

Die approbierte Originalversion dieser
Dissertation ist in der Hauptbibliothek der
Technischen Universität Wien aufgestellt und
zugänglich.

<http://www.ub.tuwien.ac.at>



The approved original version of this thesis is
available at the main library of the Vienna
University of Technology.

<http://www.ub.tuwien.ac.at/eng>



TECHNISCHE
UNIVERSITÄT
WIEN
Vienna University of Technology

DISSERTATION

Encoding and modeling techniques for center frequency agile digital RF transmitters

*ausgeführt zum Zwecke der Erlangung des akademischen Grades
eines Doktors der technischen Wissenschaften*

eingereicht an der

Fakultät für Elektrotechnik und Informationstechnik

der

Technischen Universität Wien

von

Dipl.-Ing. Henri Ruotsalainen

Matrikelnummer: 1029708

Am Kremserberg 3F

3107 St. Pölten

April 2015

Declaration of Authorship

I, Henri RUOTSALAINEN, declare that this thesis titled, 'Encoding and modeling techniques for center frequency agile digital RF transmitters' and the work presented in it are my own. I confirm that:

- This work was done wholly or mainly while in candidature for a research degree at this University.
- Where any part of this thesis has previously been submitted for a degree or any other qualification at this University or any other institution, this has been clearly stated.
- Where I have consulted the published work of others, this is always clearly attributed.
- Where I have quoted from the work of others, the source is always given. With the exception of such quotations, this thesis is entirely my own work.
- I have acknowledged all main sources of help.
- Where the thesis is based on work done by myself jointly with others, I have made clear exactly what was done by others and what I have contributed myself.

Signed:

Date:

Abstract

Current and the future radio frequency (RF) transmitters have to cope with growing data rates and support simultaneously numerous wireless standards. To this end, one of the increasingly desired features is the ability to adjust the center frequency of the transmission signal over a wide bandwidth setting. This capability leads the way to flexible RF front-ends supporting multi-mode and multi-channel operation.

Advanced, quadrature type digital transmitter concepts combine re-configurable RF signal generation with high efficiency power amplification. However, most of the state-of-the-art transmitter solutions are optimized for limited center frequency settings. Therefore, in this thesis, novel pulsed encoding and behavioral modeling techniques are presented to improve the center frequency agility.

Firstly, a novel way of digital pulse-width modulation (PWM) of quadrature sequences is given. With suitable noise shaped encoding methods, the distortion due to aliasing can be shifted away from the signal band. Thus, improved transmission signal dynamic range can be obtained for a large scale of intermediate frequency settings.

Secondly, the inherent quadrature imbalance related to the digital up-conversion technique is analyzed and suitable compensation techniques are presented. The presented quadrature noise shaped encoding algorithms enable suppression of the conjugate quantization noise and conjugate image components in the signal band of up to 50 dB. Thus, digital encoding of RF pulsed sequences with improved center frequency tuning can be enabled.

Thirdly, two complex baseband behavioral models, which capture the analog circuitry based non-linear effects of the transmitter are introduced. According to the simulation and measurement based validation results, the models are effective for a multitude of center frequency settings.

Contents

Declaration of Authorship	i
Abstract	ii
Contents	iii
List of Figures	vi
List of Tables	x
Abbreviations	xi
1 Introduction	1
1.1 Demand for center frequency agility	1
1.2 Towards digitally intensive transmitters	2
1.3 Goals and hypothesis	5
1.4 Outline	6
2 Methodology	7
2.1 Quadrature noise shaped encoding	7
2.2 Digital up-conversion technique	11
2.3 Nonlinear intersymbol interference	13
3 Digital pulse-width modulation of quadrature sequences	17
3.1 Digital pulse-width modulation	17
3.1.1 Continuous time pulse-width modulation	18
3.1.2 Discrete time Pulse-width modulation	21
3.2 Digital PWM for complex baseband signals based on quadrature noise shaped encoding	25
3.2.1 Quadrature $\Sigma\Delta$ PWM	26
3.2.2 Noise transfer function design	28
3.3 Performance evaluation of Q $\Sigma\Delta$ PWM	30
3.3.1 Signal to noise and distortion ratio	31
3.3.2 Average pulse repetition rate	36
3.3.3 Stability analysis	41

3.4	Summary	45
4	Enhanced digital up-conversion methods	47
4.1	Quadrature imbalance problem	47
4.2	Baseband modeling of digital up-conversion	49
4.3	Conjugate quantization noise compensation	53
4.3.1	Delay based compensation method	54
4.3.2	Additive compensation method	55
4.3.3	Magnitude equalization based compensation	58
4.4	Noise shaped encoders employing conjugate quantization noise compensation	59
4.4.1	Linearized models describing conjugate quantization noise folding	60
4.4.2	Noise shaped encoders with additive compensation	62
4.4.3	Noise shaped encoders with delay based compensation	65
4.4.4	Noise shaped encoders with magnitude response equalization based compensation	69
4.5	Conjugate signal compensation	71
4.6	Simulation results	72
4.6.1	Conventional digital up-conversion	72
4.6.2	Additive compensation	74
4.6.3	Delay based compensation	77
4.6.4	NTF magnitude response equalization based compensation	79
4.6.5	Conjugate signal compensation	81
4.7	Summary	83
5	Behavioral modeling of the power amplification stage	85
5.1	Equivalent complex baseband nISI model	85
5.1.1	Model derivation	86
5.1.2	Model parameter estimation	89
5.1.3	On the excitation sequence	90
5.2	Experimental time delay neural network based complex baseband model	92
5.2.1	Model description	93
5.2.2	Model parameter estimation	95
5.3	Model validation	97
5.3.1	Simulation and measurement setup	97
5.3.2	Figure of merits	99
5.3.3	Validation results based on simulations	100
5.3.4	Measurement based results	105
5.4	Summary	108
6	Conclusions	111
6.1	Future work	113

A Derivation of (4.44)	115
-------------------------------	------------

Bibliography	117
---------------------	------------

List of Figures

1.1	Block diagram of super heterodyne RF transmitter.	3
1.2	Block diagram of digital RF transmitter.	3
1.3	Quadrature type digital RF transmitter.	5
2.1	General structure of a quadrature noise shaper with a) generic quantizers and b) a linearized quantizer model.	8
2.2	Structure of the digital up-conversion block	11
2.3	Sequences involved in the digital up-conversion	12
2.4	LUT based model for nISI.	14
2.5	nISI in frequency domain.	16
3.1	PWM generation in continuous time domain.	19
3.2	Continuous TPWM in the frequency domain.	20
3.3	Continuous DPWM in frequency domain.	22
3.4	PWM generation in discrete time domain.	23
3.5	Mechanism of discrete time PWM aliasing.	24
3.6	Spectrum of discrete time PWM.	24
3.7	a) Error feedback structure of Q $\Sigma\Delta$ PWM and b) the linearized model of the former.	26
3.8	Typical spectrum of a Q $\Sigma\Delta$ PWM encoded sequence depicted over a) the entire encoded sequence bandwidth and b) near the signal band. The magnitude response of the corresponding NTF is depicted by the dashed line.	27
3.9	Magnitude responses of exemplary 2 nd order Chebyshev type NTFs. The real valued prototype NTF located at DC is depicted by the dashed line and the complex valued NTF is depicted by the bold line.	29
3.10	SNDR evaluated for various OSR settings for a) sinusoidal sequence and b) LTE sequence.	32
3.11	SNDR evaluated for various σ_x^2 settings for a) sinusoidal sequence and b) LTE sequence.	33
3.12	SNDR evaluated for various f_{IF} settings for a) sinusoidal sequence and b) LTE sequence.	33
3.13	SNDR evaluated for various f_{PWM} settings for a) sinusoidal sequence and b) LTE sequence.	34
3.14	SNDR evaluated for various $ NTF(z) _\infty$ settings for a) sinusoidal sequence and b) LTE sequence.	35

3.15	APRR evaluated for various OSR settings for a) real and b) imaginary parts of the sinusoidal sequence and c) real and d) imaginary parts of the LTE sequence.	37
3.16	APRR evaluated for various σ_x^2 settings for a) real and b) imaginary parts of the sinusoidal sequence and c) real and d) imaginary parts of the LTE sequence.	38
3.17	APRR evaluated for various $ \text{NTF}(z) _\infty$ settings for a) real and b) imaginary parts of the sinusoidal sequence and c) real and d) imaginary parts of the LTE sequence.	39
3.18	APRR evaluated for various f_{IF} settings for a) real and b) imaginary parts of the sinusoidal sequence and c) real and d) imaginary parts of the LTE sequence.	40
3.19	APRR evaluated for various f_{PWM} settings for a) real and b) imaginary parts of the sinusoidal sequence and c) real and d) imaginary parts of the LTE sequence.	41
3.20	APR evaluated for various f_{PWM} settings for a) real and b) imaginary parts of the sinusoidal sequence and c) real and d) imaginary parts of the LTE sequence.	42
3.21	Example function of $A(K)$ plotted as a function of K for a 4^{th} order NTF.	43
3.22	Estimates of K for a) sinusoidal sequence and b) LTE sequence evaluated for various σ_x^2	45
4.1	Magnitude responses of a) $H_{ma,e}(j\omega)$ and $H_{ma,e,c}(j\omega)$ over the pulsed RF sequence bandwidth b) $H_{ma,e}(j\omega)$ and $H_{ma,e,c}(j\omega)$ over the complex baseband bandwidth c) $H_{ma,o}(j\omega)$ and $H_{ma,o,c}(j\omega)$ over the pulsed RF sequence bandwidth and d) $H_{ma,o}(j\omega)$ and $H_{ma,o,c}(j\omega)$ over the complex baseband bandwidth, where $R_e = 12$ and $R_o = 13$	52
4.2	Magnitude response of $\Gamma_e(j\omega)$	56
4.3	Magnitude responses of $\Gamma_o(j\omega)$ for a) $R_o = 5$ and for b) various R_o settings.	58
4.4	Conjugate quantization noise folding compensation by additional noise shaping for a) R_e settings b) R_o settings.	59
4.5	Equivalent baseband descriptions for a combination of the linearized modulator model and the complex baseband model of the digital up-conversion in case of a) R_e and b) R_o settings.	62
4.6	Modified error feedback noise shaper structure employing additive conjugate quantization noise cancelation	63
4.7	Magnitude responses of a) complex all-pass filter $C(z)$ and corresponding equalized conjugate image transfer function and b) NTF and INTF with delay based compensation.	69
4.8	Exemplary magnitude responses of NTF and INTF with magnitude response equalization based compensation in case of a) $R_e = 8$ and b) $R_o = 7$	70
4.9	Evaluation of a) IRR and b) SNDR performance for various R_e settings.	73

4.10	Evaluation of a) IRR and b) SNDR performance for various R_o settings.	73
4.11	Evaluation of a) Maximum compensated NTF gain, b) compensated NTF average noise power, c) IRR and d) SNDR for various R_e settings.	75
4.12	Evaluation of a) Maximum compensated NTF gain, b) compensated NTF average noise power, c) IRR and d) SNDR for various R_o settings.	77
4.13	Evaluation of digital up-conversion technique with delay based compensation for a) maximum compensated NTF gain, b) compensated NTF average noise power, c) IRR and d) SNDR for various R_o settings.	78
4.14	Evaluation of digital up-conversion technique with NTF magnitude response equalization based compensation for a) maximum compensated NTF gain, b) compensated NTF average noise power, c) IRR and d) SNDR for various R_e settings.	79
4.15	Evaluation of digital up-conversion technique with NTF magnitude response equalization based compensation for a) maximum compensated NTF gain, b) compensated NTF average noise power, c) IRR and d) SNDR for various R_o settings.	81
4.16	SNDR performance without conjugate signal compensation (dashed line) and with conjugate signal compensation (thick line) for a) R_e settings and b) R_o settings.	82
5.1	Alternative complex baseband representation of the digital up-conversion.	86
5.2	Complex baseband symbols involved when nISI memory depth is equal to $R_s = 4$	88
5.3	Modeling error depicted in time domain for inadequately estimated reference nISI system.	91
5.4	Number of unique complex symbol sequences included in Q $\Sigma\Delta$ PWM encoded sequence for various M	92
5.5	Time delay neural network based complex baseband nISI model.	93
5.6	TDNN training performance for three training runs with random initial conditions.	96
5.7	Simulation and measurement based setups for model validation purposes.	98
5.8	Coefficients of the FIR filter part of the Wiener model used in the simulation setup.	99
5.9	Illustrations on the proportions of the signal spectrum that are taken into account for a) $NMSE_{pwm}$ b) $NMSE_{bb}$ and c) WESPR.	100
5.10	Simulated spectra shown a) over complete bandwidth of the encoded sequences b) near the signal band for 1) excitation 2) simulated output 3) error without modeling 4) error with equivalent nISI model 5) error with TDNN based model.	101
5.11	Simulation based modeling performance of the equivalent baseband nISI model in terms of a) $NMSE$ b) $NMSE_{bb}$ and c) $WESPR_{bb}$, where $2 \leq M \leq 3$	102

5.12	Simulation based modeling performance of the TDNN based nISI model in terms of a) NMSE b) NMSE_{bb} and c) WESPR_{bb} , where $M_i \in [2, 4, 6, 8, 10]$ and $N_i = 10$	103
5.13	Measurement based spectra shown a) over complete bandwidth of the encoded sequences b) near the signal band for 1) excitation 2) measured output 3) error without modeling 4) error with equivalent nISI model 5) error with TDNN based model.	104
5.14	Measurement based modeling performance of the equivalent base-band nISI model in terms of a) NMSE b) NMSE_{bb} and c) WESPR_{bb} , where $2 \leq M \leq 3$	106
5.15	Measurement based modeling performance of the TDNN based model in terms of a) NMSE b) NMSE_{bb} and c) WESPR_{bb} , where $M_i \in [2, 4, 6, 8, 10]$ and $N_i = 10$	109

List of Tables

3.1	Simulation parameters	31
4.1	Simulation parameters	72
5.1	Modulator parameters	97
5.2	Mean NMSE over f_{IF} and number of multiplications for equivalent baseband nISI model	107
5.3	Mean NMSE over f_{IF} and number of multiplications for TDNN based nISI model	108

Abbreviations

ADC	Analog-to-Digital Converter
ANN	Artificial Neural Network
APR	Average P ulse R ate
APRR	Average P ulse R epetition R atio
BIBO	Bounded-Input-Bounded-Output
BP$\Sigma\Delta$	Band-Pass Sigma-Delta
DAC	Digital-to-Analog Converter
DC	Direct Current
DPWM	asymmetric D ouble-edge P WM
FD	Fractional D elay
FIR	Finite I mpulse R esponse
FoM	Figure-of-Merit
FPGA	Field-Programmable-Gate-Array
INTF	Image N oise T ransfer F unction
ISTF	Image S ignal T ransfer F unction
LO	Local O scillator
LPWM	Leading edge P WM
LUT	look-up table
nISI	nonlinear I nter- S ymbol I nterference
NTF	Noise T ransfer F unction
NMSE	Normalized M ean S quare E rror
OSR	O ver- S ampling R atio
PA	Power A mplifier
PWM	P ulse- W idth M odulation

RF	R adio F requency
$\Sigma\Delta$	S igma- D elta
SMPA	S witched M ode P ower A mplifier
SNDR	S ignal-to- N oise and D istortion R atio
STF	S ignal T ransfer F unction
TDNN	T ime D elay N eural N etwork
TPWM	T railing edge P WM
WESPR	W eighted E rror S pectrum P ower R atio

Chapter 1

Introduction

1.1 Demand for center frequency agility

The evolution of wireless mobile networks and electronic wireless devices during the past 30 years has led to ubiquitous availability for e.g. telephony, internet access, and high quality sound and video. Over the past few years, the wireless connectivity has become hugely popular due to the integration of the various services into affordable, portable devices including lap-tops and smart phones. Thus the growing trend in mobile communications tends to more communication devices per person incorporating more services.

Since the radio frequency (RF) spectrum, i.e. the medium, is a limited resource and has to be shared among other terms of use, the current wireless standards need to operate on numerous frequency bands ranging from a few hundred MHz to a few GHz. From an engineering point of view, the required simultaneous support for the several standards increases the complexity of the RF transceiver. In the transmitter unit the conventional solutions incorporate a single RF transmitter chain per a single frequency band. This in the end leads on the one hand to more complex analog RF circuitry in hand-held devices and on the other hand to hardware intensive RF base-stations. A more sophisticated solution would be to enable re-use of the hardware for the different wireless standards, i.e. to enable

capability to multi-mode operation. For example in a smart-phone, a single multi-mode RF transmitter could operate on different mobile communication standards, depending on their availability. This kind of operation requires adaptation from the RF transmitter to the bandwidth and the center frequency of the transmission signal (f_c).

The emerging radio technologies call for even higher degrees of reconfigurability. One of the promising candidates to increase the spectral efficiency is a so called cognitive radio concept [1], where spectrum sensing techniques are utilized to automatically determine the available RF spectrum for communication purposes. Based on the spectrum identification results, the RF transceiver adjusts its parameters to the new transmission scenario. Hence, f_c agile RF transmitters are necessary to implement such radio concepts.

1.2 Towards digitally intensive transmitters

In Figure 1.1 the conventional RF transmitter architecture based on the super heterodyne principle is illustrated, where a band-limited baseband signal is firstly up-converted in two stages and finally the RF transmission signal is amplified by a linear RF power amplifier (PA) for transmission. Such transmitters are suitable for generation of wideband RF signals with high dynamic range. However, the concept is prone to the following undesired effects

- Nonlinear dynamic effects of the PA
- Quadrature imbalance effects
- Low PA efficiency
- Sensitivity to temperature drift and aging
- Difficult reconfiguration and integration

Despite the fact that the quadrature imbalance effects and power amplification related non-linearity can be suppressed to some extent by digital signal processing methods [2], the intensive analog component design and the limited PA efficiency makes the architecture unattractive for future wireless networks.

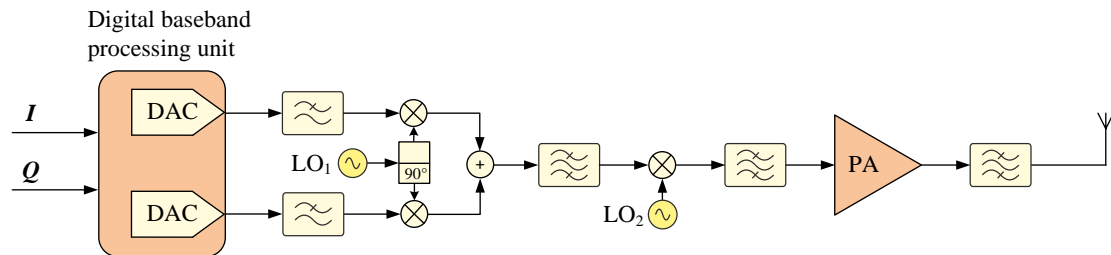


FIGURE 1.1: Block diagram of super heterodyne RF transmitter.

The advancements in silicon technology during the past decade have increased the clock rates well into the GHz range. Eventually, according to the ITRS roadmap, next to decreased power consumption the maximum available on-chip clock rate shall double between the years 2014 and 2026 [3]. Thus, replacement of the analog components of the up-conversion path with a suitable hardware performing direct digital RF signal generation constitutes a transmitter architecture with higher flexibility via programmability. This idea is strongly related to the software defined radio concept, in which the goal is to make the radio fully reconfigurable by means of digital signal processing hardware [4].

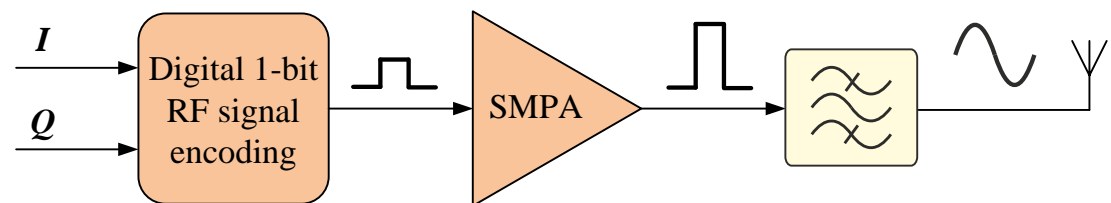


FIGURE 1.2: Block diagram of digital RF transmitter.

Figure 1.2 presents a digital RF transmitter concept, which is also called Class-S PA [5] or Delta-Sigma transmitter [6]. The RF signal generation is established with digital pulse modulation techniques, where an over-sampled digital sample sequence is encoded into a two level sequence. Hence, the resulting pulsed RF signal is suitable for the excitation of a switched-mode PA (SMPA), which enables

power amplification with high drain efficiency [7]. Due to the digital pulsed encoding, the amplified RF signal contains quantization noise and distortion products that need to be suppressed by a band-pass filter before transmission. On the one hand the advantages of the digital transmitter include

- Reconfigurable and scalable RF signal encoding
- Potentially 100% PA drain efficiency
- RF signal generation insensitive to analog component based quadrature imbalance effects, temperature drift or aging

On the other hand design issues related to the implementation of a digital transmitter comprise

- Large amount of quantization noise
- RF pulse generation and SMPA affect the RF signal encoding, which leads to increased distortion
- A band-pass reconstruction filter with steep transition bands is required to successfully suppress the out-of-band distortion products

In the literature, multiple digital RF transmitter concepts have been introduced. Some of the earliest demonstrations implement the signal encoding by band-pass sigma-delta (BP $\Sigma\Delta$) modulation [8]. Later this structurally quite simple design has been employed for Class-D RF PAs [9, 10]. Although the BP $\Sigma\Delta$ encoding enables a wide f_c tuning, the digital implementation of the encoder is required to operate at a frequency that is a multiple of f_c . Thus, implementations with state-of-the-art re-configurable hardware would allow the utilization of the transmitter up to a few hundred MHz. This drawback was alleviated by substituting the digital RF sequence encoding by a combination of complex baseband sequence encoding and a digital up-conversion technique [11]. Over the years, this approach drew more attention and various encoding methods were suggested including $\Sigma\Delta$ modulation [12–17], pulse-width modulation (PWM) [18, 19], as well as pulse position

modulation [20]. Further digital RF transmitters include digital RF-PWM based solutions [21–23] digital polar transmitters [24] and digital out-phasing transmitters [25].

1.3 Goals and hypothesis

This Thesis concentrates on the digital RF transmitter illustrated in Figure 1.3, employing PWM encoding in complex baseband. Despite the numerous efforts of the previous works, there are still important issues to be addressed in order to make the full potential of the concept available. First of all, the previously proposed encoding methods allow, in general, only for a limited adjustment of f_c . Secondly, the role of the analog circuitry based imperfections in the power amplification stage is less understood from the transmission signal linearity point of view.

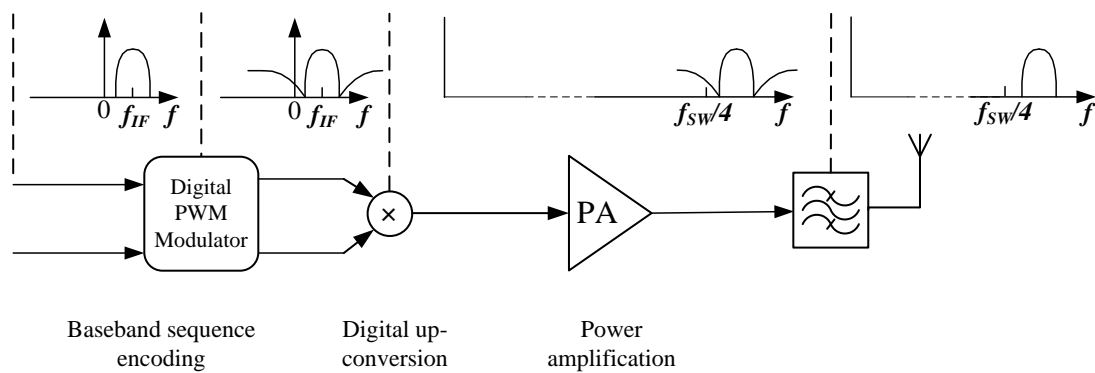


FIGURE 1.3: Quadrature type digital RF transmitter.

Based on the above given critical points, the presented work targets at two general goals:

- Enable a continuous and wide f_c adjusting.
- Identify techniques to capture the distortion of the power amplification stage.

The given goals allow for the formulation of the two main hypotheses of this Thesis:

- *Improved digital noise shaped encoding techniques shall mitigate the encoding based distortion over signal band for multiple f_c settings.*
- *Complex baseband behavioral modeling approach shall be an effective way to represent the analog circuitry related distortion*

1.4 Outline

The remainder of this Thesis is organized as follows. Chapter II gives a brief overview of the methods relevant for the digital transmitter in question. After describing the concepts of noise shaping and of digital up-conversion, which are the corner stones of the encoding part, the distortion mechanism of the power amplification stage is explained. Chapter III aims at PWM encoding of digital quadrature sequences. Motivated by harmful aliasing of the digital PWM process, a novel closed-loop modulator is given which shifts the PWM related distortion away from the signal band. The characteristics of the modulator are revealed by extensive simulations. Subsequently, novel designs of quadrature noise shapers leading to enhanced digital up-conversion techniques are given in Chapter IV. Afterwards, two new complex baseband models tailored for the complex baseband encoded sequences are demonstrated in Chapter V for behavioral modeling purposes. The performance of the models is assessed by simulation and measurement based validation setups. Finally, Chapter VI delivers next to the concluding points, also possible directions for future work.

Chapter 2

Methodology

This Chapter aims to give a compact review of the signal processing methods relevant for the quadrature type digital transmitter considered in this Thesis. At first, the single bit encoding of the complex baseband sequences will be covered. Secondly, a digital up-conversion method is explained, which is required to convert encoded baseband sequences into RF pulse sequences. Finally, the distortion mechanism related to the power amplification stage of the digital transmitter is described for the encoded pulsed RF signals.

2.1 Quadrature noise shaped encoding

Noise shaped coding or noise shaping refers to a generalized technique to manipulate quantization noise in various applications [26]. One of the most popular noise shaped encoding methods is Sigma-Delta ($\Sigma\Delta$) modulation, which has been utilized widely in digital-to-analog (DAC) and analog-to-digital (ADC) conversion in audio applications [27], in RF receivers [28, 29] as well as in digital RF transmitters [15, 30]. Figure 2.1 a) shows the generalized noise shaper structure for encoding of digital quadrature sequences $x(n)$. The type of modulation is determined by the

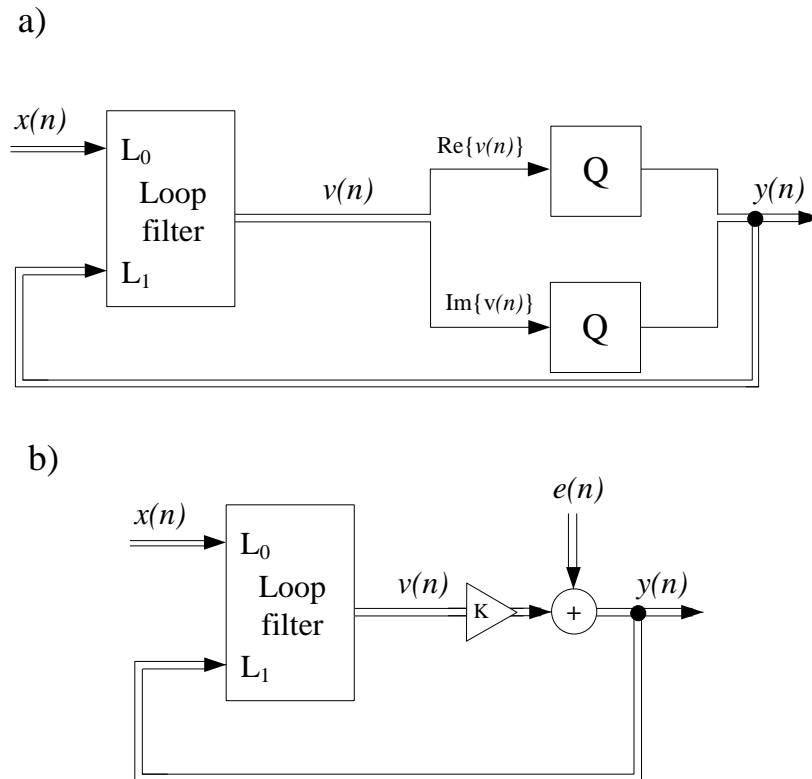


FIGURE 2.1: General structure of a quadrature noise shaper with a) generic quantizers and b) a linearized quantizer model.

choice of the quantization operations, which are here denoted by generic quantizers Q . Hence, such framework which covers multiple types of digital modulation to complex valued sequences will be referred to as *quadrature noise shaped encoding*.

The mechanism behind the shaping of the quantization noise works as follows. During a single encoder cycle the generated complex valued symbol $y(n-1)$ from the previous cycle will be fed back to the input of the modulator, where an error signal is formed. The error is fed further to loop filters $L_0(z)$ and $L_1(z)$ and finally the current complex valued bit is generated by two Q operators. Thus, $y(n)$ contains the input signal and quantization error stemming from the current cycle and a superposition of the previous quantization errors weighted by the $L_0(z)$ and $L_1(z)$. With a suitable selection of the loop filters the magnitude of the quantization noise will be weighted in the frequency domain so that the harmful distortion near the signal band is minimized. In the literature this phenomenon is commonly referred to as noise shaping.

In order to gain a better understanding on how the generic noise shaper affects the quantization noise in the frequency domain a linearized model [31] is utilized, which is originally used to analyze $\Sigma\Delta$ modulators [27]. In the linearized model shown in Figure 2.1 b) the quantizers are substituted by a combination of a gain element K and a complex valued noise source $e(n)$, which is assumed to be uncorrelated with $x(n)$. Although $e(n)$ cannot fully reproduce the nonlinear effects of the quantization, the simplification allows for calculation of the transfer function for both the signal and for the quantization noise conveniently. Given that for the generalized noise shaper topology $L_0(z) = \frac{G(z)}{H(z)}$ and $L_1(z) = \frac{H(z)-1}{H(z)}$ the output of the linearized encoder can be expressed as

$$Y(z) = \frac{1}{1 + KL_1(z)}E(z) + \frac{KL_0(z)}{1 + KL_1(z)}X(z). \quad (2.1)$$

Thus, $e(n)$ is filtered by an infinite impulse response (IIR) type filter $NTF(z) = \frac{1}{1+KL_1(z)}$, which is commonly referred to as the noise transfer function (NTF). Furthermore, the order of the nominator and the denominator of the NTF¹ determines also the order of the noise shaper (N). Since the goal of the noise shaping is to minimize the frequency content of $e(n)$ near the signal band, it is customary to define the NTF so that the stop band is centered around the center frequency of the input signal. Secondly, $x(n)$ will be modified by $STF(z) = \frac{KL_0(z)}{1+KL_1(z)}$, which in turn is called the signal transfer function (STF). Particularly in DAC applications $L_0(z)$ is often chosen so that $x(n)$ remains unchanged during encoding.

Up to this point no restrictions are put on the NTF. However, due to the fact that only the quantization errors previous to the current encoder cycle are weighted restricts the first coefficient of the numerator of the NTF(z) to be equal to one. This property is often referred in $\Sigma\Delta$ literature as the realization criterion. Hence, the NTF magnitude response $|NTF(j\omega)|^2$ exhibits in general a single or multiple stop-band regions and regions with positive gain. This reflects the fundamental principle of noise shaping: The harmful quantization noise is suppressed around the band(s) of interest and amplified in the out-of-band regions. According to the

¹Commonly equal

Gerzon-Craven theorem the optimal noise shaping performance is obtained when the NTF is of minimum phase [32]. When this condition holds, the integrals over the positive gain regions and over the stop-band regions are equal.

The most important figure of merit (FoM) for a noise shaper is the power of the remaining quantization noise in the signal band. The noise power of the linearized model can be given by

$$N_p = \frac{\sigma_e^2}{\pi} \int_{\omega_1}^{\omega_2} |NTF(e^{j\pi\omega})| d\omega, \quad (2.2)$$

where σ_e^2 denotes the variance of $e(n)$, ω_1 the beginning of the signal band and ω_2 the end of the signal band. Moreover, let $\Delta\omega = \omega_2 - \omega_1$. As it turns out, the quantity that has the most dramatic effect on N_p is a ratio called over-sampling ratio (OSR) defined as follows

$$OSR = \frac{f_{s,x}}{f_s}, \quad (2.3)$$

where $f_{s,x}$ denotes the sampling frequency of the input signal and f_s the operating frequency of the encoder, respectively. In general noise shaped encoders operate at f_s that is well beyond the Nyquist frequency of the input sequence. In order to see the significant relation between N_p and OSR it is useful to examine an exemplary 1st order NTF with $NTF(z) = 1 - z^{-1}$. For such NTF N_p can be expressed as a function of OSR as $N_p = \pi^2\sigma_e^2/3(OSR)^3$ [27]. Hence, N_p reduces exponentially as OSR increases. This characteristic is true also for other NTFs and, therefore, noise shaped encoders are also called over-sampling data converters. A further important characteristic of a modulator is the maximum noise gain defined as $|NTF(z)|_\infty$, where $|\cdot|_\infty$ denotes the Chebyshev norm. This property is commonly used in conjunction with the stability analysis of noise shaped encoders.

2.2 Digital up-conversion technique

The popular method to produce digital pulsed RF sequences [18] is shown in Figure 2.2. Given that the path between $y(n)$ and $p(n)$ can be established in the digital domain by a few logical binary operations leads to an extremely simplistic up-conversion strategy. Consequently, the computational complexity of the digital pulsed RF modulator employing digital up-conversion is largely dominated by the complex baseband encoding part. This in turn is advantageous from a fully digital transmitter design point of view, since the operating frequency of the baseband sequence encoding can be scaled suitable for reconfigurable hardware. Further, in contrast to analog quadrature mixers commonly employed in super-heterodyne and direct conversion RF transmitters, the digital up-conversion does not suffer from analog component based non-linear distortion or quadrature imbalance effects. Due to the straightforward digital implementation, the up-conversion

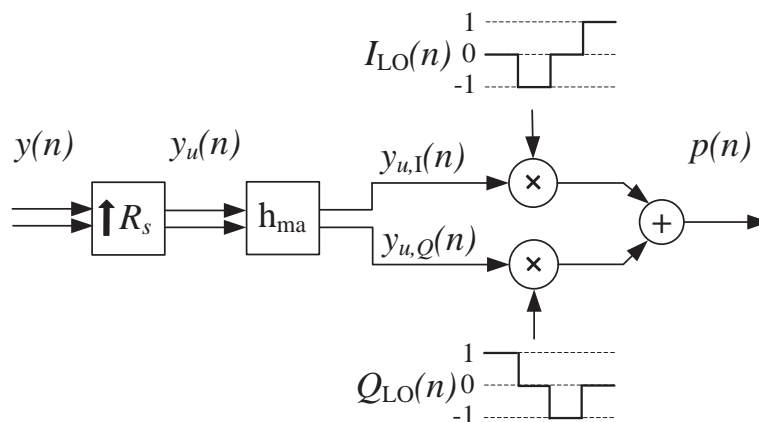


FIGURE 2.2: Structure of the digital up-conversion block

technique has been widely utilized in CMOS based digital RF signal synthesizers [13, 33–35] as well as for signal generation purposes in digital RF transmitters [12, 14, 16, 36, 37]. The practical implementations of the up-conversion technique include designs with external high-speed multiplexers [12] as well as single chip field-programmable-gate-array (FPGA) based solutions with integrated high-speed serializers [36]. From the two alternatives, the latter is more attractive for all-digital transmitters due to the scalability property of the FPGA.

The functionality of the up-conversion is as follows. At first the complex valued encoded baseband symbols $y(n)$ are up-sampled by a carrier OSR $R_s = f_{sw}/f_s$, where f_{sw} denotes the RF pulse switching rate. In order to retain the two-level sequence characteristics, the zeros contained in over-sampled symbols $y_u(n)$ are replaced by copies of $y(n)$. This operation can be represented by a convolution with a finite impulse response filter $h_{ma}(n)$ with impulse response defined as

$$h_{ma}(n) = \begin{cases} 1, & 0 \leq n \leq R_s - 1 \\ 0, & n \geq R_s. \end{cases} \quad (2.4)$$

Finally, a pulsed RF sequence $p(n)$ is generated by multiplying the real and the imaginary components of $y_u(n)$, namely $y_{u,I}(n)$ and $y_{u,Q}(n)$, by tri-state pulsed quadrature sequences $I_{LO} = [\dots, 0, -1, 0, 1, \dots]$ and $Q_{LO} = [\dots, 1, 0, -1, 0, \dots]$.

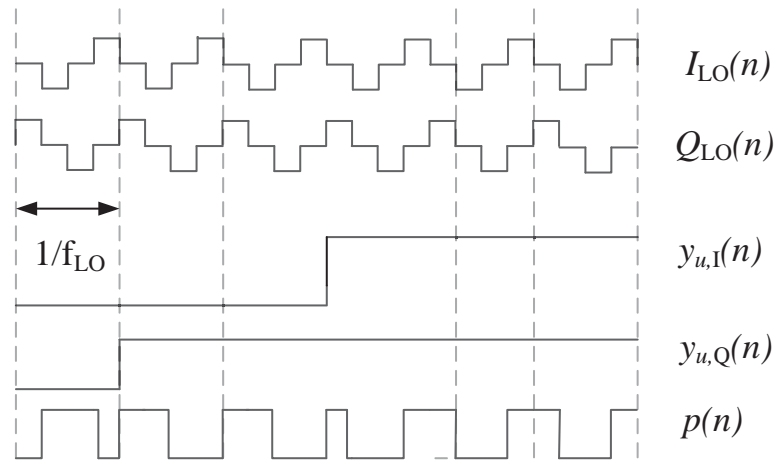


FIGURE 2.3: Sequences involved in the digital up-conversion

It can be noted that the two multiplication operations can be easily employed by discarding every second sample and by changing of the sign of every fourth sample. The detailed mathematical description of the digital up-conversion becomes

$$p(n) = [y_{u,I}(n)I_{LO}(n) + y_{u,Q}(n)Q_{LO}(n)] * h_{ma}(n), \quad (2.5)$$

where $*$ denotes the convolution operation. This mapping operation of the over-sampled and filtered complex baseband symbols is illustrated for the sake of clarity in the time domain using pulsed waveforms in Figure 2.3. On the other hand the

quadrature sequences are in fact sampled versions of the local oscillator (LO) signals, where the sampling frequency is equal to f_{sw} and the frequency of the LO signals $f_{LO} = f_{sw}/4$. This means that the DC of the $y(n)$ after up-conversion locates at $f_{sw}/4$. By observing the pulsed waveform of $p(n)$ given in Figure 2.3 it becomes clear that the phase of the $y_u(n)$ determines the phase of the RF pulse. Since in this thesis the complex baseband encoding is considered two-level, there are in total four distinct phase settings for $y_u(n)$.

2.3 Nonlinear intersymbol interference

It is commonly expected that the transmission signal dynamic range in the digital transmitter can be adjusted rather arbitrarily by selecting NTF properly. This assumption, made in the early demonstrations of digital transmitter concepts [8] as well as in the numerous follow-up works [9, 38, 39], is easy to motivate if the SMPA stage of the transmitter exhibits only memoryless non-linearity. As it is well known, such non-linearities in combination with constant envelope signals, including the two-level pulsed RF signals, cause only a DC offset to the amplified signal. However, the extensive research of microwave PAs has demonstrated that the non-linear memory effects, especially in wideband PAs cannot be neglected [40]. This suggests that for digital transmitters, where energy of the out-of-band quantization noise in comparison to the energy of the signal of interest is notable, accounting for this [behavior](#) is even more important. The effect of analog circuitry based memory on the transmission signal linearity in digital transmitters was first studied in [41]. One of the main results was that the non-linear memory implies non-linear bit-to-bit interaction for the pulsed RF signal, also referred to as non-linear inter-symbol interference (nISI). As it turns out nISI is also present at magnetic storage channels [42], high-speed audio DACs [43] as well as RF-DACs [44].

In the previous works on nISI related to digital transmitters [41, 45–47] the existence of nISI is explained by the asymmetry between the rising and the falling

edges of the RF pulse. This reasoning can be demonstrated by a relatively simple mathematical analysis in time domain. First, the continuous time pulsed signal $p_d(t)$ of the discrete time encoded pulse sequence $p(n)$ can be expressed as

$$p_d(t) = \sum_{n=-\infty}^{\infty} p(n)u(t - nT_{\text{RF}}), \quad (2.6)$$

where $u(t)$ denotes the unit pulse waveform and T_{RF} the duration of a single RF pulse. Next, let $p_b(n) = (p(n) + 1)/2$ denote binary version of $p(n)$, where -1 is mapped to 0. With these signals, the pulse asymmetry can be modeled by mapping a residual waveform $w_{\text{res}}(t)$ to a rising pulse edge as follows

$$p_{\text{isi}}(t) = p_d(t) + \sum_{n=-\infty}^{\infty} [p_b(n) - p_b(n)p_b(n-1)]w_{\text{res}}(t - nT_{\text{RF}}), \quad (2.7)$$

where $p_{\text{isi}}(t)$ denotes the distorted version of $p_b(t)$. It is immediately visible from (2.7) that the residual term is partly a non-linear function of the current and the past RF bit, which implies nISI.

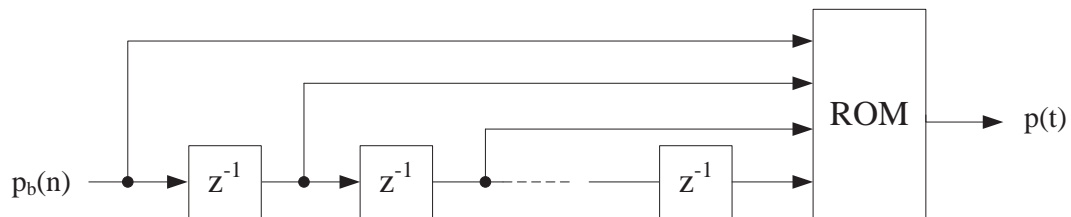


FIGURE 2.4: LUT based model for nISI.

However, at RF bit rates in the low GHz regime the nISI is more likely a function of more than two adjacent RF pulses. This hypothesis was confirmed by [44] in which the authors showed that even for pulsed signal generation alone some of the higher order nISI products are dominant in the pulsed RF signal. For these purposes the authors of [44] introduced a look-up table (LUT) based model, which is able to represent the nISI related to a time-invariant non-linear system with finite memory. As illustrated in Figure 2.4 the LUT based model includes a storage of $2^{M_{\text{RF}}} + 1$ different waveforms, which are selected dependent on the

current and the previous M_{RF} entries of $p_b(n)$. Despite the fact that the LUT based model is able to capture all possible nISI products, it does not make a distinction between the linear and the non-linear part of the non-linear system. To circumvent this problem the authors presented a Wiener type two-box model, which is under some conditions equivalent to the LUT based model. Secondly, a generalized Wiener-Hammerstein based model was given in [42], which is also able to replace the LUT based model. In the following it will be shown that the generalized Wiener-Hammerstein model can be easily derived given that the nonlinear system can be represented by a Volterra series.

Since the encoding is performed in discrete-time, it is reasonable to restrict the nISI modeling to be done in this domain as well. The discrete-time Volterra model with two-level excitation reads

$$p_{isi}(n) = h_0 + \sum_{i=1}^P V_i[p(n)], \quad (2.8)$$

where the i^{th} order Volterra kernel $V_i[p(n)]$ is given as

$$V_i[p(n)] = \sum_{m_1=0}^{M_{\text{RF}}-1} \cdots \sum_{m_n=0}^{M_{\text{RF}}-1} h_i(m_1, \dots, m_n) p(n - m_1) \cdots p(n - m_n). \quad (2.9)$$

By recognizing that $p(n - m_n)^{2k} = 1$ and that $p(n - m_n)^{(2k-1)} = p(n - m_n)$ the kernels with even and/or odd order powers reduce to the lower order kernels. What remains are the product terms involving all different combinations of time lags up to M_{RF} . This reduced model can be expressed conveniently as follows

$$p_{isi}(n) = h_0 + \sum_{i=1}^{2^{M_{\text{RF}}}} h_i \text{ISI}_i p(n), \quad (2.10)$$

in which the i^{th} nISI operator ISI_i is described as

$$\text{ISI}_i p(n) = \prod_{k \in \mathcal{K}_i} p(n - k), \quad (2.11)$$

where $\mathcal{K}_i \subseteq \mathcal{P}(S)$ denotes the i^{th} index array and $\mathcal{P}(S)$ is the power set of $S = \{1, \dots, M_{\text{RF}}\}$. As the result of each product term becomes either -1 or 1 , the model is able to represent $2^{M_{\text{RF}}}$ different output values for the memory depth of M_{RF} . Thus, (2.10) is a discrete time equivalent to the generalized continuous time nISI model presented in [42]. In contrast to the LUT based model, (2.10) is a decomposition of a DC part, a linear impulse response as well as a non-linear impulse response for the nISI terms.

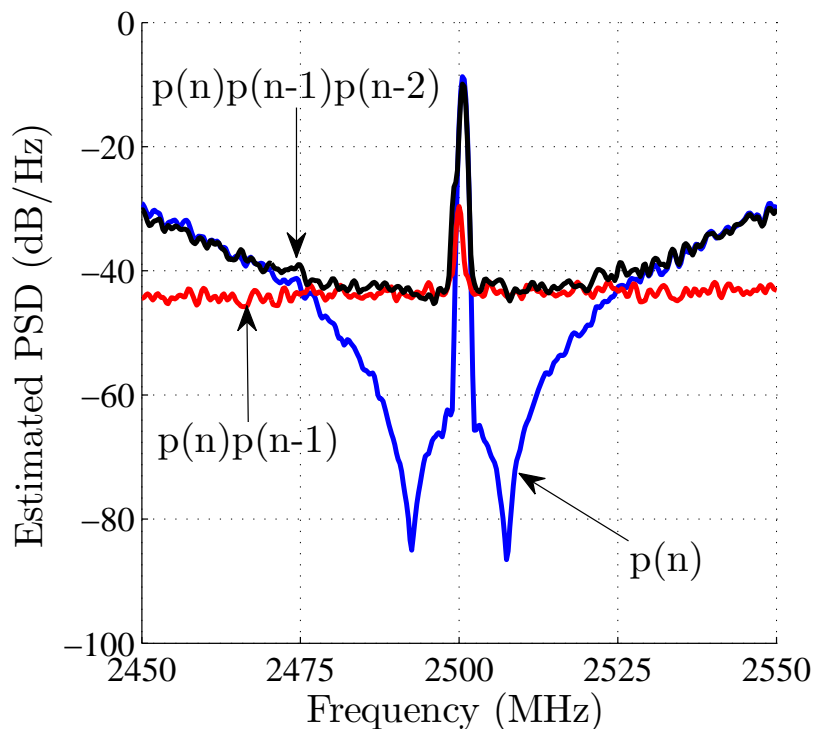


FIGURE 2.5: nISI in frequency domain.

In Figure 2.5 the spectra of $p(n)$ as well as two exemplary nISI sequences $p(n)p(n-1)$ and $p(n)p(n-1)p(n-2)$ are illustrated near the signal band. As it is clearly visible, the power of both nISI sequences is significantly higher in comparison to the power of the residual quantization noise around the signal band. Evidently, the source of the residual nISI based distortion is the high amount of noise shaped out-of-band quantization noise which due to the multiplication between the RF pulse sequence entries modulates back to the signal band.

Chapter 3

Digital pulse-width modulation of quadrature sequences

Pulsed encoding of the quadrature sequences in digital domain constitutes the first part of the digital transmitter. In this Chapter the digital pulse-width modulation (PWM) as a potential type of encoding is studied. After a brief introduction, the distortion mechanism of the discrete time PWM is explained. Motivated by the descriptions of the conventional digital PWM processes and their distortion behavior, a novel closed-loop PWM modulator for complex baseband signals is given. The modulator utilizes noise shaping to push the harmful distortion products away from the signal band. The advantage over prior quadrature type encoders is that the input signal can be located on an arbitrary intermediate frequency. Finally, the characteristics of the modulator are analyzed in detail by simulations.

3.1 Digital pulse-width modulation

The evolution of the computational resources has inspired implementations of PWM in the digital domain. The early applications concentrating on low-frequency signal modulation included e.g. highly efficient power converters and audio amplifiers [48–50]. As the clock rates of the digital signal processing hardware advanced

into the high MHz and low GHz regime, a broader range of applications was enabled including RF transmitters [8]. The digital PWM enjoys the same preferred qualities as other linear and nonlinear digital signal processing methods. The modulation in the digital domain is exactly defined and not affected by analog component imperfections. In addition, the simplest variants of the digital PWM can be implemented with very low computational complexity. However, the digital PWM as well as the analog domain PWM implement nonlinear modulation, which results in distortion products in the vicinity of the signal band. The digital implementation of the PWM means that the generated PWM signal has limited time resolution. This limitation, as explained more detailed below, leads to distortion levels much higher than would be expected from a continuous time PWM.

3.1.1 Continuous time pulse-width modulation

The fundamental principle of the PWM is to convert a band-limited signal into a stream of variable length pulses with a fixed pulse repetition rate. A multitude of techniques to perform the determination of the pulse lengths has been proposed [51]. In this thesis, a method called natural sampling PWM is considered due to its superior distortion performance in the baseband [52].

Figure 3.1. presents the basic mechanism of the natural sampling PWM for continuous time excitation. The pulsed output signal is obtained by a comparison of the excitation $x(t)$ and a repetitious carrier signal. Both signals are restricted between $[-1, 1]$. The choice of a sawtooth waveform as the carrier, as shown in Figure 3.1, results in a single transition per PWM pulse. Hence, this type of modulation is called single edge PWM. Further, if the sawtooth carrier slope is chosen increasing or decreasing the resulting modulation is called trailing edge PWM (TPWM) or leading edge PWM (LPWM), respectively. Since these two types of modulation differ only by a change of sign, only TPWM will be analyzed in the following. The pulsed TPWM signal can be expressed in the time domain as a function of the excitation as follows [52]

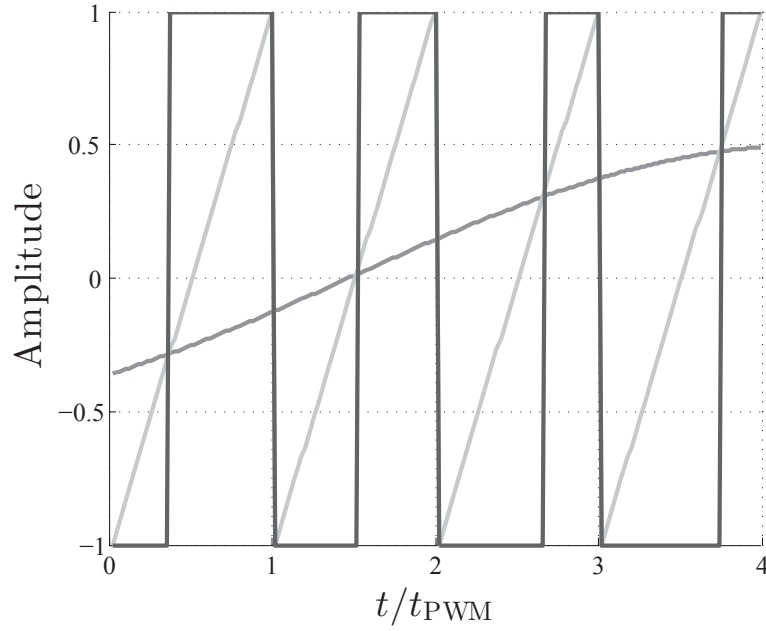


FIGURE 3.1: PWM generation in continuous time domain.

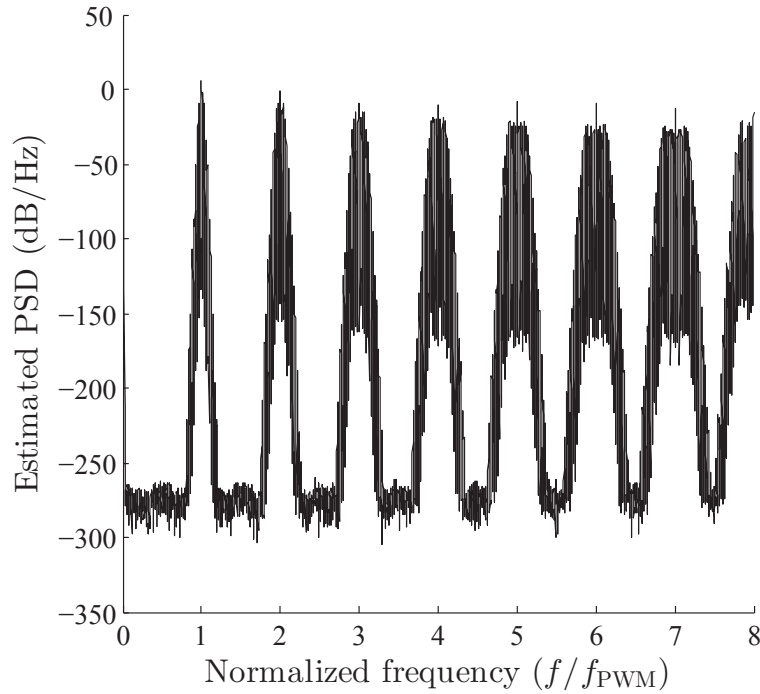
$$\text{pwm}_{\text{TE}}(t) = x(t) + \sum_{k=1}^{\infty} \frac{2}{k\pi} [\sin(2\pi k f_{\text{PWM}} t) - (-1)^k \sin(2\pi k f_{\text{PWM}} t - k\pi x(t))], \quad (3.1)$$

where f_{PWM} denotes the PWM carrier frequency. From (3.1) it can be identified that the TPWM consists of the excitation, of sinusoidal components located at multiples of f_{PWM} and copies of phase modulated excitation located at multiples of f_{PWM} . In the literature the sinusoidal components are commonly referred to as carrier harmonics.

The most interesting and important attribute of the natural sampling PWM is that when f_{PWM} is chosen appropriately, the distortion due to the phase modulation can be made negligibly small. The frequency domain equivalent to (3.1) is

$$\begin{aligned} \text{PWM}_{\text{TE}}(f) &= X(f) \\ &+ \sum_{k=1}^{\infty} (-1)^k \sum_{n=1}^{\infty} \frac{(jk\pi)^{(n-1)}}{n!} [S_n(f + kf_{\text{PWM}}) + (-1)^{(n-1)} S_n(f - kf_{\text{PWM}})], \quad (3.2) \end{aligned}$$

where $S_n(f)$ denotes the Fourier transform of $x(t)^n$. Figure 3.2. shows an exemplary case of $|\text{PWM}_{\text{TE}}(f)|^2$ for a sinusoidal excitation. Next to the first eight

FIGURE 3.2: Continuous TPWM in the frequency domain.

carrier harmonics and phase modulation products, it is visible that the frequency band near the signal is nearly distortion free as stated above.

Alternatively, a periodical triangular signal can be utilized for the carrier signal. Since the triangular waveform can be represented as a combination of subsequent sawtooth waveforms with increasing and decreasing slope, a single PWM cycle obtained by a comparison with the triangular waveform is in fact a combination of TPWM and LPWM. This results in two pulse transitions per one triangular signal period. Hence the type of the modulation is called asymmetric double-edge PWM (DPWM). Similar to TPWM, a time domain expression as a function of the excitation for the DPWM exists as well [52] and it becomes

$$\text{pwm}_D(t) = x(t) + \sum_{k=1}^{\infty} \frac{2(-1)^k}{k\pi} \left[\sin\left(2\pi k f_{\text{PWM}} t + k\pi \frac{x(t)+1}{2}\right) - \sin\left(2\pi k f_{\text{PWM}} t - k\pi \frac{x(t)+1}{2}\right) \right]. \quad (3.3)$$

In contrast to TPWM, as visible from (3.3) DPWM does not contain separate sinusoidal components. This means that in principle DPWM is free from the

carrier harmonics. However, each of the two phase modulation products contains a sinusoidal component. On the one hand for the phase modulation products mapped onto the even multiples of f_{PWM} , the sinusoidal components cancel due to a phase difference of π . On the other hand, for the phase modulation products on odd multiples of f_{PWM} , the phase difference between the products is zero and thus for DPWM there are harmonic products only at odd multiples of f_{PWM} . The frequency domain representation of (3.3) becomes

$$\begin{aligned} \text{PWM}_D(f) = X(f) &+ \sum_{k=1}^{\infty} (-1)^k \sum_{n=1}^{\infty} \left[\frac{(j2k\pi)^{(2n-2)}}{2^{(2n-2)}(2n-1)!} (S_{2n-1}(f + 2kf_{\text{PWM}}) + S_{2n-1}(f - 2kf_{\text{PWM}})) \right. \\ &\left. - \frac{(j(2k-1)\pi)^{2n-1}}{j2^{2n-1}(2n)!} (S_{2n}(f + (2k-1)f_{\text{PWM}}) + S_{2n}(f - (2k-1)f_{\text{PWM}})) \right]. \quad (3.4) \end{aligned}$$

Figure 3.3. shows an exemplary case of $|\text{PWM}_D(f)|^2$ for a sinusoidal excitation. As explained above, no peaks in spectral power are visible at even multiples of f_{PWM} . Furthermore, similar to TPWM the DPWM exhibits very small levels of distortion near the signal band.

3.1.2 Discrete time Pulse-width modulation

The results regarding time and frequency domain presentations of the previous sub-section for the continuous time PWM are well studied and known practically since the first frequency domain analysis [51]. In contrast, the distortion of the digital PWM due to the limited time resolution is much less investigated. The work presented in [53–55] gives the first insights into how the quantization of the PWM pulse edges affects the spectrum of the digital PWM sequence. The brief analysis given here is based on the work of [54].

As depicted in Figure 3.4, the discretized version of natural sampling PWM is equal to the continuous time natural sampling PWM sampled by a sampling rate f_s . On the other hand, the sampling process can be applied separately to the input

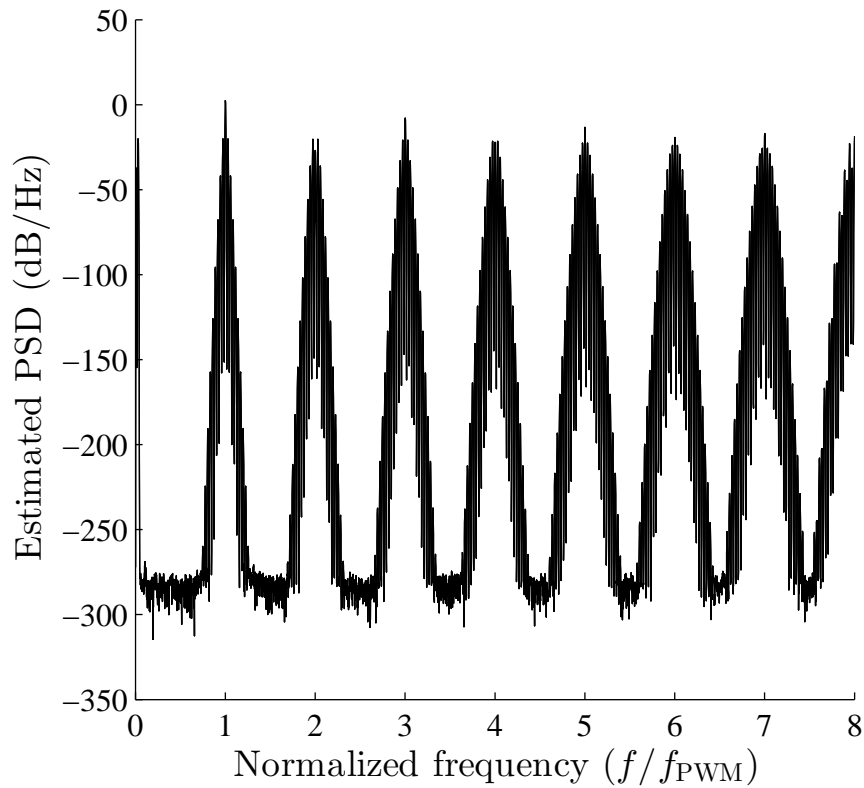


FIGURE 3.3: Continuous DPWM in frequency domain.

signal and to the carrier signal. Thus, as illustrated in Figure 3.4, the modulation by the sampled signals yields the sampled continuous natural sampling PWM. Therefore, the time domain representations of the digital TPWM and the DPWM as a function of the excitation can be obtained by evaluating (3.1) and (3.3) at the sampling instants. The evaluations lead to the following formulation for TPWM

$$\text{pwm}_{\text{TE}}(n) = x(n) + \sum_{k=1}^{\infty} \frac{2}{k\pi} [\sin(2\pi k f_{\text{PWM}} t) - (-1)^k \sin(2\pi k f_{\text{PWM}} t - k\pi x(n))], \quad (3.5)$$

and for DPWM

$$\text{pwm}_{\text{D}}(n) = x(n) + \sum_{k=1}^{\infty} \frac{2(-1)^k}{k\pi} [\sin(2\pi k f_{\text{PWM}} t + k\pi \frac{x(n) + 1}{2}) - \sin(2\pi k f_{\text{PWM}} t - k\pi \frac{x(n) + 1}{2})]. \quad (3.6)$$

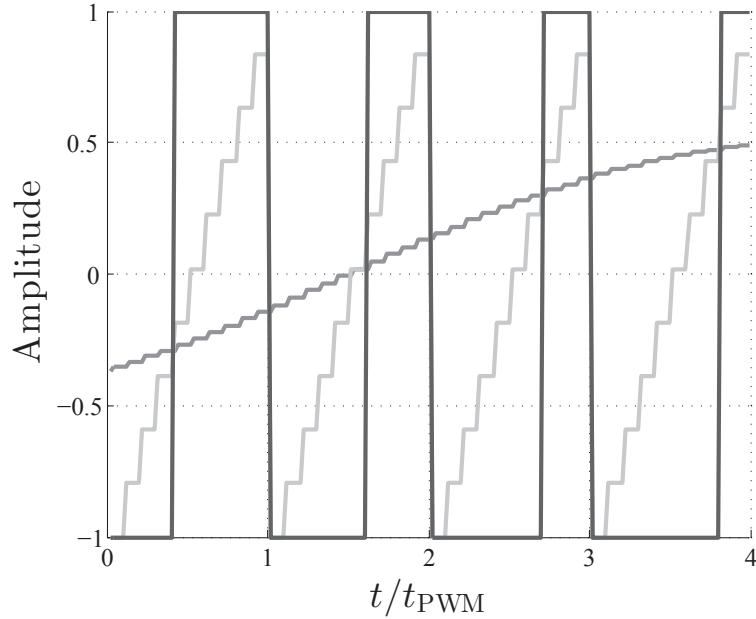


FIGURE 3.4: PWM generation in discrete time domain.

From the above expressions it is already clear that for the sampled PWM sequences the Nyquist criterion for band-limited signals is violated. This result is not surprising since the continuous time PWM signals have effectively infinite spectral spread. As a result of sampling the frequency domain versions of (3.5) and (3.6) become

$$\text{PWM}_{\text{TE},s}(f) = \frac{1}{t_s} \sum_{l=-\infty}^{\infty} \text{PWM}_{\text{TE}}\left(\frac{f}{t_s} - \frac{2\pi l}{t_s}\right), \quad (3.7)$$

and

$$\text{PWM}_{\text{D},s}(f) = \frac{1}{t_s} \sum_{l=-\infty}^{\infty} \text{PWM}_{\text{D}}\left(\frac{f}{t_s} - \frac{2\pi l}{t_s}\right), \quad (3.8)$$

respectively, where t_s denotes the sampling interval. Hence the entire spectral content of the continuous time PWM is mapped onto multiples of the sampling frequency f_s , which in the end yields a repetitious spectrum for the digital PWM. Thus, the frequency content related to the carrier harmonics and to the phase modulated products crossing $0.5f_s$ fold back to the baseband.

This phenomenon, regularly referred to as aliasing, is illustrated in Figure 3.5 for a sampled TPWM with sinusoidal excitation, where $f_s = 8f_{\text{PWM}}$. It is clearly visible that the baseband signal content is no more distortion free. In the exemplary case the first PWM harmonic coinciding with the signal band is the 8th harmonic.

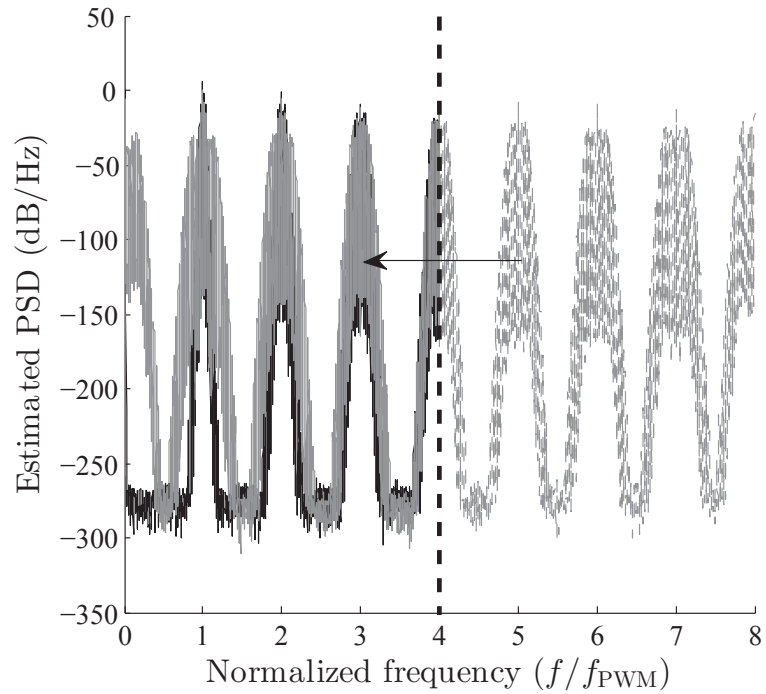


FIGURE 3.5: Mechanism of discrete time PWM aliasing.

The further phase modulated harmonic products occupy increasing ever wider bandwidths, which leads to further aliasing. Thus, the digital PWM suffers from severe destructive distortion, which is illustrated in Figure 3.6. Obviously, aliasing

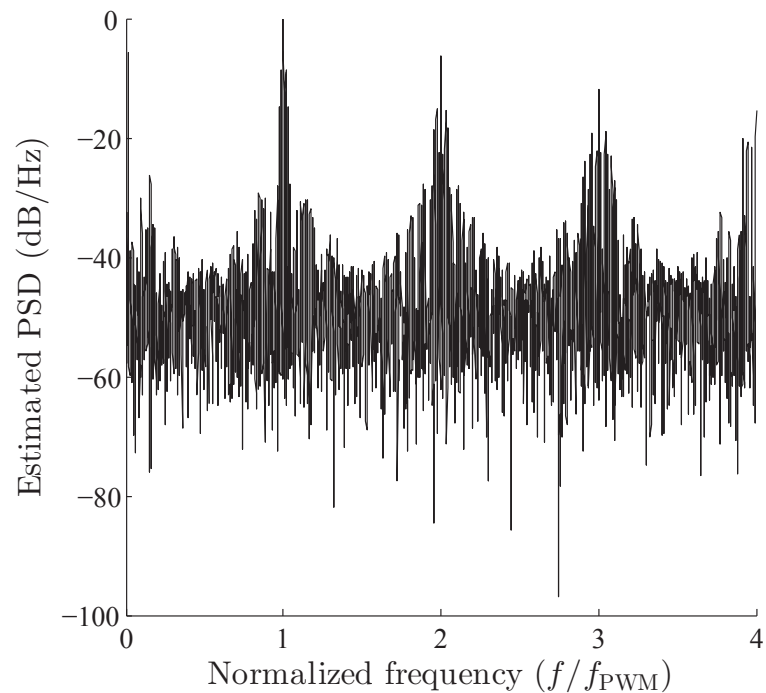


FIGURE 3.6: Spectrum of discrete time PWM.

can be reduced in the conventional implementations of digital PWM by selecting f_{PWM} high enough. However, the finite time resolution supported by the current reconfigurable hardware limits the achievable transmission signal dynamic ranges. In fact, the distortion levels may not be sufficiently small to support requirements for modern wireless standards [19]. Therefore, alternative methods to suppress the aliasing effects have to be considered.

3.2 Digital PWM for complex baseband signals based on quadrature noise shaped encoding

As presented in the previous Section the sampled PWM processes suffer from aliasing, which leads to a poor dynamic range especially when the f_{PWM} is close to f_s . This property is unacceptable for modern transmission signals with stringent linearity requirements [56]. Therefore, it is of interest to search suitable techniques, which allow for optimization of the magnitude of the aliasing components and, thus, improvement of the signal quality. The previously given methods with this goal include e.g. multi-level PWM concepts, which effectively cancel the aliasing products [57]. Furthermore, band-limited PWM technique was given in [54], where the digital PWM sequences are analytically composed so that only the harmonics, which do not contribute to aliasing, are included in the modulation. These techniques, however, require either multi-stage PA or additional DACs, which complicate the design of the digital transmitter. Hence, this sections aims to provide solution to the single bit PWM encoding of the quadrature baseband sequences. Moreover, in order for the digital transmitter system to support multi-channel operation sufficient signal quality shall be guaranteed for the encoded RF signal at various f_c settings.

3.2.1 Quadrature $\Sigma\Delta$ PWM

The common problem for most of the PWM based noise shaped encoders is that the aliasing process needs to be addressed for a satisfactory encoding performance in terms of attainable dynamic range. For this reason a multitude of so called open-loop encoder topologies have been given that perform the digital PWM and the aliasing mitigation by a noise shaped encoding, separately [58–60]. When such encoders are applied for oversampled and band-limited sequences located at f_θ in complex baseband, the optimal encoding performance is obtained for a single intermediate frequency setting, namely when $f_{IF} = 0$ and $f_\theta \approx 0$. Clearly, such limitation restricts the multi-channel operation of the digital transmitter.

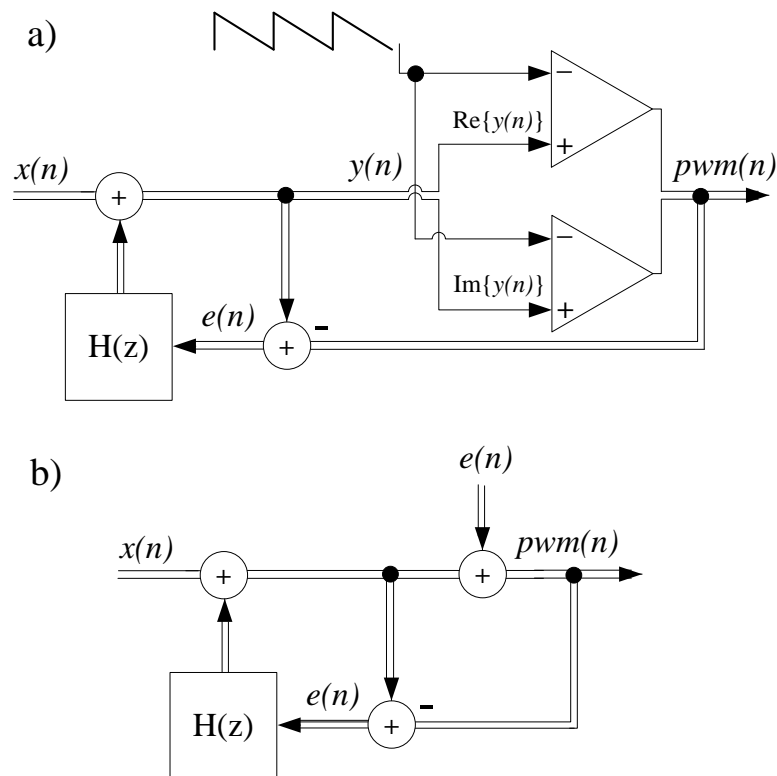


FIGURE 3.7: a) Error feedback structure of Q $\Sigma\Delta$ PWM and b) the linearized model of the former.

In Figure 3.7 a) a novel quadrature type digital PWM modulator for complex baseband signals is given. The modulator is based on a discrete time version of closed-loop PWM [61], where the digital PWM operator is included inside a noise shaper loop. Since the modulator topology is closely related to a quadrature $\Sigma\Delta$

modulator [28, 62], the modulator will be referred to as Q $\Sigma\Delta$ PWM. The closed-loop topology of the Q $\Sigma\Delta$ PWM enables modifications not only to the harmful aliasing products, but also to the non-aliased products in a relatively simple manner. Furthermore, with separated noise shaping part and PWM generation part, the novel structure can be utilized easily for many kinds of PWM.

For a practical realization of the Q $\Sigma\Delta$ PWM an error feedback noise shaper topology is chosen due to the possibility to implement the weighting of the quantization noise rather arbitrarily. The linearized model of the Q $\Sigma\Delta$ PWM with error feed-

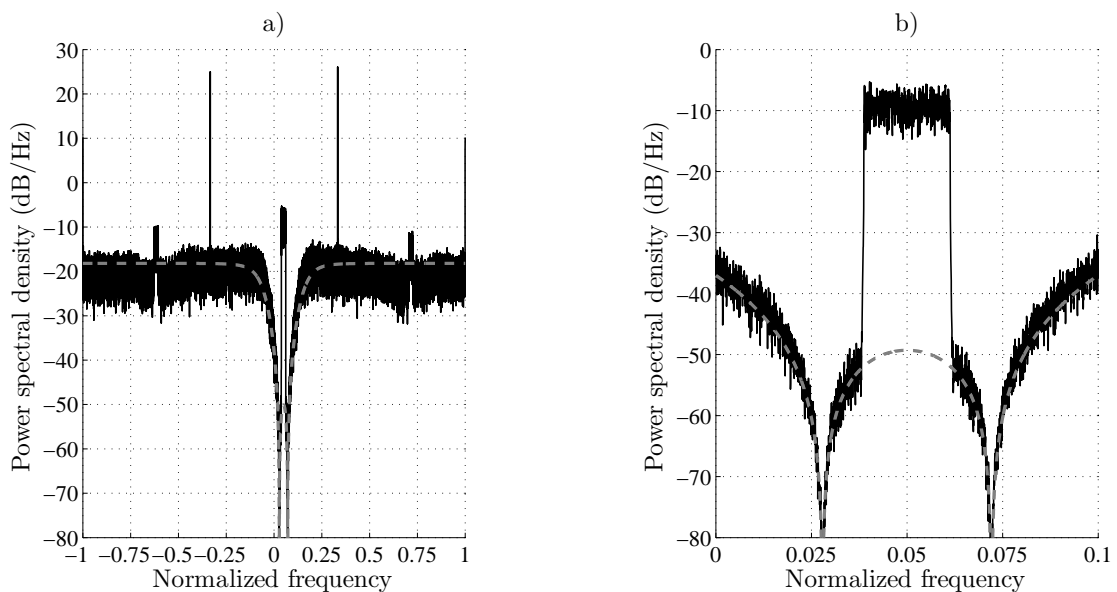


FIGURE 3.8: Typical spectrum of a Q $\Sigma\Delta$ PWM encoded sequence depicted over a) the entire encoded sequence bandwidth and b) near the signal band. The magnitude response of the corresponding NTF is depicted by the dashed line.

back is shown in Figure 3.7 b). For such loop topology $\text{NTF}(z) = 1 - H(z)$ and $\text{STF}(z) = 1$, where $H(z)$ denotes the loop filter. Hence, the input-output relation for the linearized model can be written as

$$\text{PWM}(z) = \text{NTF}(z)E(z) + X(z). \quad (3.9)$$

This means that the distortion products will be weighted by NTF and $x(n)$ remains unchanged, as desired. Figure 3.8 depicts an exemplary power spectral density estimates of $pwm(n)$. As clearly visible from Figure 3.8 a) the noise shaping loop implements an NTF (dashed line), which in turn modifies the aliased PWM

harmonics. Hence, as seen in Figure 3.8 b) the signal band dynamic range is notably improved.

3.2.2 Noise transfer function design

In general, digital RF signal encoders based on noise shaped encoding employ NTFs that are of either low-pass type [12], band-pass type [8] or high-pass type [63]. Popular choices for the NTFs in various RF signal encoders include IIR filters of typically Butterworth, Chebyshev or maximally flat all-pole designs [64]. The historical background of these filters is that they are well suited for the noise shaper topologies used in the $\Sigma\Delta$ ADC converters. However, as explained in section 2.1 the noise shaped encoders operating in the digital domain are in general not restricted to implement an NTF of a specific type. Therefore, alternative NTF designs have been developed, which are optimal in terms of e.g. N_p or other application related design metric [65–67]. Nevertheless, the utilization of the $\Sigma\Delta$ modulator based NTFs in Q $\Sigma\Delta$ PWM as well as other RF signal encoders is justified for the following reasons

- They fulfill the Gerzon-Craven theorem for optimal noise shaping.
- The respective loop filter realizations require fewer computational operations, thus leading to a lower computational complexity.
- The properties of the $\Sigma\Delta$ modulators implementing those NTFs are well studied.
- The existence of a well documented, widely popular $\Sigma\Delta$ toolbox [68].

One of the fundamental advantages of the Q $\Sigma\Delta$ PWM is the possibility to utilize a complex valued NTF. This yields two important properties. Firstly, the noise notches can be arbitrarily shifted in the over-sampled complex baseband to a desired f_{IF} . Secondly, the $|NTF(j\omega)|^2$ can be defined to be asymmetric with respect to DC. The first property enables the f_c tuning since, as presented earlier

in Chapter 2.2, the frequency content of the encoded complex baseband sequence will be mapped around a fixed carrier frequency. The second property is useful in a situation where multiple signals are to be encoded simultaneously that have distinct N_p requirements. Furthermore as shown in [69], the second property enables also a more advanced NTF design for RF signal encoding that fulfills the requirements set for spurious emissions and spectral mask.

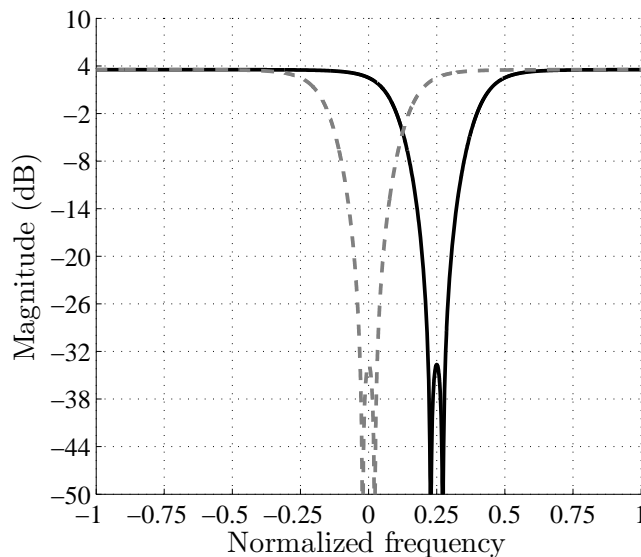


FIGURE 3.9: Magnitude responses of exemplary 2nd order Chebyshev type NTFs. The real valued prototype NTF located at DC is depicted by the dashed line and the complex valued NTF is depicted by the bold line.

The design of the complex valued NTFs can be established by a technique called frequency translation method [70]. At first a prototype lowpass type NTF is designed. Such a 2nd order low-pass type NTF based on Chebyshev IIR filter designed with the $\Delta\Sigma$ toolbox [68] is illustrated in figure 3.9 by the dashed line. In the z-domain the transfer function of the NTF is as follows

$$\text{NTF}(z) = \frac{1 - 1.995z^{-1} + z^{-2}}{1 - 1.1216z^{-1} + 0.4478z^{-2}}. \quad (3.10)$$

Here $OSR = 32$ and $|\text{NTF}(z)|_{\infty} = 1.5$. The Chebyshev type filters are beneficial for RF encoders, since they enable flat signal band noise power also for lower OSRs. Given that the coefficients of the numerator and the denominator of the prototype NTF are given in vectors $\mathbf{NTF}_{\mathbf{n}} = [1 \ b_1 \ \cdots \ b_N]$ and $\mathbf{NTF}_{\mathbf{d}} = [1 \ a_1 \ \cdots \ a_N]$,

respectively, the complex valued NTF can be obtained as follows

$$\text{NTF}(z) = \frac{\text{NTF}_{\mathbf{n}} \mathbf{z} \Psi}{\text{NTF}_{\mathbf{d}} \mathbf{z} \Psi}, \quad (3.11)$$

where

$$\Psi = \begin{bmatrix} 1 & 0 & \dots & 0 \\ 0 & e^{(j\pi f_s/f_{\text{IF}})} & \dots & 0 \\ \vdots & \dots & \ddots & 0 \\ 0 & 0 & 0 & e^{(Nj\pi f_s/f_{\text{IF}})} \end{bmatrix} \quad (3.12)$$

and $\mathbf{z} = [1 \ z^{-1} \ \dots \ z^{-N}]$. An example for the magnitude response of a translated NTF is illustrated in Figure 3.9 by the bold line. Finally, the coefficients of $H(z)$ are obtained by evaluating $H(z) = \frac{1}{1 - \text{NTF}(z)}$.

3.3 Performance evaluation of QΣΔPWM

As explained before, the QΣΔPWM incorporates digital PWM operators in a feedback loop. In contrast to purely linear systems for which exact time and frequency domain input-output relations can be obtained, such analysis turns out to be exhaustively difficult for closed loop PWM systems. In fact, apart from analysis presented for some limited ΣΔ loop topologies [71], a generalized technique that explains exactly the functionality of an arbitrary noise shaped encoder, up to the author's best knowledge, does not exist. For these reasons, the most commonly utilized methods to characterize noise shaping structures include linearized models and computer simulations [27]. Thus, in this thesis the same methodologies will be used to analyze the performance of the QΣΔPWM.

The main purpose of the analysis is to deliver the answers to the following questions relevant for digital RF transmitter design purposes.

- What is the expectable level of distortion for a reconstructed transmission signal?

- Are there modulator settings that yield inherently superior noise shaping performance?
- Are there modulator settings that lead to unreliable performance?

TABLE 3.1: Simulation parameters

f_s	$\Delta\omega$	f_{IF}	f_{PWM}	$ NTF(z) _\infty$	N	σ_x^2
800 MHz	25 MHz	0	$f_s/6$	1.5	2	0.1

Unless noted otherwise, the modulator settings given in Table 3.1 are utilized throughout the performance study. The simulations are performed for two different input sequences. The first one is a sinusoid with frequency equal to 400 kHz and the second one is a 20 MHz LTE signal with peak-to-average-power-ratio equal to 10 dB. The chosen f_s settings and input sequences represent the present day scenario, where a state-of-the-art reconfigurable hardware is utilized to implement a modulator that encodes modern broadband transmission sequences. A single data point is obtained as an average of 20 distinct modulator runs.

3.3.1 Signal to noise and distortion ratio

A metric that is frequently utilized to describe the distortion performance of a noise shaped encoder is signal-to-noise and distortion ratio (SNDR) defined as

$$\text{SNDR} = \frac{\int_{\omega_{s,1}}^{\omega_{s,2}} |S(e^{j\pi\omega})|^2 d\omega}{\int_{\omega_1}^{\omega_2} |S(e^{j\pi\omega}) - S_r(e^{j\pi\omega})|^2 d\omega}, \quad (3.13)$$

where $\omega_{s,1}$ and $\omega_{s,2}$ denote the band edges of the input signal, $S(e^{j\pi\omega})$ the spectrum of the input signal and $S_r(e^{j\pi\omega})$ the spectrum of the reconstructed signal. Hence, in the case of Q Σ Δ PWM SNDR relates the input sequence power to the distortion products falling into the reconstruction bandwidth stemming from the digital PWM. In digital domain SNDR can be conveniently evaluated using a single power spectral density estimate of the encoded sequence. The procedure used here for an accurate estimation is the one given in [64] (pp. 365-388).

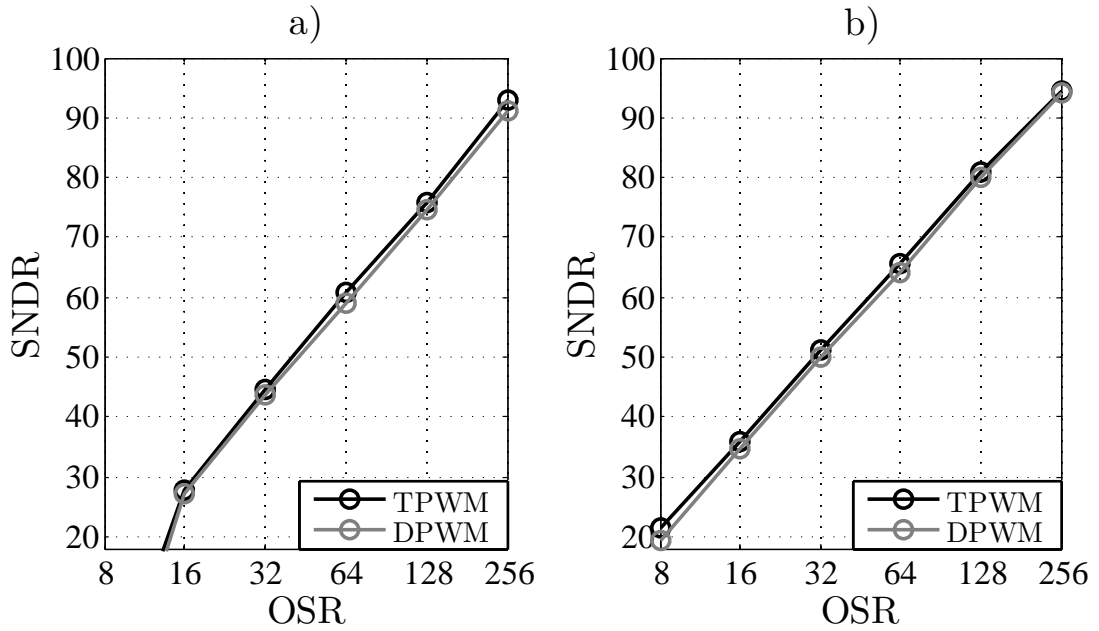


FIGURE 3.10: SNDR evaluated for various OSR settings for a) sinusoidal sequence and b) LTE sequence.

At first the SNDR as a function of OSR was evaluated and the results are shown in Figure 3.10. As predicted by the linearized model for the corresponding 2^{nd} order NTF, doubling the OSR increases the SNDR by 16 dB. The given prediction is valid for both PWM types and excitation sequences. It is also visible that the choice of TPWM yields a slight increase in SNDR. In the implementation point of view, the lowest possible OSR is desirable due to lowered clock rates and thus, reduced hardware power dissipation. However, for the considered setup, the OSRs between 8-16 result in SNDRs that are most likely unsuitable for modern RF transmission usage. On the other hand, the OSRs between 64-256 correspond to f_s settings between 1.6-6.4 GHz for which presently no reconfigurable hardware is available. Therefore, the OSRs ranging from 20 to 40 represent the realistic settings for which tolerable distortion levels are available.

The dependency between SNDR and σ_x^2 is illustrated in Figure 3.11. For a sinusoidal excitation, the SNDR shown in Figure 3.11 a) grows monotonously for both modulation schemes up to $\sigma_x^2 = -4$ dB, after which due to over modulation the harmonic distortion inside the reconstruction band is increased. The SNDR obtained for the LTE excitation shown in Figure 3.11 b) shows no compression

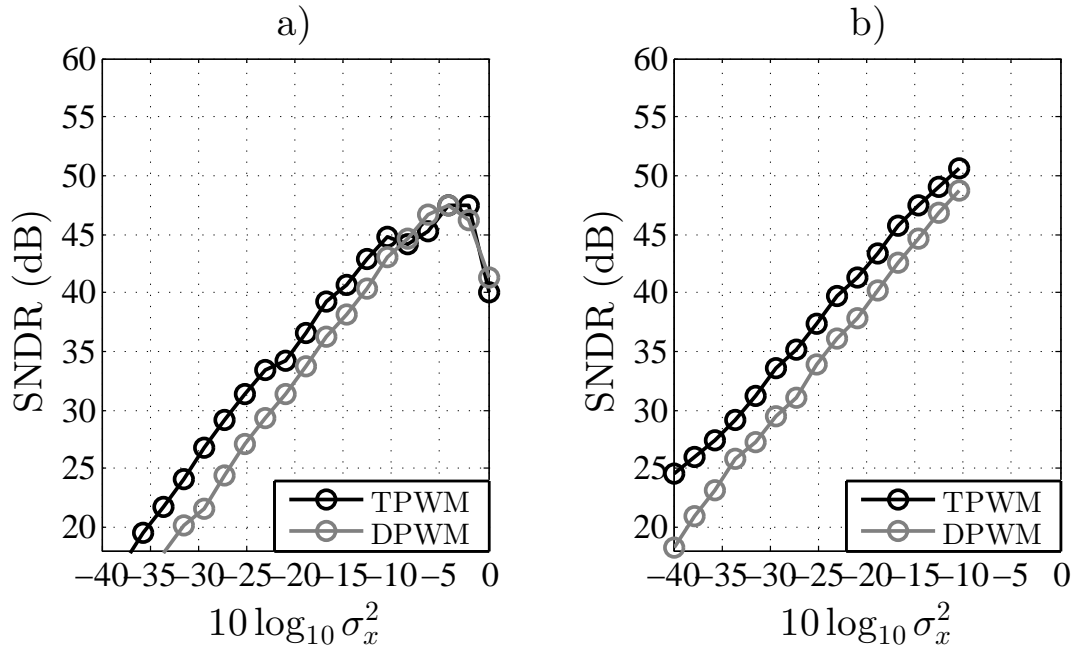


FIGURE 3.11: SNDR evaluated for various σ_x^2 settings for a) sinusoidal sequence and b) LTE sequence.

despite the full scale magnitude setting for $\sigma_x^2 = -10$ dB. This can be explained by the Gaussian amplitude distributions of the real and the imaginary parts of the excitation, resulting from the orthogonal frequency multiplexing modulation used in LTE. Therefore, the digital PWM operators are driven into over-modulation less frequently, which leads to less harmonic distortion.

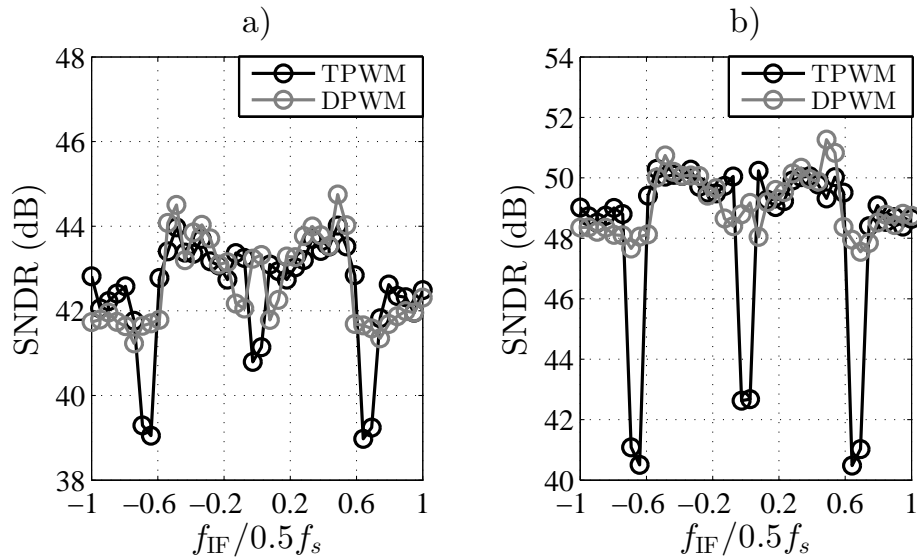


FIGURE 3.12: SNDR evaluated for various f_{IF} settings for a) sinusoidal sequence and b) LTE sequence.

At next, the SNDR as function of f_{IF} was investigated for the tuning range between $-0.5f_s \leq f_{\text{IF}} \leq 0.5f_s$. According to the linearized model, the frequency shifting operation applied on the prototype NTF shall not affect the magnitude response of the distortion products. This property is visible in the simulated results given in Figure 3.12. The SNDR for both excitations over the complete Nyquist range is nearly constant apart from a few f_{IF} settings for TPWM, where the PWM carrier harmonics are located in the signal band. The wide f_{IF} tuning beyond f_{PWM} is possible for digital closed loop PWM modulators since the noise shaper and the digital PWM operators are performing independently. This is a clear advantage over digital open-loop PWM modulators, which in general require the highest frequency component of the excitation to be located well below f_{PWM} for the correct determination of the PWM duty cycles. Thus, for the considered simulation settings a total f_{IF} tuning range of 800 MHz can be obtained, which potentially enables a very flexible multi-channel and multi-mode operation for a fully digital transmitter.

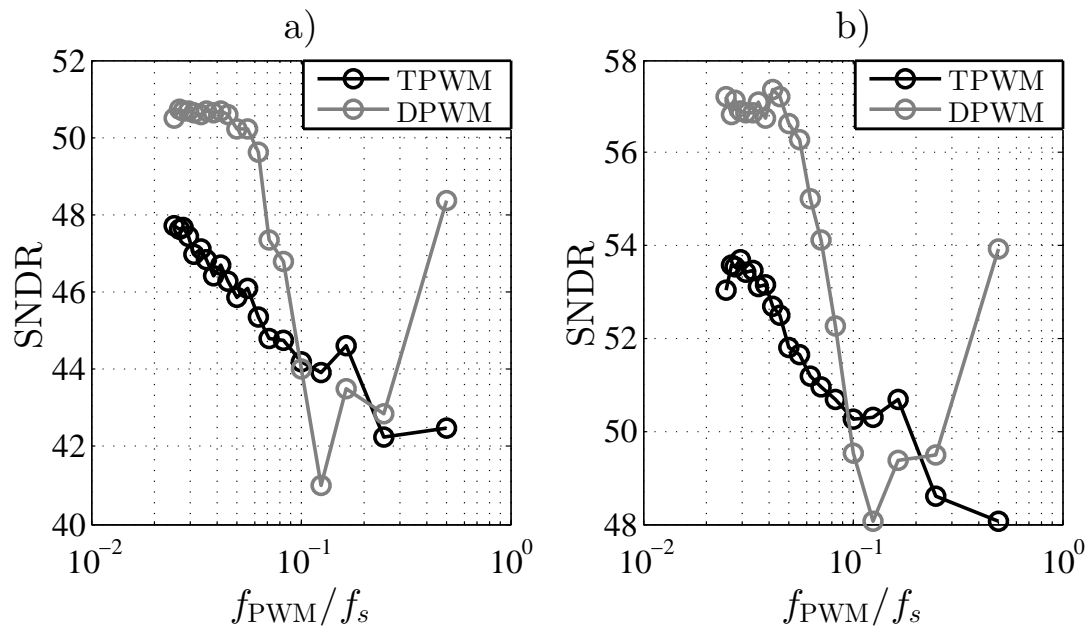


FIGURE 3.13: SNDR evaluated for various f_{PWM} settings for a) sinusoidal sequence and b) LTE sequence.

The influence of f_{PWM} on the SNDR is shown in Figure 3.13 for $f_{\text{PWM}} = f_s/k$, where $k = [2, 40]$. Due to fixed f_s , the amount of in-band aliasing products is high due to low duty cycle resolution for large f_{PWM} . This leads to worse SNDR,

which is clearly the case for both modulation schemes and excitation sequences. On the other hand, an improved distortion performance is obtained by decreasing f_{PWM} . However, as pointed out later in sub-section 3.3.2, for a specific f_s setting the average pulse repetition rate increases rapidly with decreasing f_{PWM} and thus, ultimately leading to an encoding that deviates significantly from PWM. This explains the rapid improvement in SNDR for $f_{\text{PWM}} > f_s/12$ especially in the case of DPWM.

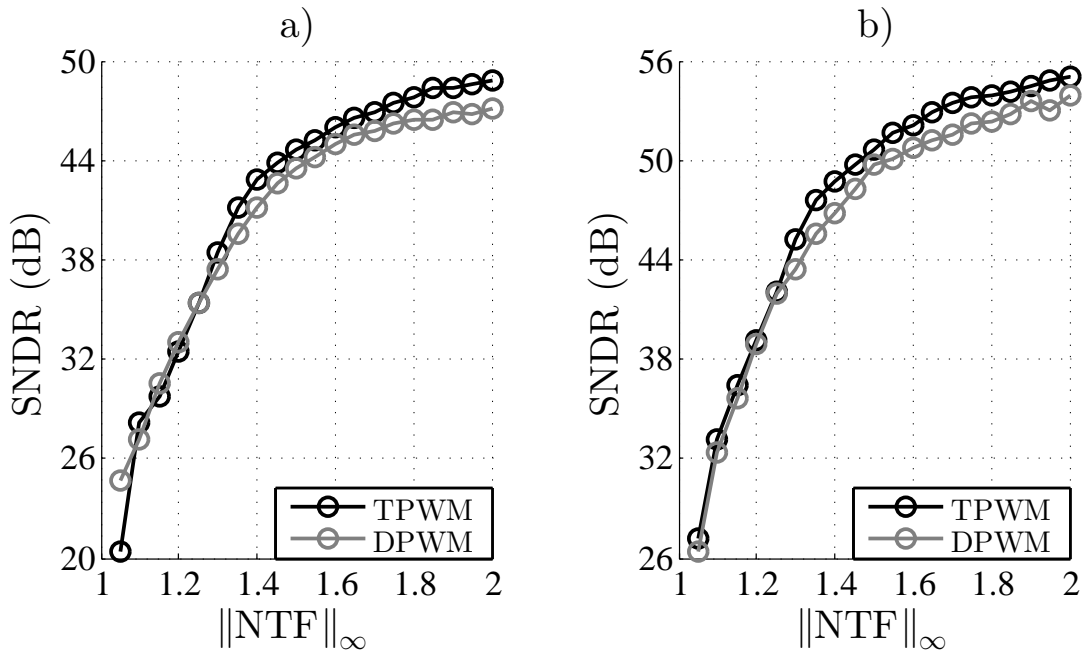


FIGURE 3.14: SNDR evaluated for various $|NTF(z)|_\infty$ settings for a) sinusoidal sequence and b) LTE sequence.

Finally, the dependency of noise shaping performance on $|NTF(z)|_\infty$ was studied by evaluating SNDR for $|NTF(z)|_\infty = [1.05, 2]$. For the chosen 2nd order Chebyshev type NTF the results are illustrated in Figure 3.14. Obviously, the relation is non-linear for the given range and, therefore, for $|NTF(z)|_\infty > 1.4$ the obtained improvement in SNDR at the expense of increased out-of-band noise gain becomes smaller. On the other hand, as $|NTF(z)|_\infty$ grows, so does the magnitude of the complex valued PWM input. Eventually, the PWM operators are driven into over-modulation, which causes a compressive effect on the noise shaped quantization noise. This in the end leads to a reduced SNDR. Moreover, it is visible that TPWM yields improvement between 0-2.5 dB in comparison to DPWM.

3.3.2 Average pulse repetition rate

In digital open-loop PWM based modulators the PWM duty cycles are obtained always for a single PWM carrier cycle at a time. Therefore, the corresponding pulse rates per real valued input sequences are known in advance as well. In contrast to the open-loop modulators, the closed loop based PWM modulators including QΣΔPWM determine the PWM output one bit symbol at a time. Hence, as it turns out, certain combinations of QΣΔPWM parameter settings lead to an encoding with more than one pulse transitions per PWM cycle. Although this undesired modulator behavior is clearly in contradiction to the original definition of PWM, in the noise shaped encoder performance point of view, the operation with multiple transitions is admissible. As long as the spectrum of the pulse encoded complex valued baseband sequence over the signal band fulfils the given design criterion, the encoder is performing its task as desired. However, since one of the main motivations to utilize PWM is to decrease the number of pulse transitions per time unit, it is relevant to find out how the different settings affect the output of the QΣΔPWM in time domain. For this reason, a unit of measure for pulse transition investigation called average pulse repetition ratio (APRR) is defined as follows

$$\text{APRR} = \text{APR} \frac{f_s}{f_{\text{PWM}}}, \quad (3.14)$$

where APR denotes the average pulse rate. In digital domain the evaluation of APR for a real valued PWM sequence can be easily performed by interpreting translating the digital pulsed sequences into binary sequences and counting the average of the rising pulse edges as follows

$$\text{APR} = \frac{\frac{1}{2}(\text{pwm}_r(n) + 1) [\frac{1}{2}(\text{pwm}_r(n) + 1) - \frac{1}{2}(\text{pwm}_r(n-1) + 1)]}{l_{\text{PWM}}}, \quad (3.15)$$

where $\text{pwm}_r(n)$ denotes a finite length real valued PWM sequence and l_{PWM} the length of the PWM sequence. From (3.14) it can be easily interpreted that $\text{APRR} = 1$ applies for PWM with strictly one single transition per carrier cycle.

Obviously for PWM with multiple transitions per carrier cycle, $APRR > 1$. Further, over-modulation, where no pulse transition occurs for certain PWM cycles, may lead to $APRR < 1$.

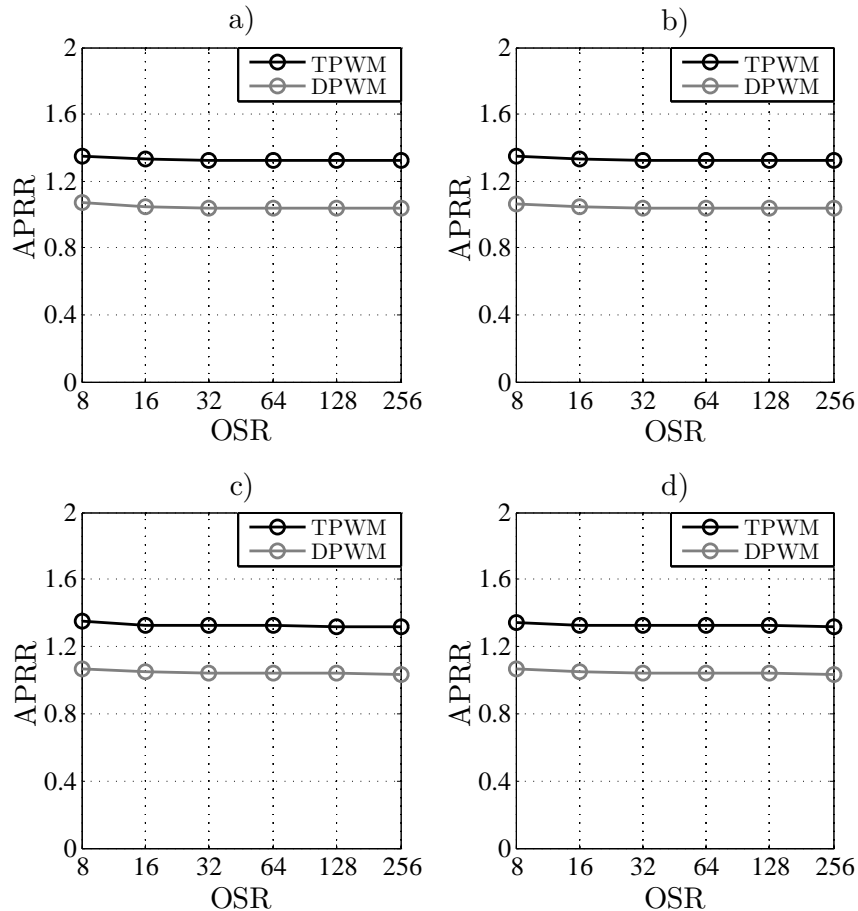


FIGURE 3.15: APRR evaluated for various OSR settings for a) real and b) imaginary parts of the sinusoidal sequence and c) real and d) imaginary parts of the LTE sequence.

At first the APRR was evaluated for various OSR settings. As visible in Figure 3.15, the obtained results for real and imaginary parts of the input sequences are nearly equal regardless of the OSR and furthermore, independent on the type of the excitation. The modulator noise shaper settings combined with the chosen f_{PWM} causes $APRR > 1$. However, it can be observed that the utilization of DPWM yields an improved APRR. This is understandable, since as explained in Section 3.1.1, except for possible multi-transitions, there are no pulse transitions in between the carrier cycles, and thus, the amount of individual pulses is reduced.

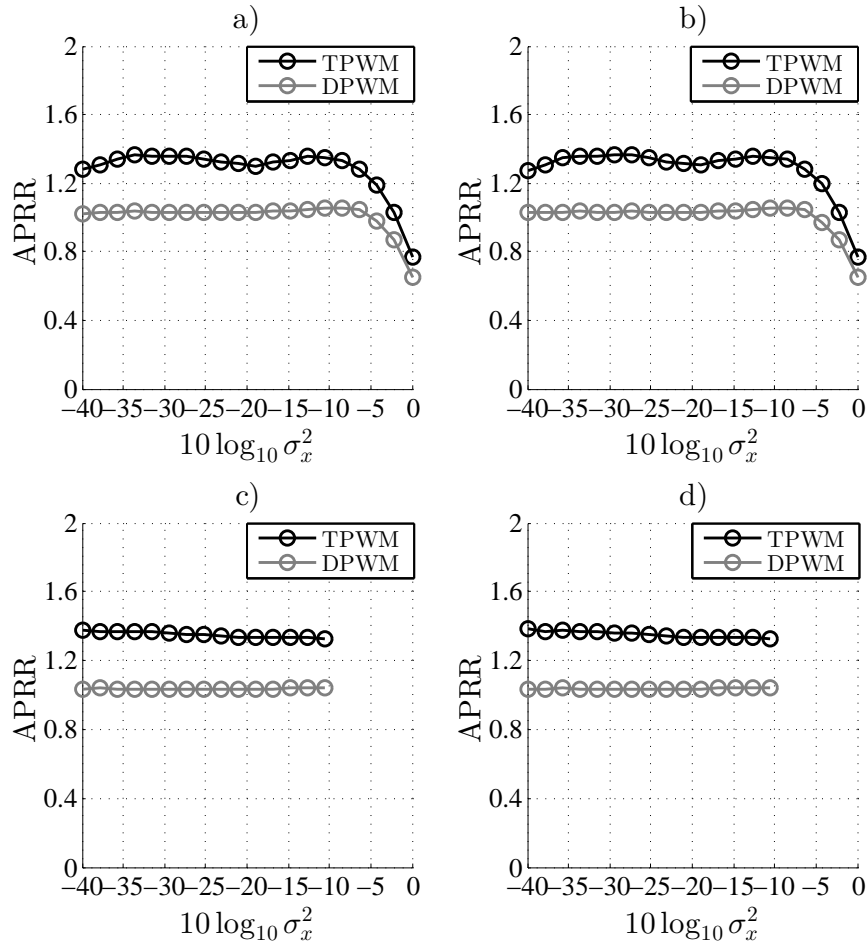


FIGURE 3.16: APRR evaluated for various σ_x^2 settings for a) real and b) imaginary parts of the sinusoidal sequence and c) real and d) imaginary parts of the LTE sequence.

The APRR dependency of σ_x^2 is illustrated in Figure 3.16. From the nearly constant APRR for both excitations and modulation types between $-40\text{dB} < 10\log_{10}\sigma_x^2 < -10\text{dB}$, it can be interpreted that the input sequence has only a minor effect on APRR. For the sinusoidal excitation, $10\log_{10}\sigma_x^2 > -10\text{dB}$ brings the modulator into state of over modulation, which in turn decreases APRR. This effect may be utilized for low PAPR excitations to reduce APRR. However, as stated before, the over modulation comes at the cost of increased harmonic distortion.

The strong effect of noise shaping parameters on APRR is clarified in Figure 3.17 where APRR is evaluated as a function of $|\text{NTF}(z)|_\infty$. It can be observed that already above $|\text{NTF}(z)|_\infty = 1.2$ multi-transitions occur for the TPWM based modulator. By comparing the given APRR values with the corresponding SNDR values

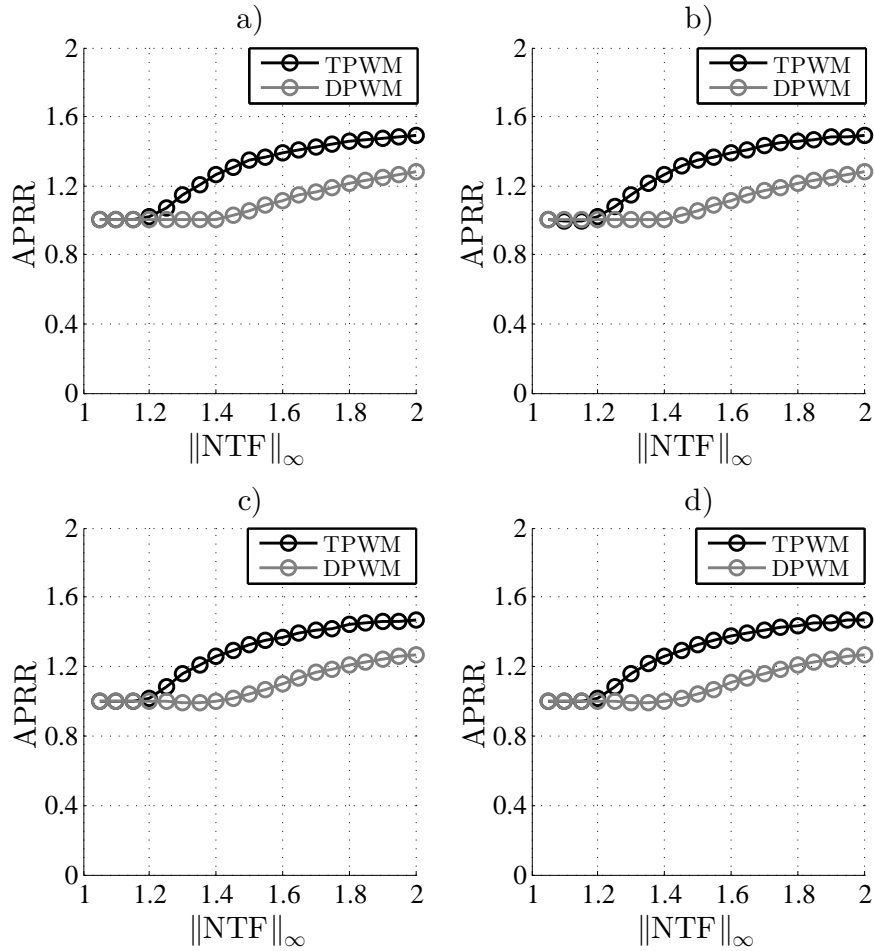


FIGURE 3.17: APRR evaluated for various $|NTF(z)|_\infty$ settings for a) real and b) imaginary parts of the sinusoidal sequence and c) real and d) imaginary parts of the LTE sequence.

from Figure 3.14, it can be deduced that since the relation between $|NTF(z)|_\infty$ and the noise shaping performance is nonlinear, so is also the relation between $|NTF(z)|_\infty$ and APRR. In contrast to TPWM, the DPWM modulator shows $APRR \approx 1$ up to approximately $|NTF|_\infty = 1.4$.

Figure 3.18 demonstrates the APRR behavior for $-0.5f_s \leq f_{IF} \leq 0.5f_s$ settings. Rather unexpectedly, the slope of the APRR shows both increasing and decreasing characteristics for both real and imaginary components of the encoded sequences even though the highest frequency component of the excitation sequence is located beyond the lowest frequency component of the PWM carrier wave. This can be explained by the real valued sub-filters of the complex valued NTF affecting the real and the imaginary components of the modulator output. The distinct

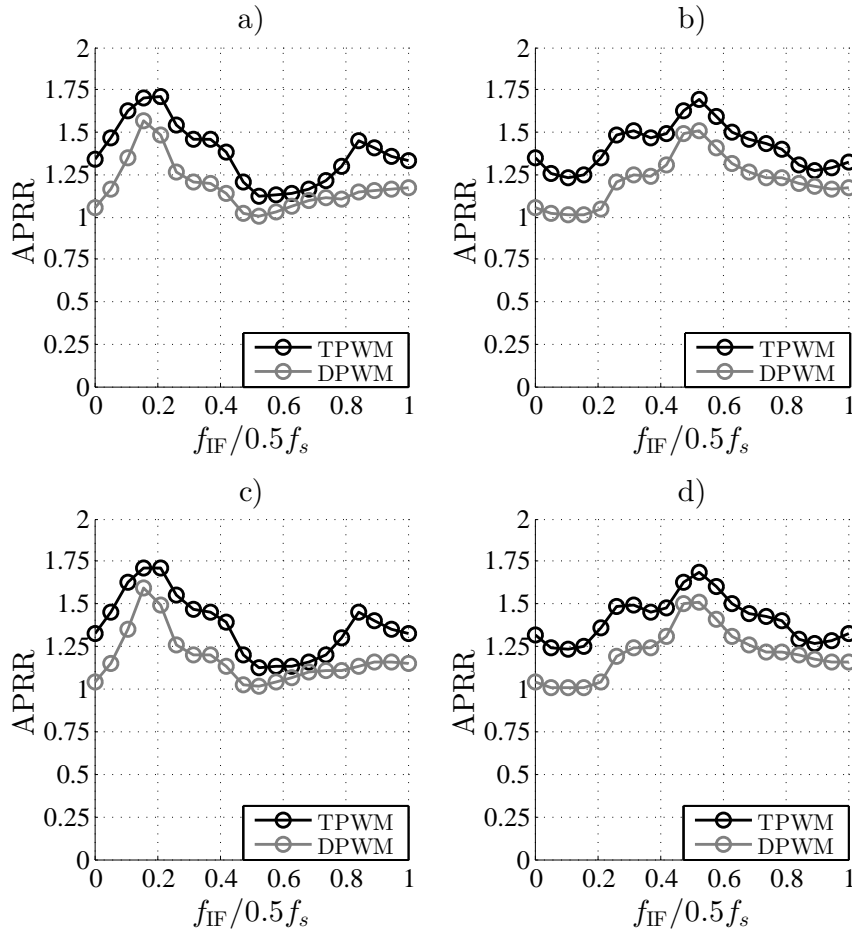


FIGURE 3.18: APRR evaluated for various f_{IF} settings for a) real and b) imaginary parts of the sinusoidal sequence and c) real and d) imaginary parts of the LTE sequence.

phase and magnitude characteristics of the sub-filters yield a noise shaping effect dependent on the particular f_{IF} setting on the digital PWM. Since the transition band of the 2nd order NTF for the chosen OSR is relatively wide, the APRR is degraded over a large f_{IF} tuning range. Moreover, by comparing Figures 3.18 a)-b) with Figures 3.18 c)-d) it becomes obvious that the given APRR values are nearly independent of the excitation. This observation further consolidates the general argument that the choice of NTF affects the APRR the most.

Finally, it was investigated how the choice of f_{PWM} affects the APRR for the given modulator settings. From the results for the real and the imaginary components of the modulator output, given in Figure 3.19, only the last four settings ($f_{PWM} = f_s/2, f_s/4, f_s/6, f_s/8$) yield a PWM performance with $APRR < 2$. Referring to

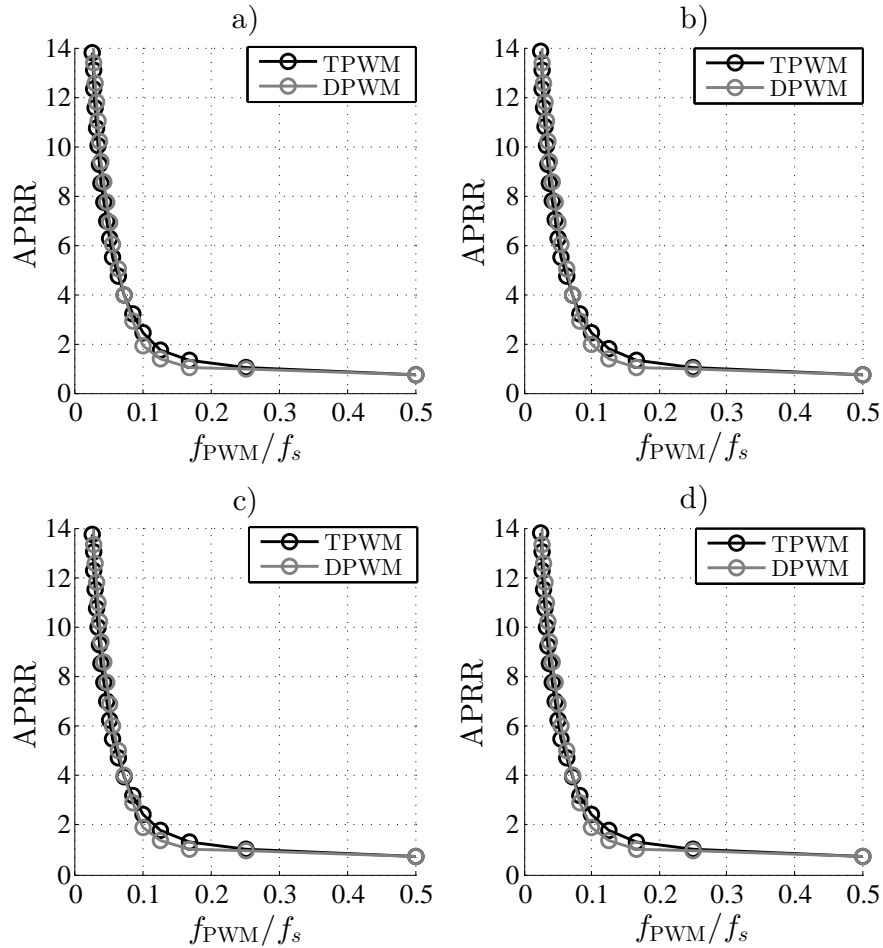


FIGURE 3.19: APRR evaluated for various f_{PWM} settings for a) real and b) imaginary parts of the sinusoidal sequence and c) real and d) imaginary parts of the LTE sequence.

the SNDR analysis the effect of the noise shaping affects significantly the digital PWM, which leads to a decreased APRR. In order to evaluate a pulse rate relative to a fixed time unit, APR was additionally evaluated. The results depicted in Figure 3.20. indicate that the lowest overall pulse transition rate can be obtained for $f_s/8$.

3.3.3 Stability analysis

According to the numerous simulation runs, the 2^{nd} order Q $\Sigma\Delta$ PWM modulator exhibits correct behavior in terms of SNDR for various excitations and modulator settings. However, according to the theory of $\Sigma\Delta$ modulators, the desired

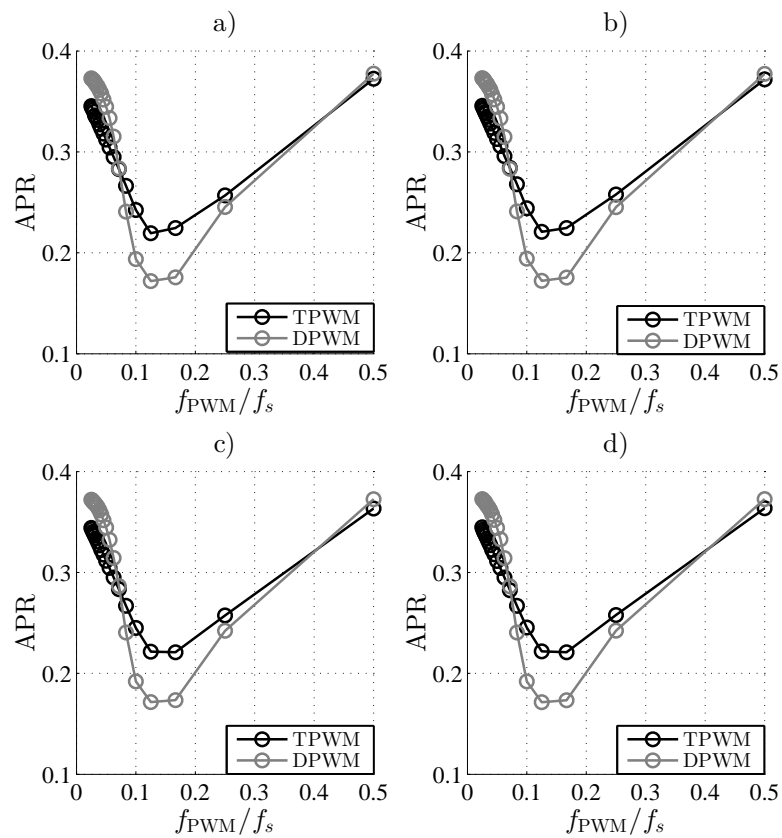


FIGURE 3.20: APR evaluated for various f_{PWM} settings for a) real and b) imaginary parts of the sinusoidal sequence and c) real and d) imaginary parts of the LTE sequence.

condition where a linear filter can be used to reconstruct the transmission signal cannot be guaranteed for arbitrary excitations or modulator parameters [72]. Due to the nonlinear dynamical characteristics of the $\text{Q}\Sigma\Delta\text{PWM}$ loop structure, a modulator state, where the amplitude of the input to the PWM operators grows unboundedly over time, can occur for particular modulator settings independent of the chosen NTF. Hence, the resulting two-level modulation becomes heavily distorted. In engineering literature this undesired condition is commonly referred to as modulator instability. In the case of $\text{Q}\Sigma\Delta\text{PWM}$ as a part of pulsed RF signal conversion in a RF transmitter, the modulator instability is catastrophic. Even a slight increase in distortion due to a malfunctioning modulator will lead to an increased in-band and adjacent channel distortion, which in turn falsifies the modulation scheme of the transmission signal. In the worst case, the instability leads to significant information loss as the wireless communication is blocked for

multiple users. Therefore, it is a demand to investigate the possible causes of the modulator instability. In literature a multitude of methods have been given to

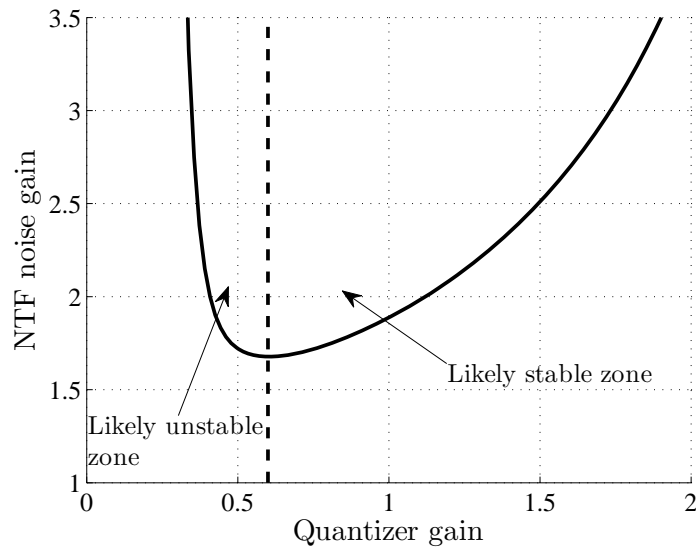


FIGURE 3.21: Example function of $A(K)$ plotted as a function of K for a 4th order NTF.

analyze the stability of $\Sigma\Delta$ loop structures [72–74]. In general, for modulators utilizing NTFs with $N \leq 2$ analytical parameter bounds for modulator stability exist. For higher order NTFs with $N > 2$, the analysis becomes more complicated and hence, the stability analysis methods for this type of modulators are often based on numerical simulations [27]. On the other hand, this means that for the higher order NTF based modulators, the simulation based stability bounds at best are approximations and that additional simulations with realistic excitations are required to ensure the modulator functionality. One of the most often applied approximate rule for $\Sigma\Delta$ modulators is a so called Lee’s rule [75], which simply states that when $|\text{NTF}|_\infty < 2$ the corresponding modulator is likely stable. This constraint for NTF, however, has been shown to be very conservative for stability prediction [64] and that more elaborate analysis shall be used instead. Indeed, it is questionable whether such $\Sigma\Delta$ stability analysis guidelines apply also for a larger family of noise shaped encoders including Q $\Sigma\Delta$ PWM.

In the following, the stability of the Q $\Sigma\Delta$ PWM is studied by means of linearized modeling techniques [76]. The substitution of the digital PWM operators by a

combination of a complex valued noise source and a linear gain element led to a convenient tool to inspect distortion behavior of the modulator. According to the theory of digital linear invariant systems, the bounded-input-bounded-output (BIBO) stability of such linearized models can be guaranteed if the poles of the NTF are inside the unit circle. The range of quantizer gains for which this property holds can be easily verified for an arbitrary NTF by evaluating $\frac{1}{1+KL_1(z)}$ for various K and subsequently by calculating the magnitudes of the poles. The next logical step in stability analysis would be to extract the quantizer gain for Q $\Sigma\Delta$ PWM. Since an exact analytical relation of the quantizer gain and the closed loop PWM type modulators is to the author's best knowledge at this date not available, the quantizer gain has to be estimated from simulated data. The minimum mean square estimate [76] for a real valued K reads

$$K = \frac{E[y(n)\text{pwm}(n)]}{\sigma_y^2}, \quad (3.16)$$

where $E[.]$ denotes the expectation operation and σ_y^2 the variance of $y(n)$, respectively. Next, the gain of the quantization noise $A(K)$ due to the variable K can be defined as

$$A(K) = \frac{E[\text{pwm}(n)]^2}{\sigma_e^2}, \quad (3.17)$$

where σ_e^2 denotes the variance of $e(n)$ in the linearized model. This function allows for an approximate analysis on how the modulator with a specific NTF responds to different quantizer gains. An exemplary illustration of (3.17) is given in Figure 3.21 for a 4th order NTF with $OSR = 32$, $|NTF|_\infty = 1.25$ and $0 < K < 2$.

With the help of the illustration, the instability of the modulator can be explained as follows. Given a possible scenario where a modulator yields K between 1.5-2 results in higher NTF noise gain. For the next modulator cycles, the subsequent values of K for two-level modulation are likely to decrease, which in turn reduces $A(K)$. If this kind of quantizer gain behavior can be ensured for all modulator cycles, then it can be stated that the corresponding modulator is stable. On the contrary, if a K for which the derivative of (3.17) becomes negative is obtained, likelihood for modulator instability rises. In such a case, the following K values

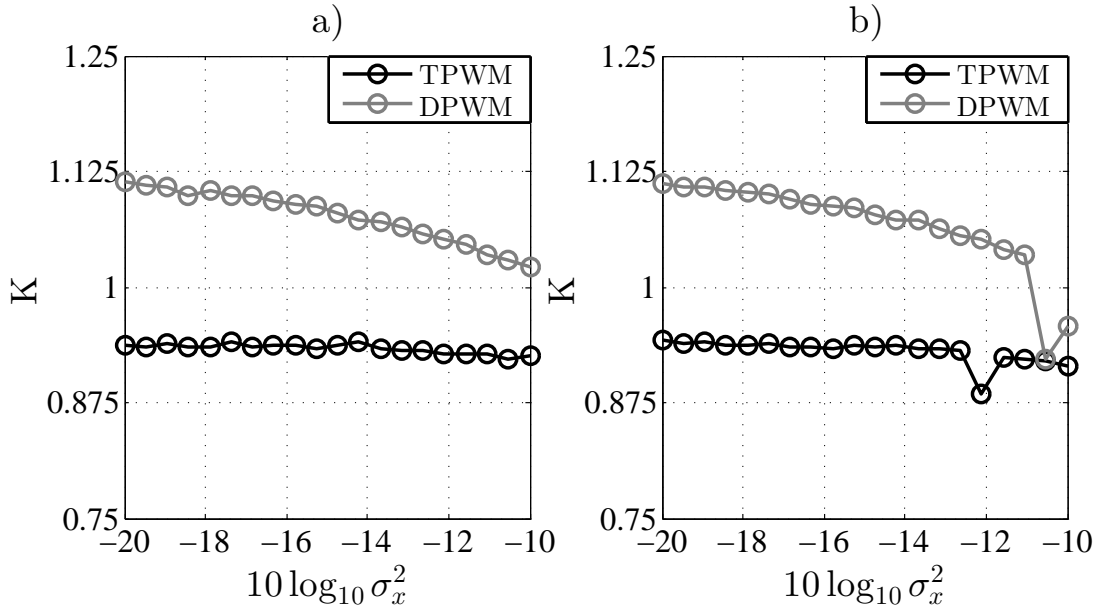


FIGURE 3.22: Estimates of K for a) sinusoidal sequence and b) LTE sequence evaluated for various σ_x^2 .

shall increase in order to decrease $A(K)$. However, for two-level modulation the opposite is more likely to happen, which in the end leads to modulator instability due to a vicious circle of decreasing K and thus, exponentially increasing $A(K)$. The real and imaginary quantizer gain values for $-20 < 10\log_{10}\sigma_x < -10$ were evaluated by utilizing the given 4th order NTF. The results for real and imaginary components of the encoded LTE and the sinusoidal excitations are depicted in Figure 3.22. The main result is that the quantizer gains are very close the unstable zone regardless of the excitation sequence power back-off. Hence, the modulator at hand is more likely to become unstable, even though $|NTF|_\infty < 2$, which clearly is in contradiction to Lee's rule.

3.4 Summary

This Chapter discussed different variants of digital PWM. It became obvious that the conventional digital PWM is a less suitable encoding method for center frequency agile digital transmitters. By employing noise shaped encoding techniques, the Q $\Sigma\Delta$ PWM with an enhanced signal band distortion power was designed. The

novel modulator enables also optimization of quantization noise power for variable f_{IF} . Thus, as the encoded complex baseband sequences are up-converted to a pulsed RF sequence, a very wide f_c tuning range is enabled. The following attributes of the encoding technique shall be underlined

- With the help of the encoding in over-sampled complex baseband the already available re-configurable hardware resources can be utilized for the encoding.
- The obtained SNDR estimates are promising in terms of applying the modulator for mobile communication purposes. With increasing hardware clock rates, even higher f_s and OSRs become available, which in turn facilitates the design of digital transmitters compatible with the stringent signal linearity constraints of the wireless standards.
- The performance analysis revealed some important properties of the novel modulator. The first finding is that the SNDR behavior is nearly independent of the modulator input. Conversely, the selection of the NTF has the most significant effect on the noise shaping. In fact, it was observed that a reduction in N_p does not yield a linear increment in SNDR. Furthermore, the selection of the NTF affects the digital PWM as well. It was observed that some specific NTFs lead to additional pulse transitions in PWM cycles. This leads to an undesired increase in APRR.
- Finally the stability of Q $\Sigma\Delta$ PWM was studied. The results suggest that in contrary to $\Sigma\Delta$ modulators the Q $\Sigma\Delta$ PWM modulator does not fulfil the popular Lee's rule. Hence, lower order conventional NTFs shall be utilized for closed loop PWM modulators.

Chapter 4

Enhanced digital up-conversion methods

The second operational block of the quadrature digital transmitter up-converts an encoded quadrature sequence to an RF sequence in digital domain. When the digital up-conversion is utilized together with a quadrature encoder such as Q Σ Δ PWM, [the carrier frequency](#) f_c can be adjusted by selecting f_{IF} accordingly. However, as learned later on, the SNDR of the RF symbol sequences deviates from the value of the encoded complex baseband sequences as $f_{IF} > 0$. In this Chapter the mechanism for the harmful distortion is analyzed and based on this, suitable compensation techniques are developed.

4.1 Quadrature imbalance problem

Despite the very low computational costs, the digital up-conversion technique suffers from inherent quadrature imbalance, which degrades the signal band dynamic range and thus limits the f_c agility of the transmitter system. The imbalance effect can be easily understood by interpreting the multiplications by $I_{LO}(n)$ and $Q_{LO}(n)$ as sub-subsequent sampling and modulating operations for $y_u(n)$. Since the sampling of the $y_{u,Q}(n)$ is performed with a phase lag of $\pi/4$ in comparison with

$y_{u,I}(n)$, there is a constant phase imbalance between the quadrature components. It shall be noted that this phase imbalance mechanism arises in digital second order sampling schemes used in digital receiver architectures [77] as well. Despite the fact that the digital up-conversion is a popular technique in digital transmitter systems, the related imbalance problem is still less known.

In order to understand the role of the quadrature imbalance for the encoded sequences it makes sense to analyze the digital up-conversion technique in frequency domain. Firstly (2.5) can be reformulated by utilizing complex valued representations of the real valued sequences $y_{u,I}(n)$, $y_{u,Q}(n)$, $I_{LO}(n)$ and $Q_{LO}(n)$ as follows

$$p(n) = \frac{1}{2j} [e^{-jn\pi/2}y_u(n) - e^{jn\pi/2}y_u^*(n)] * h_{ma}(n) \quad (4.1)$$

for which the equivalent frequency domain formula becomes

$$P(j\omega) = \frac{1}{2j} [Y_u(j(\omega - \pi/2)) - Y_u^*(j(\omega + \pi/2))]H_{ma}(j\omega) \quad (4.2)$$

The result is the well-known fact that the spectrum of a real valued sequence is conjugate symmetric. This analysis yields also important knowledge of the digital up-conversion. On the one hand, it is desired that the content of $y_u(n)$ remains intact during the up-conversion process. This condition can be easily guaranteed for band-limited sequences as follows. If the bandwidth of $Y_u(j\omega)$ is less than $f_{sw}/2$, the spectral content of $Y_u(j(\omega - \pi/2))$ and $Y_u(j(\omega + \pi/2))$ is zero between $[0, -\pi]$ and $[0, \pi]$, respectively. Thus, after summation in order to obtain the real valued sequence, $Y_u(j(\omega - \pi/2))$ and $Y_u^*(j(\omega + \pi/2))$ do not overlap. However, as explained in Chapter II, the QΣΔPWM modulated sequences contain significant amount of PWM harmonics covering nearly the entire Nyquist range. Hence, after up-conversion part of $Y_u^*(j\omega)$ is located in the signal band. In the context of digital up-conversion this phenomenon will be referred to as *conjugate quantization noise folding*¹. Further, the undesired spectral content contributed by the conjugate image will be referred to as *conjugate quantization noise*.

¹The quantization noise in the context of digital up-conversion denotes the distortion products stemming contributed by noise shaped encoding, regardless of the type of encoding.

4.2 Baseband modeling of digital up-conversion

Given that the pulsed encoding is applied for complex baseband sequences, it is of importance to describe the conjugate quantization noise folding in the complex baseband as well.

A baseband representation of the digital up-conversion can be obtained by shifting the frequency domain formulation of the pulsed RF sequence (4.2) by $\pi/2$, which yields the following baseband description

$$P(j\omega) = \frac{1}{2j} [Y_u(j\omega) - Y_u^*(j(\omega + \pi))] H_{ma}(j\omega). \quad (4.3)$$

The respective time-domain formulation thus becomes

$$p_m(n) = \frac{1}{2j} [y_u(n) - e^{jn\pi} y_u^*(n)] * h_{ma}(n). \quad (4.4)$$

In a fashion similar to the linearized noise shaped encoder model (2.1), the complex valued sequence $y_u(n)$ can be divided into a signal part $x_u(n)$ and a quantization noise part $b_u(n)$. Hence, similar to above analysis, translation of these components leads to

$$p_m(n) = x_m(n) + b_m(n), \quad (4.5)$$

where

$$x_m(n) = \frac{1}{2j} [x_u(n) - e^{jn\pi} x_u^*(n)] * h_{ma}(n) \quad (4.6)$$

and

$$b_m(n) = \frac{1}{2j} [b_u(n) - e^{jn\pi} b_u^*(n)] * h_{ma}(n). \quad (4.7)$$

In practice, the transmission signal contained in $x_u(n)$ is band-limited and due to over-sampling its spectral power is spread over a relatively narrow bandwidth. Henceforth, the signal conjugate image $x_u^*(n)$ in (4.6) is harmful only for limited f_θ settings. On the other hand, as a result of noise shaped encoding $b_u(n)$ contains spectral content over the entire Nyquist frequency range. Therefore, $b_u^*(n)$ becomes an interferer during the digital up-conversion and, as discussed earlier,

the consequences become much more severe from a signal band dynamic range point of view.

In (4.6) and (4.7), the non-conjugate and the conjugate versions of the signal and noise sequences are affected by $h_{ma}(n)$, which effectively is a finite impulse response (FIR) filter with an impulse response given by

$$h_{ma}(n) = \begin{cases} 1, & 0 \leq n \leq R_s - 1 \\ 0, & n \geq R_s. \end{cases} \quad (4.8)$$

The frequency response of this moving average type filter can be expressed in closed form as follows

$$H_{ma}(j\omega) = \frac{(1 - e^{-j\omega R_s})}{(1 - e^{-j\omega})}. \quad (4.9)$$

On the other hand the modulation operation $e^{jn\pi}$ followed by the convolution with $h_{ma}(n)$ in (4.7) and (4.6) can be substituted by another FIR filter $h_{ma,c}(n)$ with a following impulse response

$$h_{ma,c}(n) = \begin{cases} (-1)^n, & 0 \leq n \leq R_s - 1 \\ 0, & n \geq R_s. \end{cases} \quad (4.10)$$

This enables reformulation of the complex baseband models into representations of linear quadrature imbalance for complex valued input sequences. By further recognizing that since $e^{jn\pi}x_u^*(n) = x_u^*(n)$ and $e^{jn\pi}b_u^*(n) = b_u^*(n)$ for even valued R_s , i.e. $R_s = R_e$ (4.7) and (4.6) can be rewritten as

$$x_m(n) = \frac{1}{2j} [x_u(n) * h_{ma,e}(n) - x_u^*(n) * h_{ma,e,c}(n)] \quad (4.11)$$

and

$$b_m(n) = \frac{1}{2j} [b_u(n) * h_{ma,e}(n) - b_u^*(n) * h_{ma,e,c}(n)], \quad (4.12)$$

where $h_{ma,e}(n)$ and $h_{ma,e,c}(n)$ denote $h_{ma}(n)$ and $h_{ma,c}(n)$ for $R_s = R_e$, respectively.

On the other hand in case of odd valued R_s , i.e. $R_s = R_o$ the following equalities hold $e^{jn\pi}x_u^*(n) = e^{jn\pi/R_o}x_u^*(n)$, $e^{jn\pi}b_u^*(n) = e^{jn\pi/R_o}b_u^*(n)$. Thus (4.7) and (4.6) for

R_o settings become

$$x_m(n) = \frac{1}{2j} [x_u(n) * h_{ma,o}(n) - e^{jn\pi/R_o} x_u^*(n) * h_{ma,o,c}(n)] \quad (4.13)$$

and

$$b_m(n) = \frac{1}{2j} [b_u(n) * h_{ma,o}(n) - e^{jn\pi/R_o} b_u^*(n) * h_{ma,o,c}(n)], \quad (4.14)$$

where $h_{ma,o}(n)$ and $h_{ma,o,c}(n)$ denote $h_{ma}(n)$ and $h_{ma,c}(n)$ for $R_s = R_o$, respectively.

Similar to (4.9) closed form frequency response expressions for $h_{ma,c,e}(n)$ and $h_{ma,c,o}(n)$ can be found as follows

$$H_{ma,c,e}(j\omega) = \frac{(1 - e^{-j\omega R_e})}{(1 + e^{-j\omega})} \quad (4.15)$$

and

$$H_{ma,o,c}(j\omega) = \frac{(1 - e^{-j\omega} + e^{-j\omega R_o} - e^{-j\omega R_o + 1})}{(1 - e^{-j2\omega})}. \quad (4.16)$$

With these expressions the frequency responses for (4.11) and (4.12) on the one hand in case of R_e become

$$X_m(j\omega) = \frac{1}{2j} [X_u(j\omega)H_{ma,e}(j\omega) - X_u^*(-j\omega)H_{ma,e,c}(n)] \quad (4.17)$$

and

$$B_m(j\omega) = \frac{1}{2j} [B_u(j\omega)H_{ma,e}(j\omega) - B_u^*(-j\omega)H_{ma,e,c}(n)]. \quad (4.18)$$

Further, for R_o the respective expressions for (4.13) and (4.14) read

$$X_m(j\omega) = \frac{1}{2j} [X_u(j\omega)H_{ma,o}(j\omega) - X_u^*(-j(\omega + \pi/R_o))H_{ma,o,c}(j\omega)] \quad (4.19)$$

and

$$B_m(j\omega) = \frac{1}{2j} [B_u(j\omega)H_{ma,o}(j\omega) - B_u^*(-j(\omega + \pi/R_o))H_{ma,o,c}(j\omega)]. \quad (4.20)$$

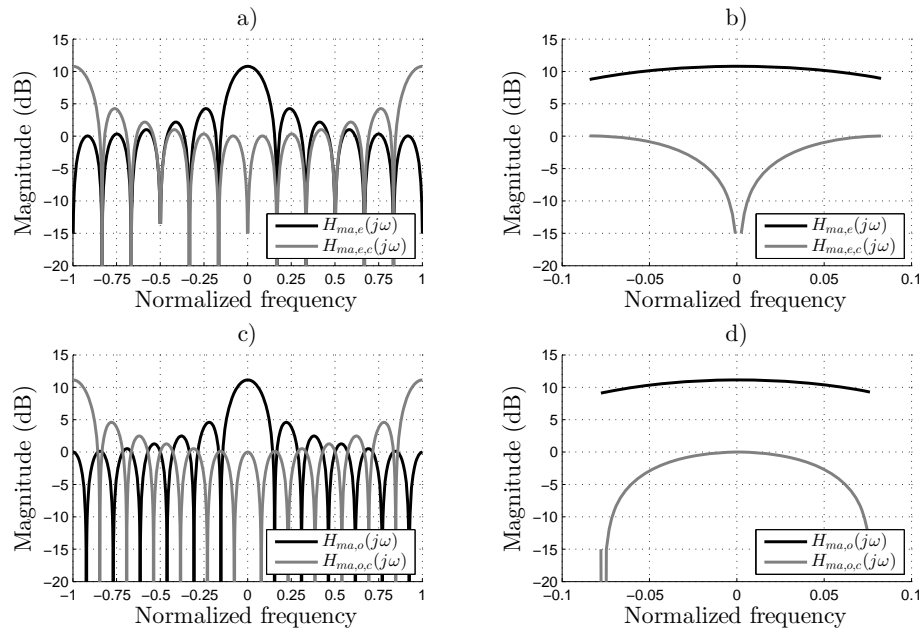


FIGURE 4.1: Magnitude responses of a) $H_{ma,e}(j\omega)$ and $H_{ma,e,c}(j\omega)$ over the pulsed RF sequence bandwidth b) $H_{ma,e}(j\omega)$ and $H_{ma,e,c}(j\omega)$ over the complex baseband bandwidth c) $H_{ma,o}(j\omega)$ and $H_{ma,o,c}(j\omega)$ over the pulsed RF sequence bandwidth and d) $H_{ma,o}(j\omega)$ and $H_{ma,o,c}(j\omega)$ over the complex baseband bandwidth, where $R_e = 12$ and $R_o = 13$.

In order to explain the role of the digital hold operation represented by $h_{ma}(n)$ in digital up-conversion for the two individual R_s settings, the magnitude responses of $H_{ma,e}(j\omega)$, $H_{ma,e,c}(j\omega)$, $H_{ma,o}(j\omega)$ and $H_{ma,o,c}(j\omega)$, where $R_e = 12$ and $R_o = 13$ are illustrated in Figure 4.1. By examining Figure 4.1 a) and b) more closely, it can be observed that $H_{ma,e,c}(j\omega)$ provides attenuation around DC. This property has been exploited in various digital RF pulse modulators, where typically LP $\Sigma\Delta$ modulators are utilized for encoding purposes. In order to enable a larger f_c tuning range, the noise shaping can be performed around f_{IF} in complex domain as explained in section 3.2.2. However, since the attenuation of $|H_{ma,e,c}(j\omega)|^2$ decreases rapidly when the band of interest is moved towards positive or negative frequencies, the gain in dynamic range due to complex valued noise shaped encoding is lost due to the conjugate quantization noise folding. Contrary to R_e settings the R_o settings provide no attenuation at DC as shown in Figure 4.1 c) and d). This means that for the conventional scenario, where the f_{IF} and f_θ locate near DC, the impact of $b_u^*(n)$ becomes significant. In this case, the best choice would be to place the signal

band near $\pm\pi/R_o$, where $H_{ma,o,c}(j\omega)$ provides the largest attenuation. However, due to the frequency translation of $x_u^*(n)$ in (4.19) the excitation sequence itself becomes an interferer for these settings, which may turn out to be problematic especially if the average signal power is high. Relying on the presented analysis, it can be concluded that generation of pulsed RF sequences by a combination of baseband encoder and conventional digital up-conversion technique allows only a limited f_c tuning range.

4.3 Conjugate quantization noise compensation

The analysis of the digital up-conversion procedure revealed that the method suffers from an inherent quadrature imbalance problem, which degrades the dynamic range of the transmit signal and, therefore, limits the f_c tuning for the digital transmitter. Thus, it is highly relevant to study ways to encounter this problem. On the one hand, the possible solutions shall not change the form of the output sequence from the original two-level pulsed format. On the other hand, the potential implementations shall be implementable with the available hardware resources.

Commonly discrete time quadrature imbalance problems that can be expressed by a linear model can be alleviated by a compensating system, which performs a phase and/or a magnitude equalization to the real valued components of the input sequence [78]. With the compensating system placed either in front or after the imbalanced system, the output of the two sub-sequent units results in suppression of the conjugate image. A second possible solution for compensation is to suppress the conjugate signal content from the input sequence. In the following, such compensating techniques are presented for the digital up-conversion baseband models.

4.3.1 Delay based compensation method

In case of R_e the quadrature imbalance can be represented by a pair of filters operating on the original sequence and its conjugate image as given in (4.18). Alternatively, a complex valued system can be expressed by its real valued components. Thereby with $Re\{B(j\omega)\} = \frac{1}{2}[B(j\omega) + B^*(j\omega)]$ and $Im\{B(j\omega)\} = \frac{1}{2j}[B(j\omega) - B^*(j\omega)]$ (4.18) becomes

$$\begin{aligned}
B_{m,e}(j\omega) &= \frac{1}{4j} [B(j\omega)H_{ma,e}(j\omega) + B^*(-j\omega)H_{ma,e}(j\omega)] \\
&+ \frac{1}{4j} [B(j\omega)H_{ma,e}(j\omega) - B^*(-j\omega)H_{ma,e}(j\omega)] \\
&- \frac{1}{4j} [B^*(-j\omega)H_{ma,e,c}(j\omega) + B(j\omega)H_{ma,e,c}(j\omega)] \\
&- \frac{1}{4j} [B^*(-j\omega)H_{ma,e,c}(j\omega) - B(j\omega)H_{ma,e,c}(j\omega)].
\end{aligned} \tag{4.21}$$

Given that a pre-compensating system has the following frequency domain description $P_{comp}(j\omega) = \alpha(j\omega) + j\beta(j\omega)$ the combination of $P_{comp}(j\omega)$ and $B_{m,e}(j\omega)$ reads

$$\begin{aligned}
B_{m,e,eq}(j\omega) &= \frac{1}{4j}\alpha(j\omega) [B(j\omega)H_{ma,e}(j\omega) + B^*(-j\omega)H_{ma,e}(j\omega)] \\
&+ \frac{1}{4j}\beta(j\omega) [B(j\omega)H_{ma,e}(j\omega) - B^*(-j\omega)H_{ma,e}(j\omega)] \\
&- \frac{1}{4j}\alpha(j\omega) [B^*(-j\omega)H_{ma,e,c}(j\omega) + B(j\omega)H_{ma,e,c}(j\omega)] \\
&- \frac{1}{4j}\beta(j\omega) [B^*(-j\omega)H_{ma,e,c}(j\omega) - B(j\omega)H_{ma,e,c}(j\omega)].
\end{aligned} \tag{4.22}$$

The goal is to find out proper $\alpha(j\omega)$ and $\beta(j\omega)$ that lead to mutual cancelation of $B^*(-j\omega)$ in (4.22). This condition is fulfilled when

$$\begin{aligned}
\alpha(j\omega)H_{ma,e}(j\omega)B^*(-j\omega) - \beta(j\omega)H_{ma,e}(j\omega)B^*(-j\omega) &= \\
\alpha(j\omega)H_{ma,e,c}(j\omega)B^*(-j\omega) + \beta(j\omega)H_{ma,e,c}(j\omega)B^*(-j\omega). &
\end{aligned} \tag{4.23}$$

Now by setting $\alpha(j\omega) = 1$ and equating (4.23) leads to the following solution for $P_{comp}(j\omega)$

$$\beta(j\omega) = \frac{H_{ma,e}(j\omega) - H_{ma,e,c}(j\omega)}{H_{ma,e}(j\omega) + H_{ma,e,c}(j\omega)} = e^{-j\omega}, \tag{4.24}$$

which is equivalent to a unit delay placed on the imaginary path. The obtained solution has an intuitive explanation. Since the multiplication by $I_{LO}(n)$ and $Q_{LO}(n)$ can be interpreted as subsequent modulation and sampling operations, where the sampling instants have a relative phase lag of $\pi/4$, $\beta(j\omega)$ acts as a phase correction mechanism to remove the phase difference. Furthermore, by evaluating (4.18) with the corrected $B(j\omega)$ leads to $B_{m,e,eq}(j\omega) = B(j\omega)[\frac{1}{j} \sum_{i=1}^{R_e/2} e^{-2j\omega i}]$. This equals to $B(j\omega)$ weighted by a transfer function with a low-pass characteristic in the baseband.

4.3.2 Additive compensation method

An alternative compensation technique for removal of the conjugate image is formed by injecting a filtered conjugate image of the input sequence to the input of the imbalanced linear system [78]. Thus, the filtered conjugate image becomes a canceling image sequence at the output of the system with quadrature imbalance.

Let $\gamma_e(n)$ denote an unknown linear transfer function with corresponding frequency response $\Gamma_e(j\omega)$ in the case of R_e . Then by substituting $b_u(n)$ by $b_u(n) + \gamma_e(n)b_u^*(n)$ (4.12) becomes

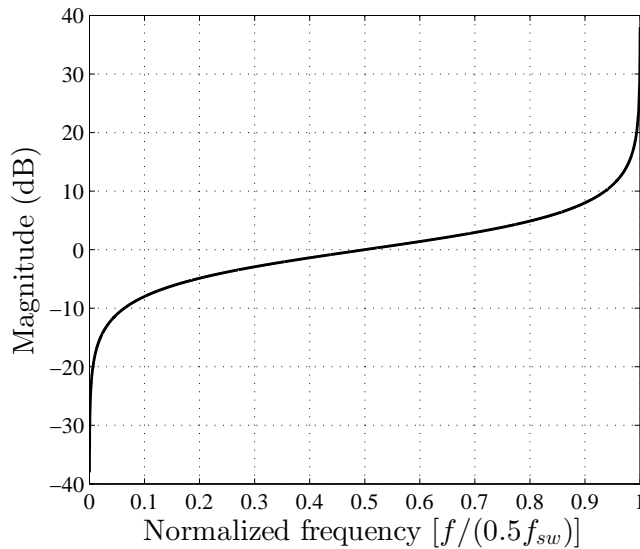
$$\begin{aligned} b_{ac,e}(n) = & \frac{1}{2j} \{ [b_u(n) + \gamma_e(n) * b_u^*(n)] * h_{ma,e}(n) - \\ & [b_u^*(n) + \gamma_e^*(n) * b_u(n)] * h_{ma,e,c}(n) \} \end{aligned} \quad (4.25)$$

with the following frequency response

$$\begin{aligned} B_{ac,e}(j\omega) = & \frac{1}{2j} \{ [B_u(j\omega) + \Gamma_e(j\omega)B_u^*(-j\omega)] H_{ma,e}(j\omega) - \\ & [B_u^*(-j\omega) + \Gamma_e^*(-j\omega)B_u(j\omega)] H_{ma,e,c}(j\omega) \}. \end{aligned} \quad (4.26)$$

Now the desired cancelation condition can be determined by setting the two conjugate images in (4.26) equal and solving for $\Gamma_e(j\omega)$. Hence, a solution can be obtained as

$$\begin{aligned} \Gamma_e(j\omega)B^*(-j\omega)H_{ma,e}(j\omega) &= B^*(-j\omega)H_{ma,e,c}(j\omega) \\ \Gamma_e(j\omega) &= \frac{H_{ma,e,c}(j\omega)}{H_{ma,e}(j\omega)} = \frac{(1-e^{-j\omega})}{(1+e^{-j\omega})}. \end{aligned} \quad (4.27)$$

FIGURE 4.2: Magnitude response of $\Gamma_e(j\omega)$.

The resulting $\Gamma_e(j\omega)$, which is independent of the choice of R_e , is real valued and has properties of a π -phase filter with a constant phase response. This means that the relevant information is given by $|\Gamma_e(j\omega)|^2$, which is illustrated in Figure 4.2. Therefore, a cancellation is achieved when a frequency dependent magnitude weighting is properly applied to the injected conjugate image sequence. Finally by inserting $\Gamma_e(j\omega)$ into (4.26) a compensated baseband model in case of R_e reads

$$B_{m,e,eq}(j\omega) = \frac{1}{2j} [B(j\omega)H_{ma,e}(j\omega) - \Gamma_e^*(-j\omega)H_{ma,e,c}(j\omega)B(j\omega)]. \quad (4.28)$$

From (4.28) it can be seen that the injected conjugate image yields a copy of the original input sequence to $B_{m,e,eq}(j\omega)$. Since the two sequences are matched in phase, the additive conjugate quantization noise compensation leads to an amplification of the quantization noise. However, the amplification factor is for realistic modulator settings very small due to attenuation delivered by $\Gamma_e^*(-j\omega)H_{ma,e,c}(j\omega)$ and thus the difference in quantization noise power described by un-compensated model (4.18) and compensated model (4.28) can be regarded negligible.

Following the lines of the derivation presented above an analogous compensation scheme can be found for R_o settings. Again, $\gamma_o(n)$ represents the weighting function for the injected conjugate image with frequency response $\Gamma_o(j\omega)$.

In order to ensure correct frequency alignment for the canceling image, the injected conjugate sequence has to be shifted by $\pi/2$. Thus by substituting $b_u(n)$ by $b_u(n) + \gamma_o(n) * e^{j\pi n/R_o} b_u^*(n)$ (4.14) becomes

$$b_{ac,o}(n) = \frac{1}{2j} \{ [b_u(n) + \gamma_o(n) * e^{j\pi n/R_o} b_u^*(n)] * h_{ma,o}(n) - [b_u^*(n) + \gamma_o^*(n) * e^{j\pi n/R_o} b_u(n)] e^{j\pi n/R_o} * h_{ma,e,c}(n) \} \quad (4.29)$$

with frequency response equal to

$$B_{ac,o}(j\omega) = \frac{1}{2j} \{ [B_u(j\omega) + \Gamma_o(j\omega) B_u^*(-j(\omega + \pi/R_o))] H_{ma,o}(j\omega) - [B_u^*(-j(\omega + \pi/R_o)) + \Gamma_o^*(-j\omega) B_u(j\omega)] H_{ma,e,c}(j\omega) \}. \quad (4.30)$$

Thus, the conjugate terms from (4.30) disappear when

$$\begin{aligned} \Gamma_o(j\omega) B_u^*(-j(\omega + \pi/R_o)) H_{ma,o}(j\omega) &= B_u^*(-j(\omega + \pi/R_o)) H_{ma,o,c}(j\omega) \\ \Gamma_o(j\omega) &= \frac{H_{ma,o,c}(j\omega)}{H_{ma,o}(j\omega)}. \end{aligned} \quad (4.31)$$

A closed form solution for $\Gamma_o(j\omega)$ can be found by inserting (4.16) and (4.9) into (4.31), which gives

$$\Gamma_o(j\omega) = \frac{(1 - e^{-j\omega} + e^{-j\omega R_o} - e^{-j\omega R_o + 1})}{(1 - e^{-j\omega R_o})(1 + e^{-j\omega})}. \quad (4.32)$$

This solution is again a real valued transfer function with constant zero phase characteristics on the complex baseband. Therefore, similar to the case of R_e the cancelation for R_o settings is obtained by manipulating only the magnitude of the additive conjugate term according to (4.32).

In Figure 4.3 a) an exemplary $|\Gamma_o(j\omega)|^2$ is shown for $R_o = 5$. Further illustrations of the baseband part of $|\Gamma_o(j\omega)|^2$ for various R_o settings are given in Figure 4.3 b). Ultimately, the compensated baseband model for R_o settings in frequency domain reads

$$B_{m,o,eq}(j\omega) = \frac{1}{2j} [B(j\omega) H_{ma,o}(j\omega) - \Gamma_o^*(-j\omega) H_{ma,o,c}(j\omega) B(j\omega)]. \quad (4.33)$$

The same argumentation regarding quantization noise amplification due to an

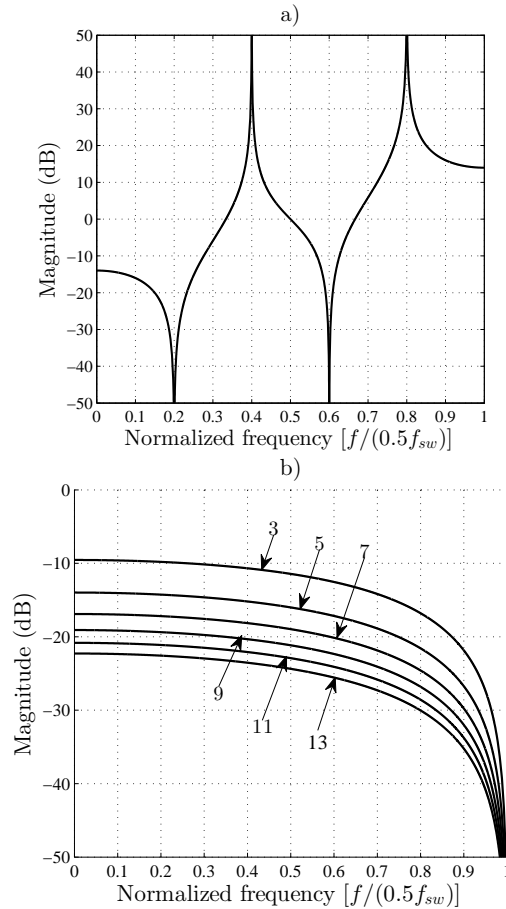


FIGURE 4.3: Magnitude responses of $\Gamma_o(j\omega)$ for a) $R_o = 5$ and for b) various R_o settings.

additional copy of $B(j\omega)$ as presented for the case of R_e applies for R_o settings as well, and thus $|B_{m,o,eq}(j\omega)|^2 \simeq |B(j\omega)|^2$.

4.3.3 Magnitude equalization based compensation

Next to the presented delay based and additive pre-compensation methods, the conjugate quantization noise folding can be alternatively encountered by manipulating the magnitude of quantization noise.

As presented in section 3.2.2 the noise shaping in the complex baseband can be performed around f_{IF} . Therefore, the harmful conjugate quantization noise proportion in complex baseband locates at $-f_{IF}$ and $-f_{IF} + \pi^2$ in case of R_e and R_o ,

² f_{IF} is normalized between $[-\pi, \pi]$

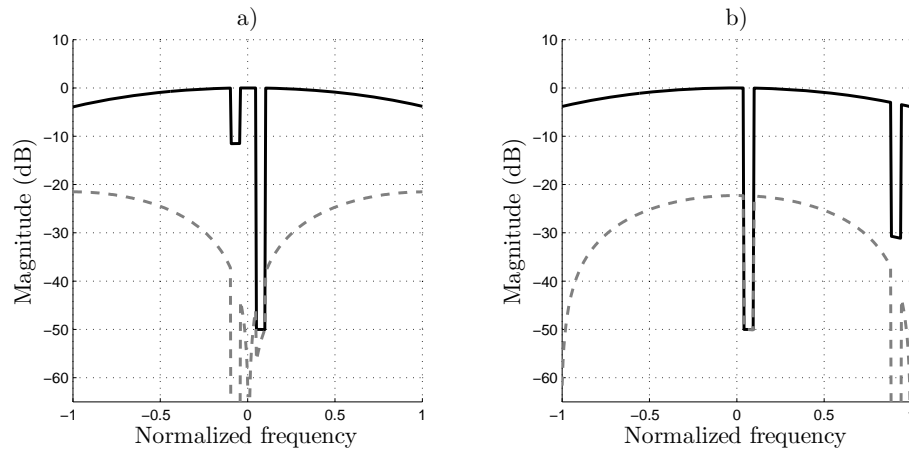


FIGURE 4.4: Conjugate quantization noise folding compensation by additional noise shaping for a) R_e settings b) R_o settings.

respectively. On the one hand, if an additional noise shaping is performed at these settings, the overlapping conjugate quantization noise can be suppressed below the quantization noise floor defined by the noise shaping performed at the signal band. This method is illustrated in frequency domain for ideal NTFs for R_e and R_o settings in Figure 4.4 a) and b).

4.4 Noise shaped encoders employing conjugate quantization noise compensation

The closed-form descriptions of the conjugate quantization noise folding in complex baseband enabled derivation of compensating systems which effectively lead to a complete suppression of the conjugate image. However, the pre-compensating systems were derived given that the sampling frequency is equal to f_{sw} . In order to decrease computational complexity the noise shaped encoding is performed at the lowest possible f_s , for which sufficient SNDR is obtained. This in turn means that $R_s > 1$ for a realistic scenario given the state-of-the-art reconfigurable hardware and the transmission settings of modern wireless communication networks. Therefore, the given compensation models employed in noise shaped encoders need to operate at f_s as well. Further due to specific NTF design constraints the compensation conditions have to be approximated which results in only a partial

suppression of the conjugate noise. On the other hand, the fact that the relevant part of the harmful conjugate noise locates at signal band can be utilized to optimize the compensation performance.

4.4.1 Linearized models describing conjugate quantization noise folding

The linearized modeling of the noise shaped encoders presented in Section 2.1 can be further utilized to study a system consisting of the modulator and the complex bandpass model of the digital up-conversion. Hence, the compensated modulator in the general case can be expressed by a description of a quadrature imbalanced linear system in which the LTI systems operating on the non-conjugated and the conjugated noise sequences are denoted by NTF and image NTF (INTF), respectively. By considering only the baseband proportions of (4.18) and (4.20) the following equivalent baseband descriptions are obtained

$$B_{eq,e}(j\omega) = \frac{1}{2j} [B(j\omega)H_{ma,e}(j\omega/R_e) - B^*(-j\omega)H_{ma,e,c}(j\omega/R_e)]. \quad (4.34)$$

and

$$B_{eq,o}(j\omega) = \frac{1}{2j} [B(j\omega)H_{ma,o}(j\omega/R_o) - B^*(j(\omega + \pi))H_{ma,o,c}(j\omega/R_o)]. \quad (4.35)$$

The combined linearized model can be thus obtained by cascading the two imbalanced systems and by computing the input-output relations for the original and the conjugated copy of the excitation noise $E(j\omega)$. In frequency domain these relations in case of R_e and R_o become

$$\begin{aligned} Y_e(j\omega) &= \text{NTF}_{\text{tot},e}(j\omega)E(j\omega) \\ &\quad + \text{INTF}_{\text{tot},e}(j\omega)E^*(-j\omega), \end{aligned} \quad (4.36)$$

$$\begin{aligned} \text{NTF}_{\text{tot},e}(j\omega) &= [\text{NTF}_e(j\omega)H_{ma,e}(j\omega/R_e) \\ &\quad + \text{INTF}_e^*(-j\omega)H_{mac,e}(j\omega/R_e)] \end{aligned} \quad (4.37)$$

$$\begin{aligned} \text{INTF}_{\text{tot,e}}(j\omega) &= [\text{INTF}_e(j\omega)\text{H}_{\text{ma,e}}(j\omega/R_e) \\ &\quad + \text{NTF}_e^*(-j\omega)\text{H}_{\text{mac,e}}(j\omega/R_e)] \end{aligned} \quad (4.38)$$

and

$$\begin{aligned} Y_o(j\omega) &= \text{NTF}_{\text{tot,o}}(j\omega)\text{E}(j\omega) \\ &\quad + \text{INTF}_{\text{tot,o}}(j\omega)\text{E}^*(j\omega), \end{aligned} \quad (4.39)$$

$$\begin{aligned} \text{NTF}_{\text{tot,o}}(j\omega) &= [\text{NTF}_o(j\omega)\text{H}_{\text{ma,o}}(j\omega/R_o) \\ &\quad + \text{INTF}_o^*(j\omega)\text{H}_{\text{mac,o}}(j\omega/R_o)] \end{aligned} \quad (4.40)$$

$$\begin{aligned} \text{INTF}_{\text{tot,o}}(j\omega) &= [\text{INTF}_o(j\omega)\text{H}_{\text{ma,o}}(j\omega/R_o) \\ &\quad + \text{NTF}_o^*(j\omega)\text{H}_{\text{mac,o}}(j\omega/R_o)], \end{aligned} \quad (4.41)$$

where $\text{NTF}_{\text{tot,e}}(j\omega)$, $\text{INTF}_{\text{tot,e}}(j\omega)$, $\text{NTF}_{\text{tot,o}}(j\omega)$ and $\text{INTF}_{\text{tot,o}}(j\omega)$ denote the total NTF for R_e , the total INTF for R_e , the total NTF for R_o and the total INTF for R_o , respectively. These models are illustrated in cascaded form in Figure 4.5 a) and b).

From the compensation point of view, the relevant information is delivered by $\text{INTF}_{\text{tot,e}}(j\omega)$ and $\text{INTF}_{\text{tot,o}}(j\omega)$ around the signal band. More precisely a knowledge of whether the average power of conjugate quantization noise exceeds the average power of the original noise shaped quantization noise is of interest. For this purpose a performance metric commonly applied for imbalanced quadrature $\Sigma\Delta$ data converters called image rejection ratio (IRR) can be utilized [29]. By assuming that the variance of the quantization noise is equal to one, the equations for IRR in the case of R_e and R_o read

$$\text{IRR}_e = \frac{\int_{\omega_1}^{\omega_2} |\text{NTF}_{\text{tot,e}}(j\omega)|^2}{\int_{\omega_1}^{\omega_2} |\text{INTF}_{\text{tot,e}}(j\omega)|^2} \quad (4.42)$$

and

$$\text{IRR}_o = \frac{\int_{\omega_1}^{\omega_2} |\text{NTF}_{\text{tot,o}}(j\omega)|^2}{\int_{\omega_1}^{\omega_2} |\text{INTF}_{\text{tot,o}}(j\omega)|^2}, \quad (4.43)$$

where ω_1 and ω_2 denote the edges of the signal band.

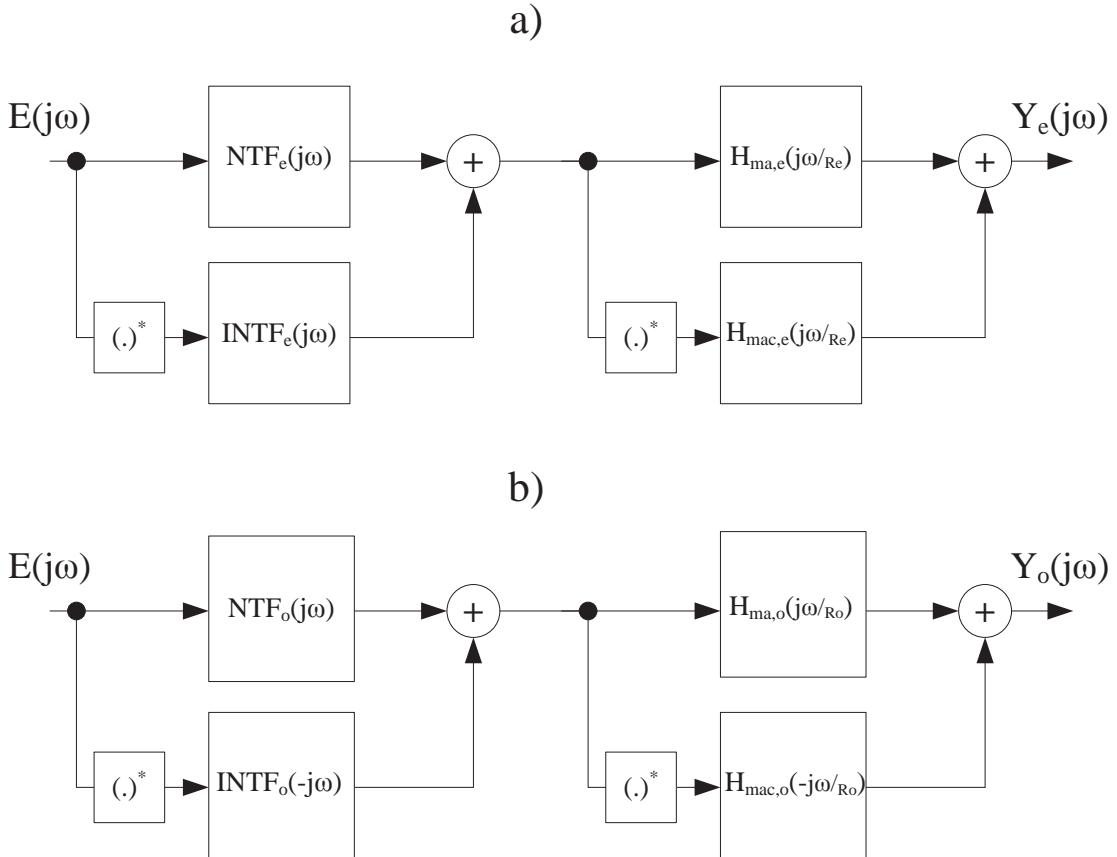


FIGURE 4.5: Equivalent baseband descriptions for a combination of the linearized modulator model and the complex baseband model of the digital up-conversion in case of a) R_e and b) R_o settings.

4.4.2 Noise shaped encoders with additive compensation

The second technique for a complete mitigation of conjugate quantization noise introduced in section 4.3.2 based on additive canceling the conjugate term involves a convolution by a constant phase filter (4.32). Since such filters have anticausal impulse responses, they are usually utilized in off-line applications, where the complete data set to be processed is available [79]. A second option for realizing a constant phase filter is to delay the impulse response by a constant value, which gives a linear phase filter [80]. This solution, however, implies a phase lag in form of a constant group delay which is undesirable for RF transceiver usage. In pulsed RF signal generation purposes the modulator is operating on-line and the input data symbols are in general unknown. Furthermore, NTFs and INTFs of compensated noise shapers have to fulfill the realization criteria. For these

reasons an alternative strategy is proposed for inclusion of the additive conjugate quantization noise cancellation to a quadrature noise shaped encoder.

A filtering operation by a zero-phase filter can be interpreted as a frequency dependent magnitude component adjustment. Hence the simplest zero-phase filter is a multiplication by a constant. This allows for convenient and straightforward approximations to (4.27) and (4.32). By evaluating the given constant phase filters at f_{IF} the approximations become $\hat{\Gamma}_e = \Gamma_e(jf_{IF})$ and $\hat{\Gamma}_o = \Gamma_o(jf_{IF})$. Therefore, the optimal cancelation performance is obtained only at a single frequency setting, namely at the center of the signal band. However, due to over-sampling it can be assumed that the approximation error along the signal band does not increase notably.

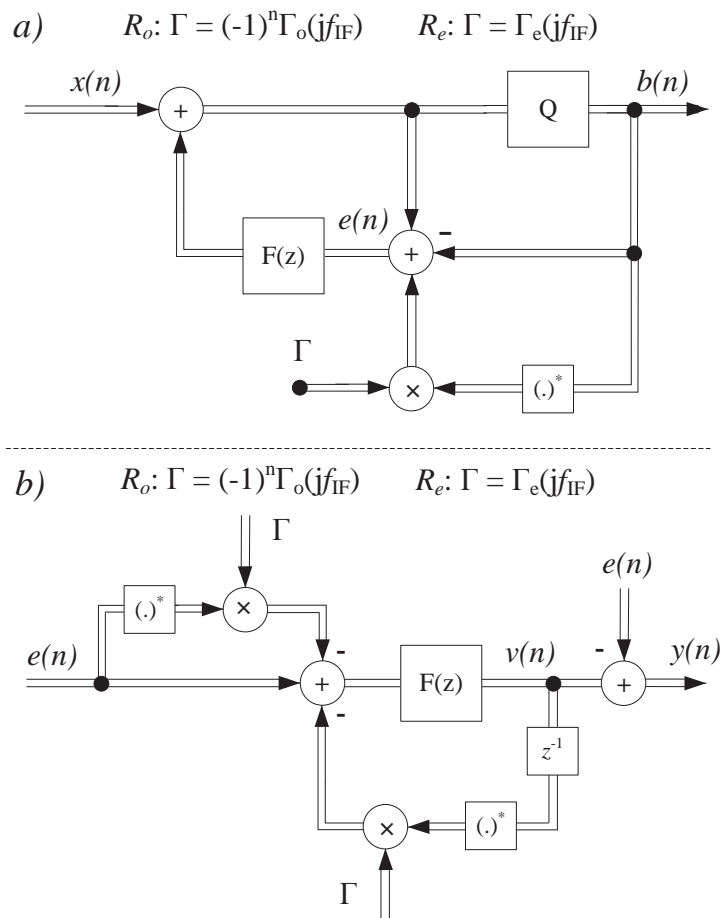


FIGURE 4.6: Modified error feedback noise shaper structure employing additive conjugate quantization noise cancelation

In order to incorporate the additive conjugate quantization noise compensation by constant multiplication approximations into a noise shaper structure, a modified error-feedback topology is proposed. The novel architecture is given in Figure 4.6 a). The simple modification by an addition of a weighted conjugate image of the encoded output sequence leads on the one hand to a new relation between $F(z)$ and NTF and on the other hand makes the compensation performance dependent on $F(z)$. To see how these arguments apply it is convenient to study the linearized form of the modified error feedback structure, which is given in Figure 4.6 b). The NTF/INTF pair as a function of $F(z)$ can be found³ by applying z -transformation to the linearized structure. The relations become

$$\begin{aligned}
\text{NTF}_e(z) &= 1 - \frac{z^{-1}[F(z) + |\Gamma_e(jf_{\text{IF}})|^2 F^*(-z)F(z)]}{1 - z^{-2}|\Gamma_e(jf_{\text{IF}})|^2 F^*(-z)F(z)} \\
\text{INTF}_e(z) &= \frac{z^{-1}\Gamma_e(jf_{\text{IF}})[F(z) + F^*(-z)F(z)]}{1 - z^{-2}|\Gamma_e(jf_{\text{IF}})|^2 F^*(-z)F(z)} \\
\text{NTF}_o(z) &= 1 - \frac{z^{-1}[F(z) + |\Gamma_o(jf_{\text{IF}})|^2 F^*(z)F(z)]}{1 - z^{-2}|\Gamma_o(jf_{\text{IF}})|^2 F^*(z)F(z)} \\
\text{INTF}_o(z) &= \frac{z^{-1}\Gamma_o(jf_{\text{IF}})[F(z) + F^*(z)F(z)]}{1 - z^{-2}|\Gamma_o(jf_{\text{IF}})|^2 F^*(z)F(z)},
\end{aligned} \tag{4.44}$$

where $\text{NTF}_e(z)$, $\text{INTF}_e(z)$, $\text{NTF}_o(z)$ and $\text{INTF}_o(z)$ denote the NTF for R_e , the INTF for R_e , the NTF for R_o and the INTF for R_o , respectively. However, from these relations the functionality of the modified error feedback structure is still difficult to interpret. For clarification let $F(z) = F_b(z)/F_a(z)$. After substitution and a few algebraic manipulations it can be shown that $\text{NTF}_e(z)$ and $\text{INTF}_e(z)$ become

$$\begin{aligned}
\text{NTF}_e(z) &= \frac{F_a(z)F_a^*(-z) - 2|\Gamma_e|^2 F_b(z)F_b^*(-z) - F_b(z)F_a^*(-z)}{F_a(z)F_a^*(-z) - |\Gamma_e|^2 F_b(z)F_b^*(-z)} \\
\text{INTF}_e(z) &= \frac{\Gamma_e F_b(z)F_a^*(-z) - \Gamma_e F_b(z)F_b^*(-z)}{F_a(z)F_a^*(-z) - |\Gamma_e|^2 F_b(z)F_b^*(-z)}.
\end{aligned} \tag{4.45}$$

Next, by stating that $|\Gamma_e|^2 F_b(z) \approx 0$ the above simplifies into

$$\begin{aligned}
\text{NTF}_e(z) &\approx \frac{F_a(z) - F_b(z)}{F_a(z)} \\
\text{INTF}_e(z) &\approx \frac{F_b(z)\Gamma_e[F_a^*(-z) - F_b^*(-z)]}{F_a(z)F_a^*(-z)} \approx F(z)\Gamma_e \text{NTF}^*(-z)
\end{aligned} \tag{4.46}$$

Thus, without the residual terms $\text{NTF}_e(z)$ reduces to the original error-feedback loop coefficients given in section 3.2.1. Secondly $\text{INTF}_e(z)$ can be interpreted as a

³See Appendix A for derivation.

weighted conjugate version of $\text{NTF}_e(z)$ with additional convolution by $F(z)$. This means that the compensation becomes dependent on characteristics of $F(z)$ in the signal band. The error feedback loop filters related to the conventional prototype NTFs discussed in Section 3.2.2 exhibit approximately unit magnitude and zero phase characteristics near the signal band. Therefore, the influence of $F(z)$ can be considered negligible for those NTFs especially in the case when the OSR is chosen high enough. It can be summarized that the modified error-feedback structure delivers a rough approximation of the additive conjugate quantization noise compensation that is preferable for narrow signal-band settings.

4.4.3 Noise shaped encoders with delay based compensation

For R_e settings an intuitive and simple compensation scheme consisting of a single unit delay element was obtained in Section 4.3.1. However, since $R_e \geq 2$ the corresponding delay in complex baseband is a rational number equal to $1/R_e$. A common digital signal processing tool for realization of such non-integer delays is called fractional delay (FD) filter [81]. Firstly, from a noise shaping point of view it would be desirable to modify only the phase characteristics of the quantization noise. Conversely a FD filter, which modifies also the magnitude response, may lead to unnecessary noise shaping and, thus, more likely to increased instability. Secondly, it can be argued that the absolute phase information of the real and the imaginary components of the quantization noise is not critical as long as the magnitude of the quantization noise is minimized around the signal band. Therefore, an all-pass filter that implements a rational delay difference between the real and the imaginary components of the complex valued sequence is a sufficient solution.

The phase characteristics of the noise shaped quantization noise contained in a complex valued encoded sequence is defined by NTF. Thus, an equalized NTF with delay based compensation can be composed of a complex valued all-pass

filter $C(z)$ and a prototype NTF(z) as follows

$$\text{NTF}_d(z) = C(z)\text{NTF}(z). \quad (4.47)$$

It is important to notice that the NTF realization criteria apply also to $\text{NTF}_d(z)$. This can be guaranteed when the first coefficient of $C(z)$ is equal to one. The strength of the given method is that $\text{NTF}_d(z)$ can be readily used in an existing noise shaper topology. For instance, the loop filter coefficients for the error feedback structure can be obtained straightforwardly $\text{NTF}_d(z) = 1 - z^{-1}F(z)$.

The remaining task is to find coefficients for $C(z)$ such that the design constraints given above are fulfilled to some extent. Since $C(z)$ is actually a quadrature imbalanced linear system, it turns out that the estimation task can be treated as an equalization problem, where $C(z)$ is cascaded with a counter imbalanced system. Ideally, the complex valued output of the cascade becomes a fractionally delayed version of the complex valued input. Due to multiple design constraints, i.e. the NTF realization criteria and the all-pass criteria, the design task can be relaxed by concerning only the relative group delay difference around the signal band.

Let $D(z) = z^{-1/R_e} + j$ denote a reference system, which consists of an ideal FD element placed on the real path. The output of the cascaded system can be thus expressed by using the average and the difference transfer functions as follows

$$\begin{aligned} C_{\text{avg,t}}(z) &= C_{\text{avg}}(z)D_{\text{avg}}(z) + C_{\text{diff}}^*(z)D_{\text{diff}}(z), \\ C_{\text{diff,t}}(z) &= C_{\text{diff}}(z)D_{\text{avg}}(z) + C_{\text{avg}}^*(z)D_{\text{diff}}(z). \end{aligned} \quad (4.48)$$

On the other hand, given that $C(z) = R_1(z) - Q_1(z) + j(R_2(z) + Q_2(z))$ the above expressions with real valued transfer functions for real and imaginary paths

become

$$\begin{aligned}
C_{\text{avg,t}}(z) &= \\
&\frac{1}{2}(z^{-1/R_e} + 1)\frac{1}{2}[R_1(z) + R_2(z) + j(Q_1(z) + Q_2(z))] + \\
&\frac{1}{2}(z^{-1/R_e} - 1)\frac{1}{2}[R_1(z) - R_2(z) - j(Q_1(z) - Q_2(z))] \quad (4.49) \\
&= \\
&\frac{1}{2}z^{-1/R_e}[R_1(z) + jQ_2(z)] + \frac{1}{2}[R_2(z) + jQ_1(z)].
\end{aligned}$$

$$\begin{aligned}
C_{\text{diff,t}}(z) &= \\
&\frac{1}{2}(z^{-1/R_e} + 1)\frac{1}{2}[R_1(z) - R_2(z) + j(Q_1(z) - Q_2(z))] + \\
&\frac{1}{2}(z^{-1/R_e} - 1)\frac{1}{2}[R_1(z) + R_2(z) - j(Q_1(z) + Q_2(z))] \quad (4.50) \\
&= \\
&\frac{1}{2}z^{-1/R_e}[R_1(z) - jQ_2(z)] + \frac{1}{2}[-R_2(z) + jQ_1(z)].
\end{aligned}$$

With expressions (4.49) and (4.50) the optimization goals can be interpreted straightforwardly. Firstly, $|C_{\text{avg,t}}(z)|^2$ shall be minimized around the signal band. Secondly, the complete magnitude response of $C(z)$, namely $|C_{\text{avg}}(z)|^2 + |C_{\text{diff}}(z)|^2$ shall remain close to unit magnitude. This description casts the original all-pass filter design problem into a constrained optimization problem. Such techniques for filter design purposes have been earlier utilized for quadrature mirror filter banks [82], where the constrained optimization problem is re-formulated into an unconstrained form. In order to apply such transformation to estimate FIR type complex all-pass filters with the above given criteria in unconstrained fashion let

$$\boldsymbol{\gamma}(j\omega) = [1 \ e^{-j\omega} \ \dots \ e^{-j\omega L}]^T \quad (4.51)$$

$$\boldsymbol{\gamma}_{\text{fd}}(j\omega) = [1 \ e^{-j\omega-1/R_e} \ \dots \ e^{-j\omega L-1/R_e}]^T \quad (4.52)$$

$$\mathbf{a} = [1 \ R_{1,2} + jQ_{2,2} \ \dots \ R_{1,L} + jQ_{2,L}]^T \quad (4.53)$$

$$\mathbf{b} = [1 \ R_{2,2} + jQ_{1,2} \ \dots \ R_{2,L} + jQ_{1,L}]^T, \quad (4.54)$$

where L denotes the order of the FIR filter, $R_{1,n}$, $R_{2,n}$ and $Q_{1,n}$, $Q_{2,n}$ the n th coefficient of the filters $R_1(z)$, $R_2(z)$ and $Q_1(z)$, $Q_2(z)$, respectively. Thus, $C_{\text{diff,t}}(z)$,

$C_{\text{avg}}(z)$ and $C_{\text{diff}}(z)$ become

$$C_{\text{diff},t}(j\omega) = \frac{1}{2}\mathbf{a}^H\boldsymbol{\gamma}_{\text{fd}}(j\omega) - \frac{1}{2}\mathbf{b}^H\boldsymbol{\gamma}(j\omega) \quad (4.55)$$

$$C_{\text{avg}}(j\omega) = \frac{1}{2}\mathbf{a}^T\boldsymbol{\gamma}(j\omega) + \frac{1}{2}\mathbf{b}^T\boldsymbol{\gamma}(j\omega) \quad (4.56)$$

$$C_{\text{diff}}(j\omega) = \frac{1}{2}\mathbf{a}^H\boldsymbol{\gamma}(j\omega) - \frac{1}{2}\mathbf{b}^H\boldsymbol{\gamma}(j\omega). \quad (4.57)$$

At next, the total cost function J_{TOT} can be expressed with the above expressions as follows

$$J_1 = \sum_{\omega=\omega_1}^{\omega_2} |C_{\text{diff},t}(j\omega)|^2 \quad (4.58)$$

$$J_2 = \sum_{\omega=0}^{2\pi} ||C_{\text{diff}}(j\omega)|^2 + |C_{\text{avg}}(j\omega)|^2 - 1|^2 \quad (4.59)$$

$$J_{\text{TOT}} = J_1 + \alpha J_2, \quad (4.60)$$

where J_1 describes the magnitude of the conjugate image along the signal band between $[\omega_1\omega_2]$, J_2 the deviation from the ideal all-pass response and α a weighting for the all-pass error.

Finally the coefficients \mathbf{a} and \mathbf{b} can be calculated iteratively by following the steps given below

- 1) Initialize \mathbf{a} and \mathbf{b} with random complex exponentials locating inside unit. Additionally set α so that $\alpha < 1$.
- 2) Perform optimization for J_{TOT} .
- 3) Evaluate the obtained values of J_1 and J_2 . On the one hand, if the resulting J_1 is unsatisfactory, increase α and return to 2). On the other hand, if the resulting J_2 becomes prohibitively large, decrease α and return to 2). If both J_1 and J_2 cannot mutually fulfil the a priori defined error bounds, then it can be expected that the optimization goals are too tight for the given parameter settings. In this case, a larger L may be considered for possibly improved conjugate image suppression. Otherwise the optimization procedure has produced suitable coefficients.

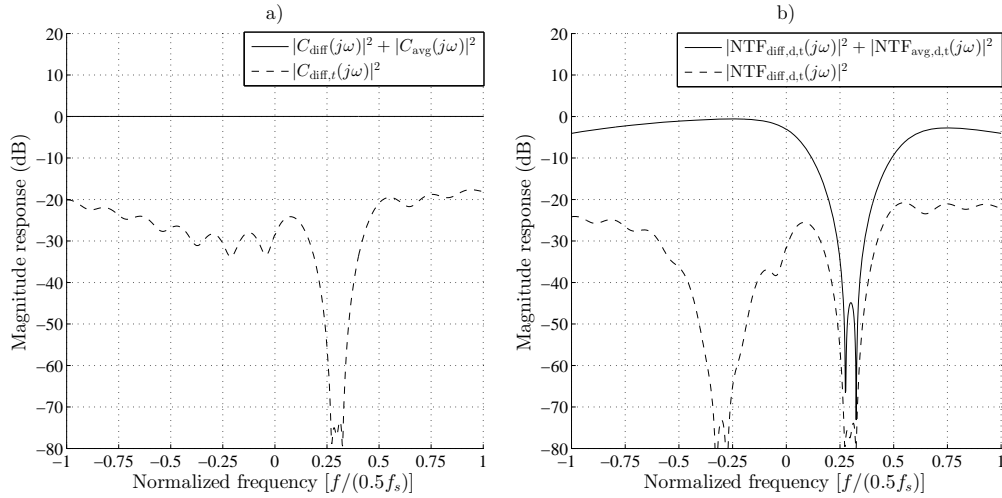


FIGURE 4.7: Magnitude responses of a) complex all-pass filter $C(z)$ and corresponding equalized conjugate image transfer function and b) NTF and INTF with delay based compensation.

Figure 4.7 a) presents magnitude responses of an exemplary complex-allpass filter obtained with the above optimization routine implemented with the Matlab optimization toolbox function *fminunc* for $R_e = 14, L = 12, \omega_1 = 0.295$ and $\omega_2 = 0.305$. By combining the complex all-pass filter with a prototype NTF with $f_{\text{IF}} = 0.3$, the complete conjugate quantization noise on the signal band is suppressed well below the average quantization noise power as illustrated in Figure 4.7 b).

4.4.4 Noise shaped encoders with magnitude response equalization based compensation

In contrast to the delay based and to the additive compensation methods, the conjugate quantization noise compensation technique relying on additional noise shaping does not require any structural modifications to the noise shaper part of the modulator. Furthermore, as long as the modulator operation remains stable, the average conjugate quantization noise power can be suppressed well below the average quantization noise power in the signal band. Hence, by optimizing the magnitude response of the NTF properly, the desired signal band noise shaping performance for the RF pulse sequences can be restored for arbitrary f_{IF} and R_s settings.

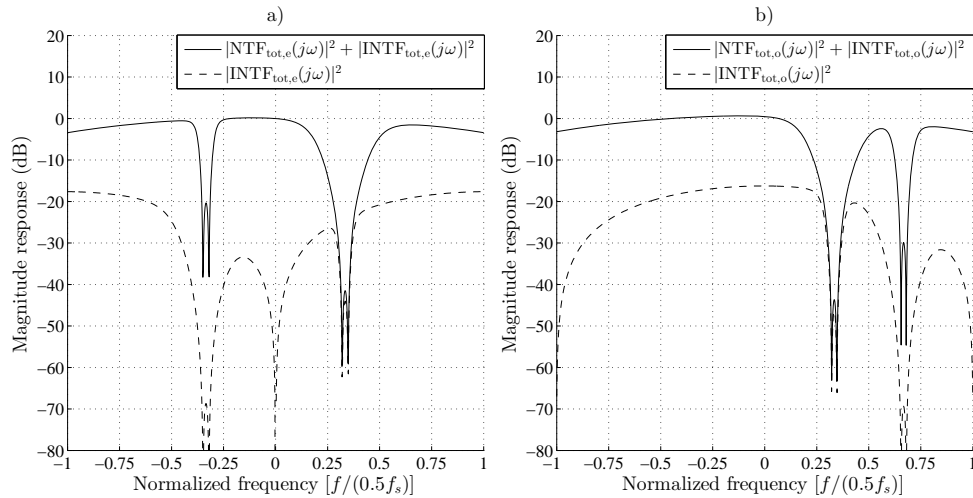


FIGURE 4.8: Exemplary magnitude responses of NTF and INTF with magnitude response equalization based compensation in case of a) $R_e = 8$ and b) $R_o = 7$.

Obviously it is desirable to find out the minimum amount of quantization noise suppression on the image band which results in a condition where the conjugate quantization noise power on the signal band can be considered negligible. This is important because the additional noise shaping leads to an increase in the NTF order and as shown in Section 3.3.3, the Q $\Sigma\Delta$ PWM modulators employing higher order NTFs are more prone to modulator instability. Given the linearized models (4.36) and (4.39) and a prototype NTF, the corresponding IRR values can be evaluated for uncompensated modulators by evaluating (4.42) and (4.43). These measures define the relative average noise power difference between the signal band quantization noise and the signal band conjugate quantization noise. Hence, by introducing a scaled copy of the prototype NTF $\text{NTF}_{im}(z)$ with quantization noise suppression equal to $\text{IRR} + \delta$, ($\delta > 0$) at $-f_{\text{IF}}$ or $-f_{\text{IF}} + \pi$ for R_e and R_o settings respectively, the desired conjugate quantization noise suppression can be obtained. The small positive valued constant δ ensures that the average power of the suppressed conjugate quantization noise in the signal band is strictly lower than the average quantization noise power. Finally, the NTF with compensation can be obtained by convolving the prototype NTF with $\text{NTF}_{im}(z)$. Exemplary magnitude responses illustrating the compensation performance of the given method in frequency domain are given in Figure 4.8 a) for $R_e = 8$ and in Figure 4.8 b)

for $R_o = 7$. Albeit non-optimal, the given technique allows for straightforward implementations with the existing NTF design tools [68].

4.5 Conjugate signal compensation

Next to the conjugate quantization noise component an image of the over-sampled complex baseband signal becomes an interferer for distinct f_θ and R_s settings during digital up-conversion. In principle, the same compensation techniques derived for the conjugate noise in Section 4.4 are directly applicable for the suppression of the conjugate image component. Contrary to the conjugate quantization noise rejection techniques, which require realizations compatible with the noise shaped encoder topologies, the conjugate signal component compensation can be implemented without such constraints. The previous work on the topic includes approximations of (4.27) by a FIR filter and approximations of the FD $1/R_e$ by an estimated FIR type FD filter [80]. In context of digital up-conversion of pulsed baseband sequences containing a single transmission signal the compensation is necessary on a relatively narrow bandwidth. Therefore, the wideband compensation performance obtained by the FIR approximations is largely unnecessary. On the other hand, the methods for implementing the additive compensation techniques given in Section 4.4.2. are an effective way to perform the conjugate signal compensation for both R_e and R_o settings. Given the multiplicative approximations $\hat{\Gamma}_e = \Gamma_e(jf_\theta)$ and $\hat{\Gamma}_o = \Gamma_o(jf_\theta)$ the compensated $x_u(n)$ becomes

$$x_{ac,e}(n) = x_u(n) + \hat{\Gamma}_e x_u(n)^*, \quad (4.61)$$

for R_e settings and

$$x_{ac,o}(n) = x_u(n) + (-1)^n \hat{\Gamma}_o x_u(n)^*, \quad (4.62)$$

for R_o settings. This way the compensation is optimized always at f_θ and, moreover, no additional phase lag is involved contrary to the FIR filter based compensation.

4.6 Simulation results

In order to verify the conjugate quantization noise compensation properties of the various enhanced digital up-conversion techniques it is essential to study the in-band distortion characteristics of a pulsed RF sequence, produced by a modulator employing the noise shaper topology given in Section 3.2.1. The primary motivation for the evaluations is to reveal f_c settings for which the signal band distortion performance can be expected to be close to that of the complex baseband encoder.

For these purposes the noise shaper part of the Q Σ Δ PWM modulator was substituted by the corresponding compensated topologies and sub-sequently, extensive simulations were performed on MATLAB for numerous modulator parameter combinations. Firstly, the intensive computer simulations complement the approximate distortion performance evaluations delivered by the linearized models. Secondly, since all of the considered compensation strategies lead to modified NTFs, the repetitious simulation runs shall reveal possibly unstable modulator behavior.

TABLE 4.1: Simulation parameters

f_{sw}	Δf_{NTF}	R_s	f_{IF}, f_θ	f_{PWM}	$ NTF _\infty$	N
10 GHz	25 MHz	2–14	$(0-0.5)\frac{f_{sw}}{R_s}$	$\frac{f_{sw}}{6R_s}$	1.5	2

Unless otherwise noted, the considered common parameter settings are those listed in Table 4.1. The selected f_{sw} , R_s , f_θ and f_{IF} parameters equal to f_c tuning ranges between approximately 714 – 5000 MHz.

4.6.1 Conventional digital up-conversion

At first, a simulation case without conjugate signal and noise compensation was studied. The IRR and SNDR results for different R_e settings are shown in Figure 4.9. As already predicted by the linearized digital up-conversion baseband model in Section 4.2 the effect of the conjugate quantization noise on the dynamic

range becomes significant for $f_{IF} \gg 0$. The evaluated IRR figures given in Figure 4.9 a) suggest that only a small fraction of the potential f_c tuning range can be expected being conjugate quantization noise free.

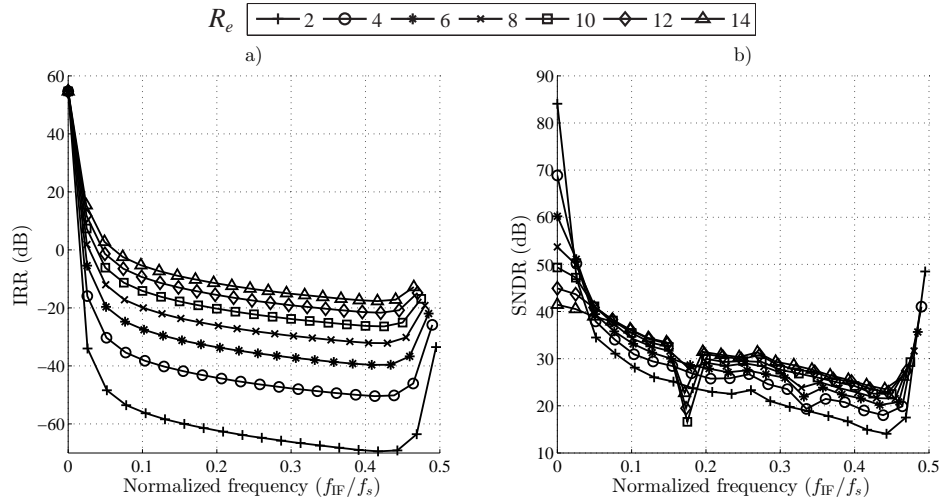


FIGURE 4.9: Evaluation of a) IRR and b) SNDR performance for various R_e settings.

This is confirmed by the SNDR results shown in Figure 4.9 b). By comparing the conjugate quantization noise free settings at $f_{IF} = 0$ to the ones with $f_{IF} > 0$ it can be observed that in the worst case the dynamic range is degraded by over 50 dB. For the higher R_e settings the loss in SNDR becomes milder on the average due to the weighting of $H_{ma,e,c}(j\omega)$, which for the complex baseband proportion decays as R_e grows.

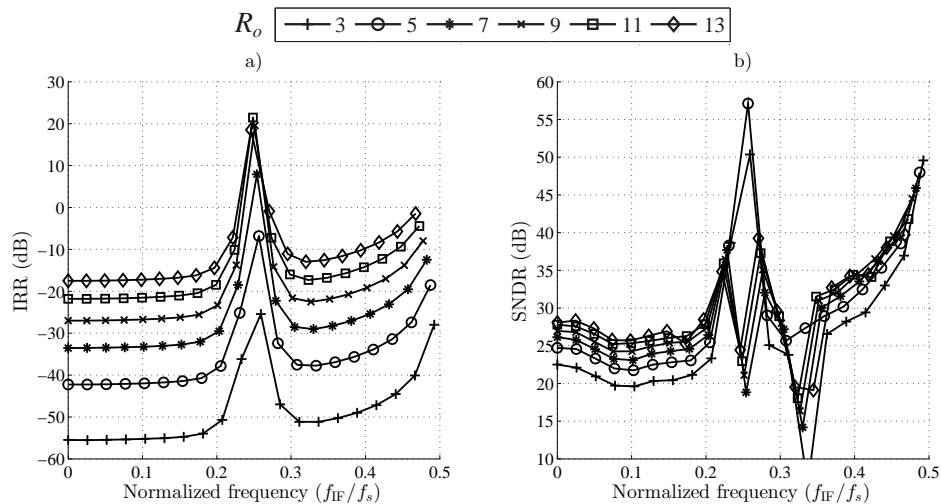


FIGURE 4.10: Evaluation of a) IRR and b) SNDR performance for various R_o settings.

In case of R_o settings the respective IRR and SNDR evaluation results are illustrated in Figure 4.10. By observing the IRR values depicted in Figure 4.10-a) it becomes clear that except for a few parameter combinations, the conjugate quantization noise folding contributes negatively to the signal band dynamic range. Normalized intermediate frequencies f_{IF} for which the uncompensated modulator achieves positive IRR can be found near $f_{IF}/f_s = 0.25$. At this setting the conjugate image of the NTF stop-band overlaps with the original NTF stop-band and thus, the interfering conjugate quantization noise is suppressed. However, as noted in Section 4.1 next to the conjugate signal band quantization noise also the conjugate signal image overlaps with the signal band which degrades the dynamic range further.

The above given analytic predictions are verified by SNDR evaluations shown in Figure 4.10 b). The achieved SNDR is again on the average very far from the ideal complex baseband sequence. Furthermore, the conjugate signal folding corrupts the otherwise conjugate quantization noise free normalized f_{IF} settings for which $f_{IF}/f_s \approx 0.25$.

Based on the above SNDR evaluations it can be argued that without compensation the quantization noise enhancement gained by the noise shaped encoding is lost for most of the f_{IF} settings during the digital up-conversion regardless of the R_s settings. The loss in dynamic range due to conjugate signal and quantization noise is significant and the resulting SNDRs suggest that the resulting adjacent channel leakage ratios (ACLR) for the reconstructed transmission signals become in most cases insufficient in terms of linearity requirements for modern RF base-station usage [56].

4.6.2 Additive compensation

The error feedback noise shaper loop structures implementing the additive compensation techniques were employed in Q $\Sigma\Delta$ PWM modulator to investigate the potential improvements in signal band dynamic range. Secondly, the impact of the

modified loop structures to the properties of the corresponding NTFs is studied as well.

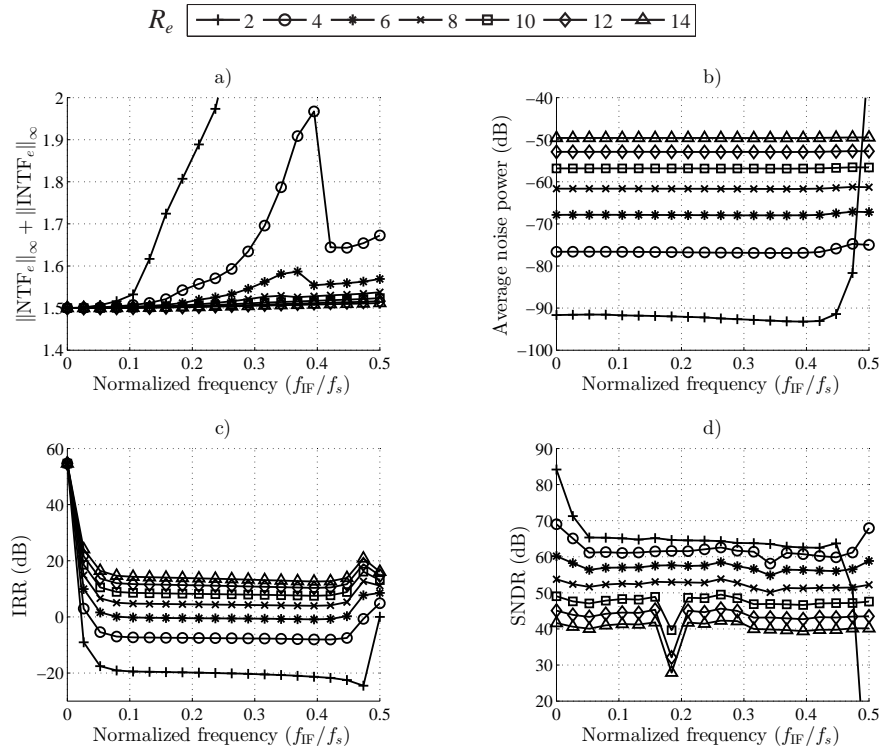


FIGURE 4.11: Evaluation of a) Maximum compensated NTF gain, b) compensated NTF average noise power, c) IRR and d) SNDR for various R_e settings.

As explained in Section 4.4.2 the implementation of the additive compensation technique by the modified error-feedback loop leads also to a modified version of the original NTF. Since the goal of the compensation strategies is to maintain the dynamic range delivered by the original baseband encoding, it is of interest to study the properties of the modified NTFs. In Figure 4.11 a) the maximum gain for the modified NTF is given for the considered modulator parameter settings in case of R_e settings. Clearly between $8 \leq R_e \leq 14$ the modified loop structure has only a minor effect on the maximum NTF gain. For $R_e < 8$ the residual terms in the modified NTF lead to significant changes of the NTF shape and thus to increased maximum NTF gain as well. The rapid increase in the maximum NTF gain for combination of low R_e and high f_{IF} settings may lead to modulator instability especially for modulators with higher order NTFs. On the other hand the average noise powers of the modified NTFs remain well behaved and are close

to those of the original NTFs. The only major difference can be observed for $R_e = 2$ where f_{IF} approaches the Nyquist frequency. In that case the effect of the residual terms becomes dominant since $\Gamma_e \approx 1$ and the shape of the modified NTF deviates significantly from the original NTF.

The IRRs related to the NTF of the loop structure with additive compensation are given in Figure 4.11 c). Obviously, when $R_e \geq 8$ the strictly positive IRRs in dB scale for every simulation setting suggest that the complex baseband dynamic range is restored for the available f_c tuning range. The SNDR results illustrated in Figure 4.11 d) confirm the predicted compensation performance. Except for a few f_{IF} settings, where the signal band dynamic is negatively affected by the PWM harmonics, the presented SNDR values are close to those obtained for the baseband signal. The inadequate conjugate quantization noise compensation for $R_e < 8$ can be explained by the approximations in the implementation of the additive compensation technique. The loss in dynamic range for these settings lies between 2 – 20 dB. Nevertheless, a notable improvement in comparison to the uncompensated modulator settings is achieved.

In case of R_o settings the impact of the compensated loop filter on the maximum NTF gain as shown in Figure 4.12 a) becomes significant for $R_o \leq 5$. Clearly, the gain increases for decreasing f_{IF} . This is because the maximum value of Γ_o is obtained at $f_{\text{IF}} = 0$ and thus the harmful effects of the residual terms become more notable for small f_{IF} and R_o . However, according to the average noise power results shown in Figure 4.12 b) the noise shaping properties of the modified NTF at the signal band can be regarded similar to that of the original NTF.

As illustrated in Figure 4.12 c) IRR values suggesting sufficient compensation for conjugate quantization noise free performance can be regarded for $R_o \geq 9$. By comparing the SNDR results given in Figure 4.12 d) with the ones without compensation given in Figure 4.10, it can be recognized that on the average the SNDR performance is enhanced significantly. A further comparison reveals that for $R_o = 3$ and $f_{\text{IF}} \approx 0.1$ an SNDR improvement of over 50 dB can be obtained.

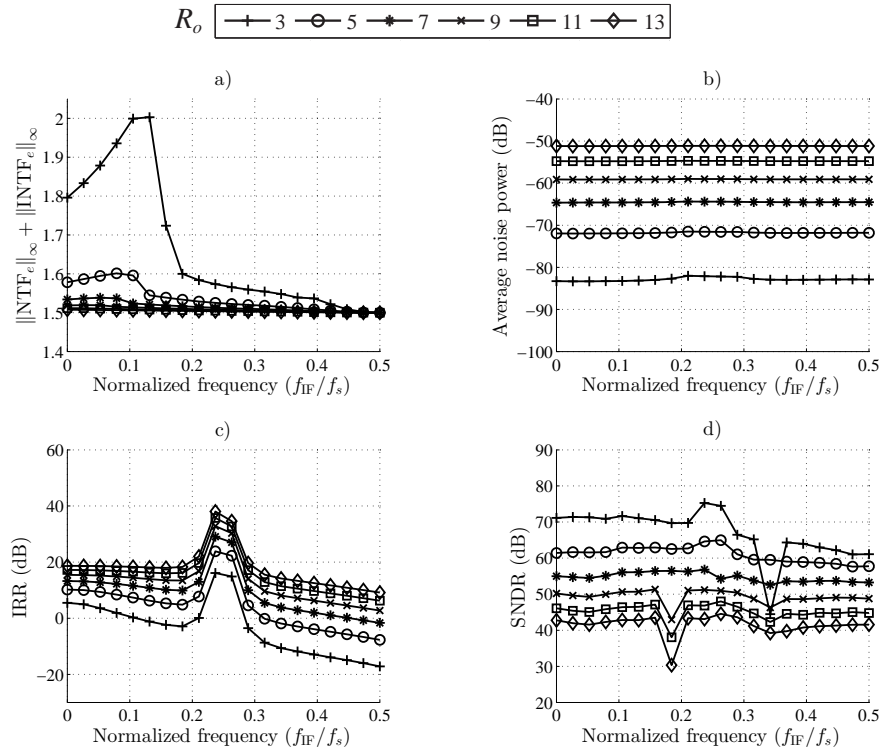


FIGURE 4.12: Evaluation of a) Maximum compensated NTF gain, b) compensated NTF average noise power, c) IRR and d) SNDR for various R_o settings.

4.6.3 Delay based compensation

In order to evaluate the performance of the delay based compensation technique, 12^{th} order complex all-pass FD filters were computed for the considered f_{IF} settings using the optimization technique presented in Section 4.4.3. The maximum gain constraint was set equal to 1.5 and the desired image rejection rate was set equal to -60 dB. The compensated NTFs were implemented by error-feedback noise shaper topologies.

Since the magnitude responses of the FD filters are only approximately of all-pass type, the maximum gain of the estimated filters affect the maximum gain of the compensated NTFs. This effect is shown in Figure 4.14 a). Clearly, the deviation from the all-pass response grows with increasing f_{IF} , which results in a worst case increment in the NTF maximum gain between 10% – 33%. The nearly static average noise power results given in Figure 4.14 b) indicate the fact that

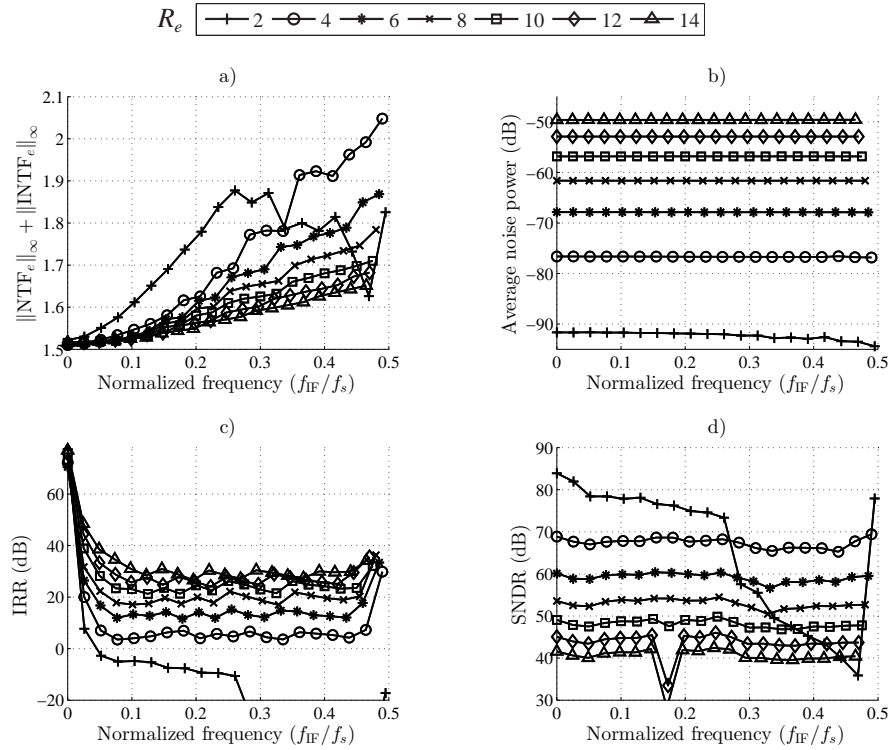


FIGURE 4.13: Evaluation of digital up-conversion technique with delay based compensation for a) maximum compensated NTF gain, b) compensated NTF average noise power, c) IRR and d) SNDR for various R_e settings.

the magnitude responses of the complex all-pass filters are sufficiently flat over the signal band.

In comparison to the additive compensation technique for R_e settings the delay based compensation employing the FD filters improves the IRR performance even further as seen from Figure 4.14 c). Apart from $R_e = 2$ the dB scaled IRR results are well above zero for every normalized f_{IF} setting. The decreased IRRs for $R_e = 2$ and $f_{IF}/f_s > 0.25$ are due to the above given maximum gain constraint set for the FD filter optimization. The SNDR performance given in Figure 4.14 d) for $4 \leq R_e \leq 14$ is nearly constant, which demonstrates successful conjugate quantization noise rejection. In addition, for $R_e = 2$ the conjugate quantization noise cancellation, albeit imperfect, delivers again up to 50 dB improvement of the dynamic range.

4.6.4 NTF magnitude response equalization based compensation

The conjugate quantization noise mitigation by additional noise shaping was implemented as described in Section 4.4.4 for the given simulation settings. Since the required magnitude response equalization with a 2nd order prototype NTF leads to a 4th order compensated NTF, the maximum prototype NTF gain was set to 1.2 in order to ensure the stability of the compensated modulator. Furthermore, the conjugate image NTFs were designed so that a minimum IRR margin of 3 dB was guaranteed.

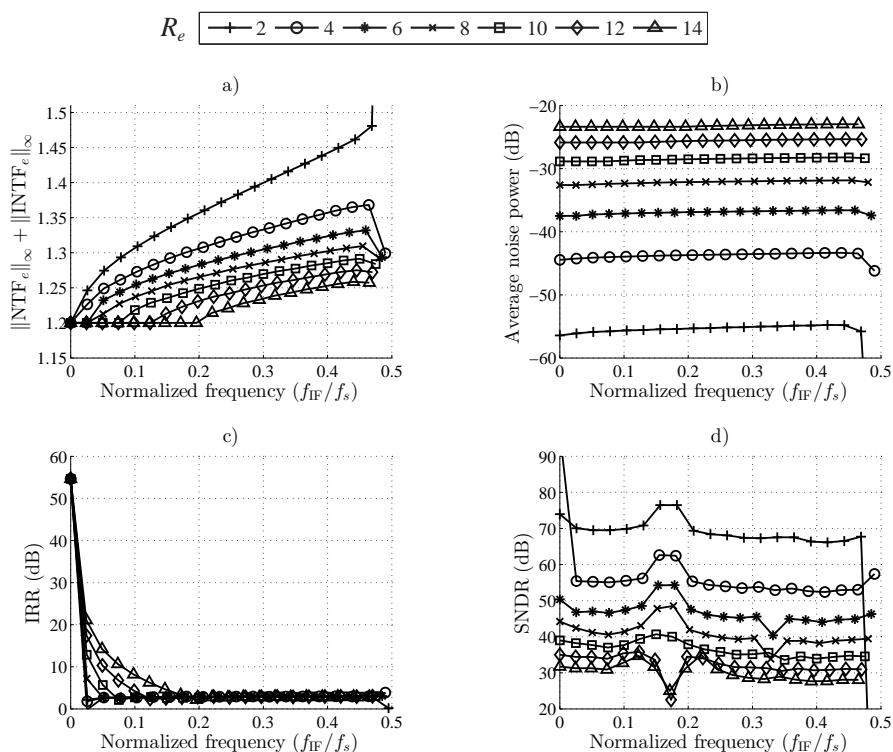


FIGURE 4.14: Evaluation of digital up-conversion technique with NTF magnitude response equalization based compensation for a) maximum compensated NTF gain, b) compensated NTF average noise power, c) IRR and d) SNDR for various R_e settings.

The increment in maximum compensated NTF gain due to the noise shaping at the conjugate band is illustrated for R_e settings in Figure 4.14 a). For the considered prototype NTFs the growth of the maximum compensated NTF gain is more subtle for higher R_e due to lower average NTF noise power. However, for

lower R_e with higher OSR and, thus, higher average NTF noise power as well, the need for the compensation becomes more prominent. This in the end leads to higher compensated NTF gain and, therefore, a lower maximum gain setting shall be considered for the prototype NTF with $N > 2$. The constrained maximum NTF gains cause evidently loss in an achievable dynamic range as suggested by the average noise power results shown in Figure 4.14 b). This is a drawback especially in the case when moderate OSRs are available for the baseband sequence encoding.

The IRR and SNDR results shown in Figure 4.14 c) and d) confirm the fact that the properly applied conjugate image NTFs enable suppression of the conjugate quantization noise at the signal band below the signal band quantization noise for arbitrary f_{IF} of R_e settings. However, despite theoretically conjugate quantization noise free operation the SNDR results are for most of the simulation settings inferior to those obtained by delay based or additive compensation methods. In addition it shall be noted that the involved additional noise shaping affects the magnitude of the input sequence to the PWM block of the Q Σ Δ PWM modulator. This may lead to modified noise shaping properties due to enhanced quantizer gain.

The same argumentation given above for R_e settings holds also for R_o settings regarding the maximum compensated NTF gain. At $f_{IF} = 0$ the average power of the conjugate quantization noise at the signal band is the largest, which causes an increment in the maximum compensated NTF gain of approximately between 4%–14% depending on the R_o setting. On the other hand as visible in Figure 4.15 a) near $f_{IF}/f_s = 0.25$ the signal and the conjugate band NTF stop-bands overlap, which relaxes the image rejection requirements. The average noise power levels given in Figure 4.15 b) are again decreased due to the limited prototype NTF maximum gain.

With properly adjusted conjugate signal band noise shaping settings the conjugate quantization noise can be rejected also in the case of R_o settings. The IRR evaluations shown in Figure 4.15 c) validate this proposition for the linearized modulator model. By observing the SNDR values from Figure 4.15 d) it becomes clear that

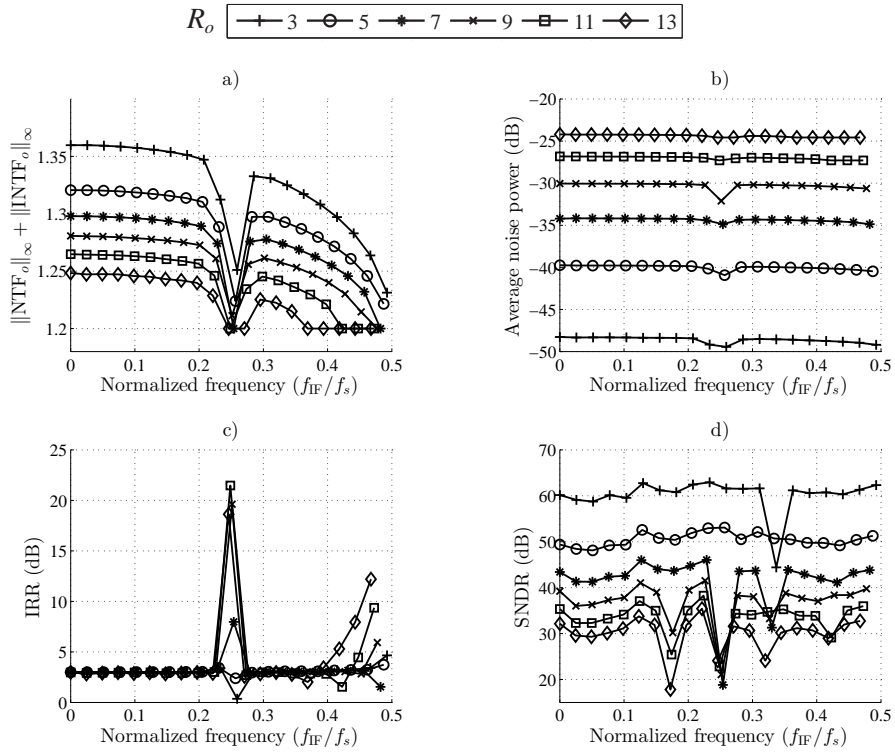


FIGURE 4.15: Evaluation of digital up-conversion technique with NTF magnitude response equalization based compensation for a) maximum compensated NTF gain, b) compensated NTF average noise power, c) IRR and d) SNDR for various R_o settings.

except for a few f_{IF} settings, for which the PWM harmonics and the conjugate image folding degrades the SNDR a nearly constant distortion performance can be guaranteed over the entire f_{IF} tuning range.

4.6.5 Conjugate signal compensation

The performance of the approximative conjugate signal suppression technique given in Section 4.5 was assessed by simulating Q $\Sigma\Delta$ PWM with both compensated and uncompensated excitation. Since the conjugate signal folding is relevant for limited f_θ settings, only $f_\theta = 3\text{MHz}/f_s$ for R_e and $f_\theta = 0.5 + 3\text{MHz}/f_s$ for R_o configurations were considered. For these settings the conjugate signal image locates in the signal band in all of the encoded pulsed sequences. The conjugate quantization noise compensation for these simulation settings is not necessary, since the corresponding IRRs are positive.

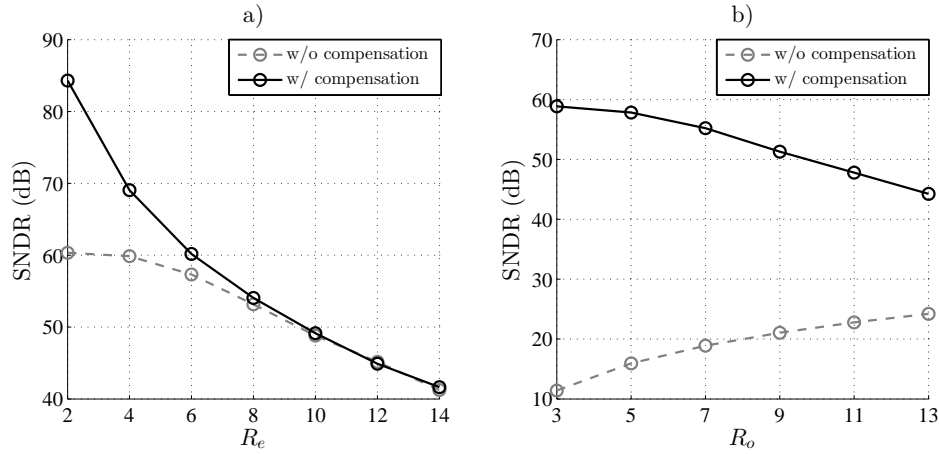


FIGURE 4.16: SNDR performance without conjugate signal compensation (dashed line) and with conjugate signal compensation (thick line) for a) R_e settings and b) R_o settings.

As visible from Figure 4.16 a) the improvement in SNDR due to the suppression of the conjugate signal is notable here mainly for $R_e \leq 8$. For those settings, the compensation method is able to restore the dynamic range close to that of the encoded baseband sequence. Given that for R_e settings the conjugate signal image is already suppressed to some extent by $H_{ma,c,e}(j\omega)$ near $f_{IF} = 0$, the average power of the inherently suppressed conjugate signal image is below average power of the quantization noise on the signal band when $R_e \geq 10$.

On the other hand, as explained in Section 4.2, for R_o settings $H_{ma,c,o}(j\omega)$ delivers only a minor suppression to the conjugate signal image. This effect is observable in Figure 4.16 b). The SNDR performance between 10–25 dB for the uncompensated excitation confirms the fact that the conjugate signal folding for R_o settings causes much severer degradation to the dynamic range. With compensation an improvement in SNDR of up to 50 dB can be obtained. Due to the rough approximation of $\Gamma_o(j\omega)$ by a constant multiplication the applied compensation achieves only partial suppression. This is valid for the considered lower R_o settings for which the SNDR is degraded from the equivalent baseband performance by approximately 10 dB.

4.7 Summary

This chapter discussed the digital up-conversion technique and its suitability for center frequency agile quadrature type digital transmitters. According to theoretical analysis the inherent quadrature imbalance of the digital up-conversion leads next to a conjugate signal image also to conjugate quantization noise folding. The conjugate quantization noise content in the signal band causes reduced SNDR and hence, limits the f_c tuning severely.

It turned out that the imbalance problem can be effectively solved by a linear, equalizing pre-compensation system. With complex baseband imbalance models of the digital up-conversion, three solutions were obtained. The first one applies a method frequently used in quadrature $\Sigma\Delta$ data converters, where additional noise shaping to the conjugate quantization noise content is applied. The second and the third technique are based on cancelation of the conjugate quantization noise image by modifying the phase and the magnitude of the quantization noise. Subsequently, with suitable approximations the linear compensating systems can be embedded in a noise shaping loop.

The conjugate quantization noise and conjugate image rejection performance was determined for various modulator settings by a linearized model of the Q $\Sigma\Delta$ PWM as well as by extensive simulations. According to the IRR and SNDR evaluations, a nearly full compensation can be achieved for many f_s and f_{IF} settings with all three compensation techniques over the entire Nyquist range. Furthermore, the cancelation based compensation techniques resulted in overall improved SNDR in comparison to the noise shaping based compensation. This is the primary advantage of the quantization noise cancelation. Without excess conjugate band noise shaping, the quantization noise can be optimized only around the signal band, which leads to a stronger noise shaping effect.

In summary, the appropriately compensated complex baseband encoding combined with the digital up-conversion method constitutes a powerful way to produce pulsed RF sequences with a flexible f_c tuning. This enables quadrature type

digital transmitters supporting simultaneously multiple communication standards operating on various channels.

Chapter 5

Behavioral modeling of the power amplification stage

As mentioned in earlier Chapters, the fully digital pulsed RF signal encoding is not prone to analog circuitry based non-ideal effects typical to an analog RF transmitter signal generation part. However, digital to analog conversion of the pulsed RF sequence and power amplification of the corresponding pulsed RF signal will lead to a distorted version of the ideal two-level sequence and hence, potentially to an increased unwanted residual signal content around the signal band. This behavior is undesirable, since despite the mitigation of out-of-band quantization noise by means of a reconstruction filter a large amount of in-band and adjacent channel distortion will limit the usage of the digital transmitter for wireless communication networks with high transmission signal linearity constraints. This chapter will present novel methods to characterize the analog component related distortion effects in a computationally cost effective way.

5.1 Equivalent complex baseband nISI model

The characterization of nISI by the generalized nISI model becomes computationally exhaustive due to the exponential growth in number of terms to estimate when

the memory depth is large. This characteristic becomes an issue when the pulsed RF signal is subject to long-term non-linear memory effects, which result in higher order nISI terms. Obviously it is desirable to find nISI models with reduced complexity, which show a performance that is close or equal to the generalized nISI models.

A potential way to reduce the computational burden is to consider modeling of the encoded complex baseband sequences instead of the pulsed RF sequence. This technique enjoys the same benefits of the equivalent complex baseband modeling of non-linear pass-band systems [83], namely the lower computational memory requirements for block type identification, less training data and perhaps most important, relaxed computational complexity. Since the encoding of the digital transmitter considered in this Thesis is performed in over-sampled digital baseband, the aforementioned method is a preferable choice.

5.1.1 Model derivation

An initial step to construct an nISI model for the complex baseband sequences is to reformulate the complex imbalance model given in Section 4.1 for digital up-conversion in terms of the real valued $pwm_I(n)$ and $pwm_Q(n)$ sequences.

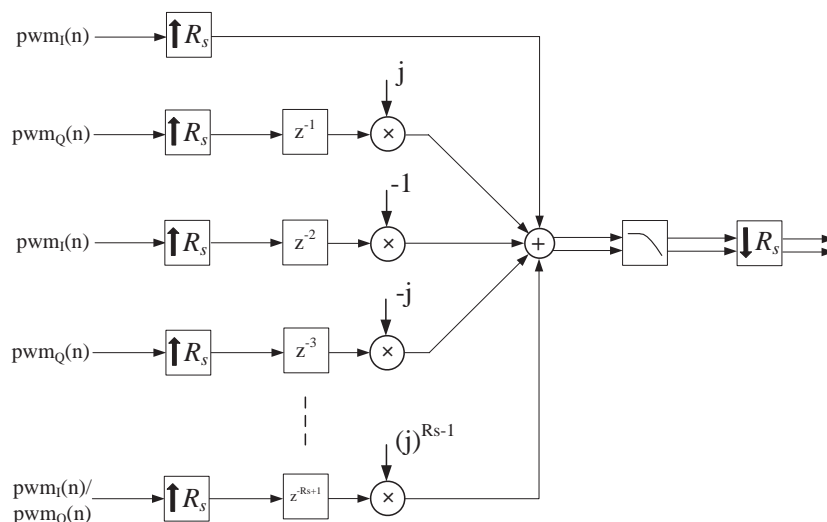


FIGURE 5.1: Alternative complex baseband representation of the digital up-conversion.

Alternatively, (2.5) can be described by interleaving the corresponding $pwm_I(n)$ and $pwm_Q(n)$ with proper signs and delay components. By applying down-conversion by a multiplication with $e^{-jn\pi}$ and re-sampling leads to an alternative representation of (4.3) illustrated in Figure 5.1. Thus, the model output $pwm_{bb}(n)$ can be expressed as a re-sampled version of

$$pwm_{bb,o}(n) = \sum_{i=1}^{\lfloor \frac{R_s}{2} \rfloor} pwm_I(n) z^{2(i-1)} (-1)^i + j \sum_{i=1}^{\lfloor \frac{R_s}{2} \rfloor} pwm_Q(n) z^{2i-1} (-1)^{i-1}. \quad (5.1)$$

Next, by recognizing that the operations contained in the parallel branches in Figure 5.1 can be substituted by an FD element followed by a multiplication, $pwm_{bb}(n)$ simplifies to

$$pwm_{bb}(n) = \sum_{i=1}^{\lfloor \frac{R_s}{2} \rfloor} pwm_I(n) z^{(2i-2)/R_s} (-1)^i + j \sum_{i=1}^{\lfloor \frac{R_s}{2} \rfloor} pwm_Q(n) z^{(2i-1)/R_s} (-1)^{i-1}. \quad (5.2)$$

This kind of decomposition of the quadrature imbalance related to the digital up-conversion gives information on how a single pulsed RF symbol affects $pwm_{bb}(n)$ and thus, becomes a good starting point for the equivalent complex baseband nISI model.

The next step is to consider which complex baseband symbols are present in the nISI sequences given that $M_{RF} = MR_s$, where M is a positive integer. In order to simplify the analysis it is convenient to investigate an exemplary case, where $M = 1$ and $R_s = 4$. Additionally for convenience, let $I_n = pwm_I(n)$ and let $Q_n = pwm_Q(n)$. Figure 5.2 shows the four distinct sets of symbols involved for each of the four RF pulse timing instants. Given that $I_n^{2k} = Q_n^{2k} = 1$, $I_n^{(2k-1)} = I_n$ and that $Q_n^{(2k-1)} = Q_n$ the relevant nISI terms contained in each of the sets include the constant term and the sub-sets $s_{k,n,4}$, $1 \leq k \leq 4$ containing only the unique symbol elements. In the exemplary case these sub-sets are given on the right-hand

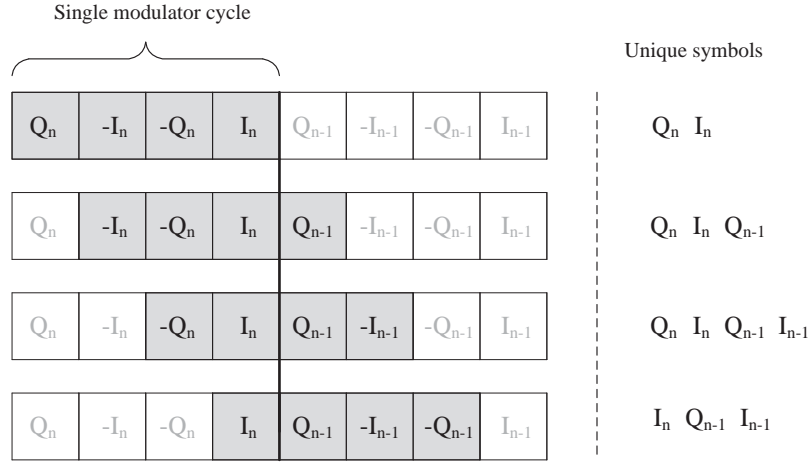


FIGURE 5.2: Complex baseband symbols involved when nISI memory depth is equal to $R_s = 4$.

side in Figure 5.2. Finally, the nISI for the given settings stems from the products between the elements of $s_{k,n,4}$.

The unique symbol elements for each n in the general case with arbitrary $R_s > 3$ and M can be found straightforwardly by extending the example case. As it turns out, there are four distinct cases. At first, when $k = 1$ there are $2M$ unique elements in $s_{1,n,M}$ since in the RF bit domain a memory depth of R_s covers only the symbols of a single modulator cycle. In the case of $k = 2$ the cardinality of $s_{2,n,M}$ is equal to $2M + 1$ as the involved symbols include those from $s_{1,n,M}$ and an additional symbol due to an index shift by one. For $3 \leq k \leq R_s - 1$ there are in total $2M + 2$ symbol terms as in this case $s_{k,n,M}$ is a super-set containing $s_{1,n,M}$ and two additional symbols. At last, when $k = R_s$ the cardinality of $s_{R_s,n,M}$ becomes $2M + 1$ as $s_{R_s,n,M}$ is a sub-set of $s_{R_s-1,n,M}$ excluding one of the first of the two symbols with time index n . Given the information on all possible unique symbol sets, the equivalent complex baseband model can be formulated as follows

$$\begin{aligned}
 pwm_{isi}(n) = & h_0 + \sum_{i=1}^{2^{2M}} h_{1,i} \text{ISI}_i s_{1,n,M} + z^{-1/R_s} \sum_{i=1}^{2^{2M+1}} h_{2,i} \text{ISI}_i s_{2,n,M} \\
 + \sum_{k=3}^{R_s-1} h_{k,i} z^{-(k-1)/R_s} \sum_{i=1}^{2^{2M+2}} \text{ISI}_i s_{k,n,M} + z^{-(R_s-1)/R_s} \sum_{i=1}^{2^{2M+1}} h_{R_s,i} \text{ISI}_i s_{R_s,n,M}, \quad (5.3)
 \end{aligned}$$

where

$$\begin{aligned}
s_{1,n,M} &= \{Q_n, I_n, \dots, Q_{n-M}, I_{n-M}\}, \\
s_{2,n,M} &= \{Q_n, I_n, \dots, Q_{n-M}, I_{n-M}, Q_{n-M-1}\}, (R_s = R_e) \\
s_{2,n,M} &= \{Q_n, I_n, \dots, Q_{n-M}, I_{n-M}, I_{n-M-1}\}, (R_s = R_o) \\
s_{k,n,M} &= \{Q_n, I_n, \dots, Q_{n-M-1}, I_{n-M-1}\}, (3 \leq k \leq R_s - 1) \\
s_{R_s,n,M} &= \{I_n, \dots, Q_{n-M-1}, I_{n-M-1}\}, (R_s = R_e) \\
s_{R_s,n,M} &= \{Q_n, \dots, Q_{n-M-1}, I_{n-M-1}\}, (R_s = R_o). \tag{5.4}
\end{aligned}$$

The two remaining R_s settings, namely $R_s = 2, 3$ can be treated as special cases. For $R_s = 3$ in (5.3) the only active sub-sets are $s_{1,n,M}, s_{2,n,M}$ and $s_{3,n,M}$ and for $R_s = 2$ the respective active sub-sets are $s_{1,n,M}$ and $s_{2,n,M}$.

5.1.2 Model parameter estimation

Given that (5.3) is linear in its parameters, linear regression can be utilized for the parameter estimation. This technique is often applied to perform fitting of discrete time Volterra models [84] based on batch processing, which is the aim here as well. Firstly, (5.3) can be expressed for a given finite excitation sequence of length L in matrix form as follows

$$\mathbf{pwm}_{isi} = \mathbf{\Phi} \mathbf{h}, \tag{5.5}$$

where

$$\begin{aligned}
\mathbf{\Phi} &= \begin{bmatrix} 1 & \mathbf{i}_{1,1} & \mathbf{i}_{2,1} & \mathbf{i}_{k,1} & \mathbf{i}_{R_s,1} \\ \vdots & \vdots & \vdots & \vdots & \vdots \\ 1 & \mathbf{i}_{1,L} & \mathbf{i}_{2,L} & \mathbf{i}_{k,L} & \mathbf{i}_{R_s,L} \end{bmatrix} \\
\mathbf{i}_{1,l} &= \left[\text{ISI}_{1s_{1,l,M}} \cdots \text{ISI}_{2^{2M}s_{2^{2M},l,M}} \right]^T \\
\mathbf{i}_{2,l} &= \left[\text{ISI}_{1s_{2,l,M}} \cdots \text{ISI}_{2^{2M+1}s_{2^{2M+1},l,M}} \right]^T \\
\mathbf{i}_{k,l} &= \left[\text{ISI}_{1s_{k,l,M}} \cdots \text{ISI}_{2^{2M+2}s_{2^{2M+2},l,M}} \right]^T, \quad (3 \leq k \leq R_s - 1) \\
\mathbf{i}_{R_s,l} &= \left[\text{ISI}_{1s_{R_s,l,M}} \cdots \text{ISI}_{2^{2M+1}s_{2^{2M+1},l,M}} \right]^T \\
\mathbf{h} &= \left[h_0 \ h_{1,1} \cdots h_{1,2^{2M}} \ h_{2,1} \cdots h_{2,2^{2M+1}} \ h_{k,1} \cdots h_{k,2^{2M+2}} \ h_{R_s,1} \cdots h_{R_s,2^{2M+1}} \right]^T \\
\mathbf{pwm}_{isi} &= \left[pwm_{isi}(1) \cdots pwm_{isi}(L) \right]^T. \tag{5.6}
\end{aligned}$$

A cost function that delivers the squared error between a training sequence \mathbf{pwm}_{train} and \mathbf{pwm}_{isi} becomes

$$J_{isi} = \|(\mathbf{pwm}_{train} - \mathbf{\Phi h})\|^2. \tag{5.7}$$

Finally, the least squares solution \mathbf{pwm}_{isi} that minimizes J_{isi} can be obtained by pseudo inverse [85] as follows

$$\mathbf{pwm}_{isi} = (\mathbf{\Phi}^H \mathbf{\Phi})^{-1} \mathbf{\Phi}^H \mathbf{pwm}_{train}. \tag{5.8}$$

5.1.3 On the excitation sequence

Similar to the real valued nISI model (2.10) the equivalent baseband model (5.3) can be interpreted as an alternative representation of the LUT model as well. Thus, an arbitrary sequence of interleaved real and imaginary symbols corresponds to a distinct complex valued output look-up table entry. For a correct model behavior, the look-up table shall have an entry for every distinct combination of the sets (5.4). On the contrary, a missing entry would lead to inadequate modeling performance.

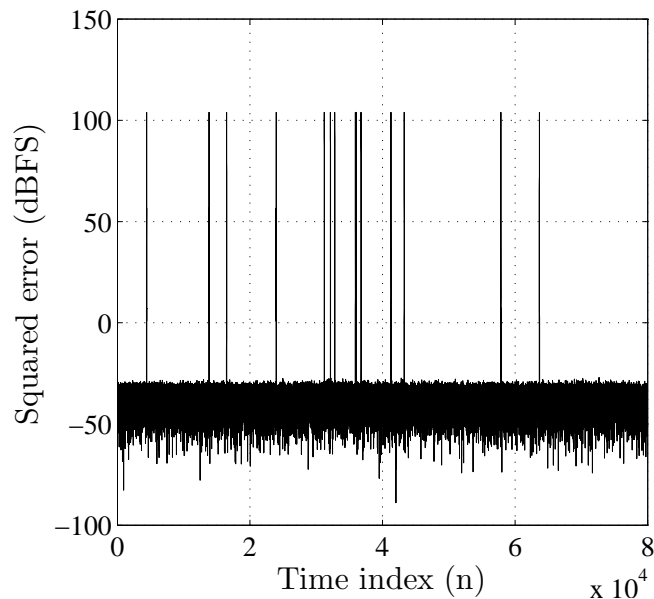


FIGURE 5.3: Modeling error depicted in time domain for inadequately estimated reference nISI system.

From a model parameter estimation point of view, for (2.10) to be equivalent with a correctly functioning look-up table model, the training shall be performed with excitation sequences which contain all possible symbol combinations for a given M . An inadequate excitation including only a sub-set of the full symbol set leads to a malfunctioning model. This [behavior](#) is illustrated in Figure 5.3, where the squared error is calculated between the model output and the reference system output. In this case $M = 3$ and the excitation sequence of length 12000 is a 10 MHz LTE sequence encoded by Q Σ Δ PWM with $f_s = 833$ MHz. After parameter estimation, the obtained model was excited with another, similar validation sequence of length 80000. It is clearly visible from Figure 5.3 that the parameter estimation with insufficient excitation causes bursty errors. The large error magnitude can be explained by ill-conditioned $\Phi^H \Phi$ in (5.8), which in turn leads to large variations in the estimated model coefficients.

The above example rises an important question regarding the block type model fitting: What is the largest M that yields a consistently estimated model when a reasonably long excitation is encoded by Q Σ Δ PWM? This is a relevant issue when the modeling is e.g. utilized as a part of an on-line pre-distortion system. In such a case the only excitation available is the encoded baseband sequence.

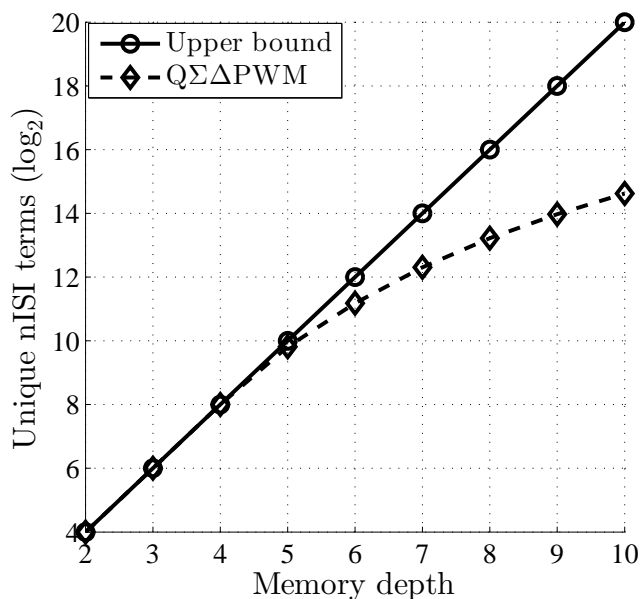


FIGURE 5.4: Number of unique complex symbol sequences included in QΣΔPWM encoded sequence for various M .

An answer to the above stated question can be easily obtained by analyzing the set of unique symbols (5.4) for a given excitation sequence and M . An example result for such a computation is illustrated in Figure 5.4, where the unique sets are evaluated for the above described QΣΔPWM encoded validation sequence of length 80000 and $2 \leq M \leq 10$. In this case for the memory depths $2 \leq M \leq 4$ the sub-sets in (5.4) contain all the possible symbol combinations. On the contrary, for $M > 4$ this property is not more valid for the considered excitation.

5.2 Experimental time delay neural network based complex baseband model

The exploitation of the redundancy in the pulse encoded sequence led to savings in computational complexity in comparison to the real valued generalized nISI model. However, the number of the nISI terms still grows exponentially as a function of the memory depth. This is undesirable especially in the case when the PA stage exhibits long-term memory effects and the carrier OSR is low. In that case the computational complexity of the equivalent complex baseband model

becomes close to that of the generalized nISI model. Therefore, in this Section an experimental complex baseband modeling technique is studied, which shall lead to further savings in the computational burden.

5.2.1 Model description

For equivalent baseband modeling purposes of RF PAs with continuous RF signal input signals a number of low-complexity models including simplified Wiener and Hammerstein models [86], parallel versions of the latter [87] as well as memory polynomials [88] have been proposed. These models can be considered as simplified versions of the full-blown Volterra series representation. Recently, artificial neural network (ANN) based models have been shown to outperform some of the above listed models for the modeling of wide-band RF transmitters [89]. Moreover the theoretical results indicate that an ANN can be used to identify Volterra models [90] as well as non-linear models with discontinuities [91]. Hence, it is appealing to apply ANNs to the complex baseband modeling of nISI.

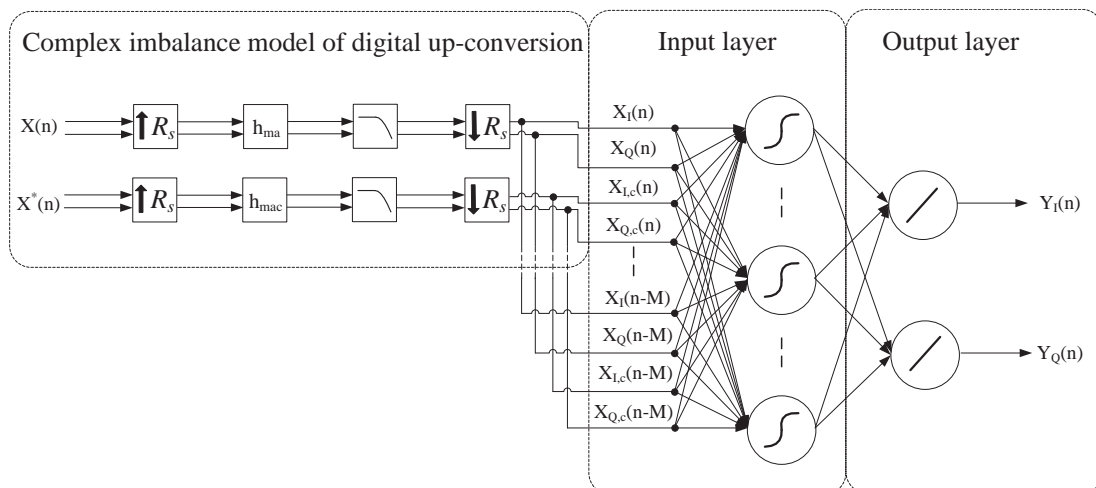


FIGURE 5.5: Time delay neural network based complex baseband nISI model.

The proposed experimental ANN based model is depicted in Figure 5.5. The model is composed of a pre-conditioning block, which regenerates the complex imbalance of the digital up-conversion and a two layer time delay neural network (TDNN), capturing the nISI effects. As it turns out this separation is helpful to reduce the computational complexity. The pre-condition block is essentially equivalent with

the complex imbalance model (4.3). However, instead of summing the conjugate image at the output of the block, the real valued components of the non-conjugate and the conjugate versions of the encoded baseband sequence, namely $x_i(n)$, $x_q(n)$, $x_{i,c}(n)$ and $x_{q,c}(n)$ are fed to the input of the TDNN block. The nISI terms are generated in the input layer of the TDNN, which consists of four delay lines of depth M_i connected to N_i activation functions, which are of sigmoid type. It shall be noticed that at least two activation functions are required to allow for a correct mapping of the real and imaginary components of the input sequence. Finally, the output sequence is composed in the output layer, which consists of two linear activation functions. The input-output relation of the TDNN block can be described as

$$y(n) = f_o(\mathbf{C}_o f_i(\mathbf{x}^T \mathbf{C}_i)) \mathbf{j}, \quad (5.9)$$

with the following vector variables

$$\begin{aligned} \mathbf{C}_i &= \begin{bmatrix} c_{i,1,1} & \cdots & c_{i,1,N_i} \\ \vdots & \ddots & \vdots \\ c_{i,4M_i,1} & \cdots & c_{i,4M_i,N_i} \end{bmatrix} \\ \mathbf{C}_o &= \begin{bmatrix} c_{o,1,1} & c_{o,1,2} \\ \vdots & \vdots \\ c_{o,N_i,1} & c_{o,N_i,2} \end{bmatrix} \\ \mathbf{j} &= [1 \ j]^T \\ \mathbf{x}_i &= [x_i(n), \cdots, x_i(n - M_i)]^T \\ \mathbf{x}_q &= [x_q(n), \cdots, x_q(n - M_i)]^T \\ \mathbf{x}_{i,c} &= [x_{i,c}(n), \cdots, x_{i,c}(n - M_i)]^T \\ \mathbf{x}_{q,c} &= [x_{q,c}(n), \cdots, x_{q,c}(n - M_i)]^T \\ \mathbf{x} &= [\mathbf{x}_i^T, \mathbf{x}_q^T, \mathbf{x}_{i,c}^T, \mathbf{x}_{q,c}^T]^T. \end{aligned} \quad (5.10)$$

The model complexity is dominated by the structure of the TDNN block. Obviously the total number of input and output layer weights is $4M_i N_i + 2N_i$, which results in an equivalent number of multiplications. Secondly, the evaluations of the

activation functions $f_i(\cdot)$ and $f_o(\cdot)$ adds to the computational load. Nevertheless, the model complexity does increase now as a polynomial function of M_i and N_i .

A further positive aspect of TDNN is associated to the stability of the model. Albeit the variants of ANNs with feedback connections, such as recurrent neural networks may yield a performance gain as presented in [89], the boundedness of the layer state variables has to be taken into account during the modeling [92]. Due to an open-loop structure, such analysis is not necessary for the TDNN block.

A noteworthy drawback of the TDNN based model is related to the separation between the complex imbalance model and the nISI generation. By interpreting the complex imbalance regeneration block as the parallel all-pass filter representation given by 5.2, it becomes clear that the input layer activation functions receive all fractionally delayed input sequence components. Therefore, the sigmoid function output contains undesired mixed products between the differently delayed components. These residual products may reduce the modeling performance. However, the external complex imbalance model is the key to lower the computational complexity, which is a highly desired feature in e.g. real-time applications.

5.2.2 Model parameter estimation

The TDNN block weights \mathbf{C}_i and \mathbf{C}_o are trained by the popular Levenberg-Marquard back-propagation algorithm [93]. This gradient based training method is designed to perform parameter estimation for multi-layer ANNs. The cost function for the training algorithm is defined as

$$J_{tdnn} = \|(\mathbf{pwm}_{train} - \mathbf{y})\|^2, \quad (5.11)$$

where \mathbf{y} denotes a vector holding the evaluations of (5.9) for different time indexes. Here J_{tdnn} is a non-linear function of the weights contained in \mathbf{C}_i and \mathbf{C}_o . Hence, the minimization of (5.11) is a non-linear least squares optimization problem, which is solvable by the Levenberg-Marquard algorithm.

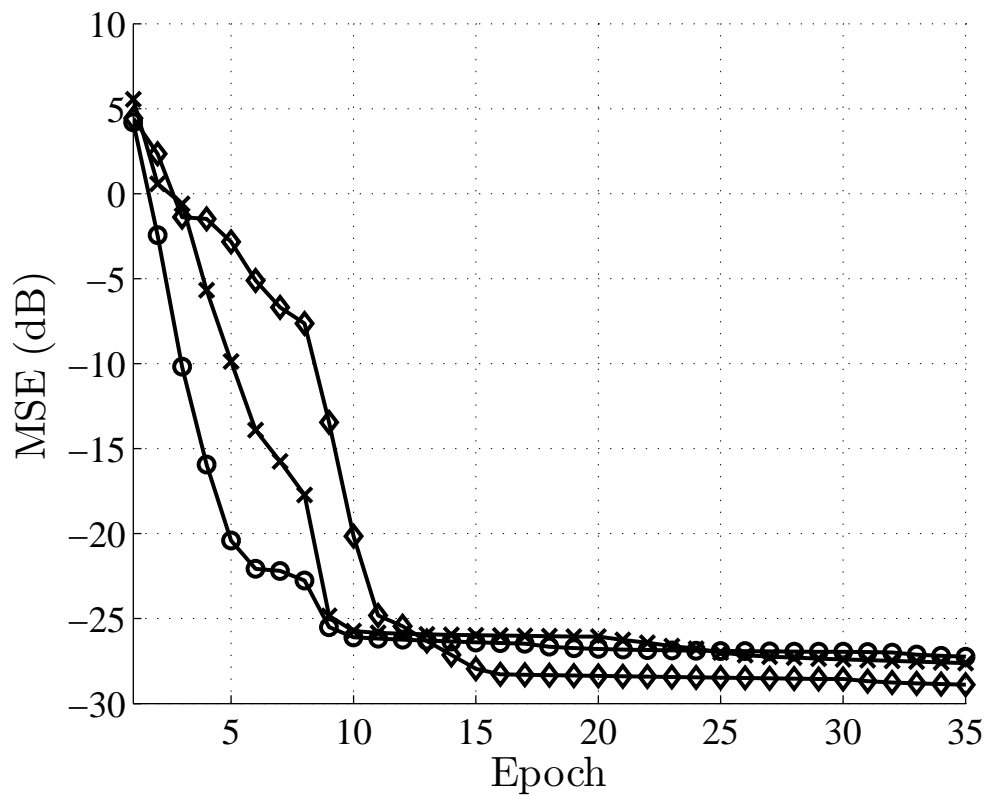


FIGURE 5.6: TDNN training performance for three training runs with random initial conditions.

Although it has been reported that the Levenberg-Marquard algorithm yields faster learning speed in comparison to the conventional gradient descent based back-propagation algorithms [93], the convergence to the global minimum cannot be guaranteed in general [94]. Instead, the training algorithm is likely to converge to a one of the multiple of local minima of (5.11), which results in a reduced modeling performance. The convergence performance is dependent on the selected parameters of the training algorithm as well as on the initial weights. The sensitivity to the initial model conditions is illustrated in Figure 5.6, where the TDNN fitting routine is performed three times for the same training data, but with random initial conditions. After 35 epochs, the difference between the best and the worst mean-square-error is approximately 3 dB.

5.3 Model validation

The last step in the behavioral modeling approach is to verify that the given models are functioning as desired. For the considered black-box modeling technique the validation involves modeling by multiple excitation signals with different f_c settings. For validation purposes two different setups will be considered. Firstly, an experimental simulation based setup will be utilized to demonstrate that the identification works flawlessly. Secondly, a measurement based setup is used to determine the performance of the given models for a realistic digital RF transmitter architecture in terms of accuracy and computational complexity.

5.3.1 Simulation and measurement setup

Figure 5.7 shows the details of the complete system used to perform the behavioral modeling. The parameters for Q $\Sigma\Delta$ PWM encoding with the additive conjugate quantization noise compensation as well as for digital up-conversion are those given in Table 5.1. It shall be furthermore stressed that $f_\theta = f_{IF}$ in every case. The parameters are common for identification of both simulation and measurement based systems.

TABLE 5.1: Modulator parameters

f_{sw}	R_s	f_{IF}, f_θ	f_{PWM}	$ NTF _\infty$	N
10 GHz	12	$(0-0.45)\frac{f_{sw}}{R_s}$	$\frac{f_{sw}}{6R_s}$	1.5	2

The experimental simulation setup consists of a two-box Wiener model composed of a FIR filter and a hyperbolic tangential static non-linearity. The sampling frequency of the simulations is equal to f_{sw} . As shown in [44], the Wiener model is a special case of the general nSI model. The motivation to utilize this model here is to produce long-term nSI effects in a computationally efficient way. The coefficients of the 48th order FIR filter are shown in Figure 5.8. The filter taps are generated randomly by a function $e^{(n/8+10^{-4})}\cos(2\pi X(n))$, where $X(n)$ denotes

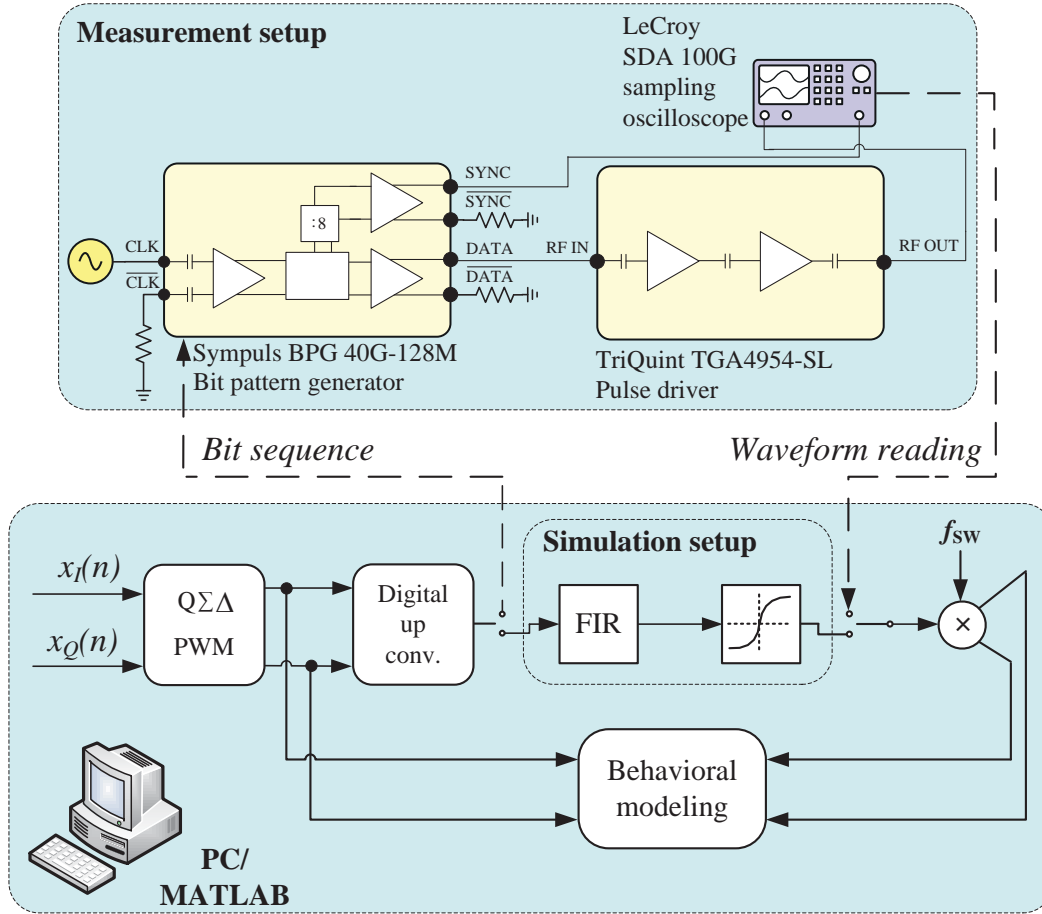


FIGURE 5.7: Simulation and measurement based setups for model validation purposes.

a discrete uniformly distributed random variable. This results in a non-linear dynamical reference system with fading memory, which represents an RF SMPA.

The measurement system shown in the upper part of Figure 5.7 consists of a Sympluls BPG 40G-128M bit-pattern generator, TriQuint TGA4954-SL Pulse driver and a LeCroy SDA 100G sampling oscilloscope. The generated RF bit sequences are transferred first to the bit pattern generator, which generates an analog pulsed excitation signal in a repetitive manner. The pulsed RF signal is amplified by the pulse driver and the respective output signal waveform is captured by the sampling oscilloscope. The bit pattern generator is clocked with a frequency equal to f_{sw} . The bit pattern generator and the sampling oscilloscope are synchronized with the same RF clock. The effective sampling rate of the captured RF waveform was chosen to be equal to $32f_{sw}$ in order to avoid aliasing.

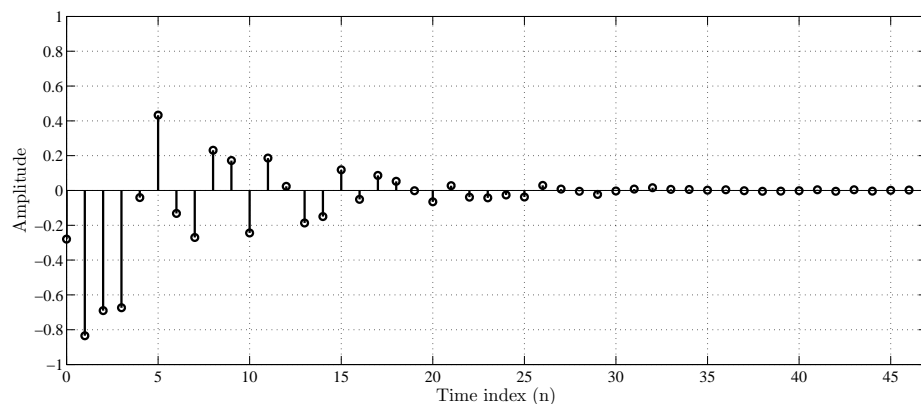


FIGURE 5.8: Coefficients of the FIR filter part of the Wiener model used in the simulation setup.

5.3.2 Figure of merits

An important part of the behavioral modeling is to find out how well the selected model reflects the true behavior of the reference system. For this reason, a multitude of FoMs have been introduced for RF PA modeling purposes.

The motivation in this thesis is to capture the nISI caused by non-linear dynamics of the PA stage. Hence, it is critical to consider those FoMs intended to assess the modeling performance of the nonlinear memory effects. According to the results given in [95] good evaluation criteria for RF PAs exhibiting strong non-linear memory effects include normalized mean square error (NMSE) and weighted error spectrum power ratio (WESPR) [96]. The former is a time domain error measure, whereas the latter is evaluated from spectrum estimates. The advantages of these two FoMs are independence of the excitation signal and capability to accurately assess the in-band as well as the out-of-band modeling performance.

NMSE is defined as

$$\text{NMSE} = \frac{\sum_{n=1}^L |y_{\text{mod}}(n) - y_{\text{meas}}(n)|^2}{\sum_{n=1}^L |y_{\text{meas}}(n)|^2}, \quad (5.12)$$

where $y_{\text{mod}}(n)$ denotes the output of the behavioral model and $y_{\text{meas}}(n)$ the measured output of the reference system, respectively. NMSE is often utilized to capture the in-band modeling performance. WESPR, on the other hand, can be

formulated as

$$\text{WESPR} = \frac{\int_{f_c-0.5f_b}^{f_c+0.5f_b} |W(f)E(f)|^2 df}{\int_{f_c-0.5f_b}^{f_c+0.5f_b} |Y_{meas}(f)|^2 df}, \quad (5.13)$$

where

$$W(f) = \frac{\max(|E(f)|)}{\max(|E(f)|) + |X(f)|} \quad (5.14)$$

is the soft threshold window and the $E(f) = Y_{meas}(f) - Y_{mod}(f)$ denotes the error spectrum of the measured and modeled output spectra and $X(f)$ the spectrum of the excitation signal. The multiplication by $W(f)$ gives more weight to the less energetic spectral content. Thus WESPR is more practical to evaluate the out-of-band modeling performance, where the distortion power is often lower than the in-band signal power.

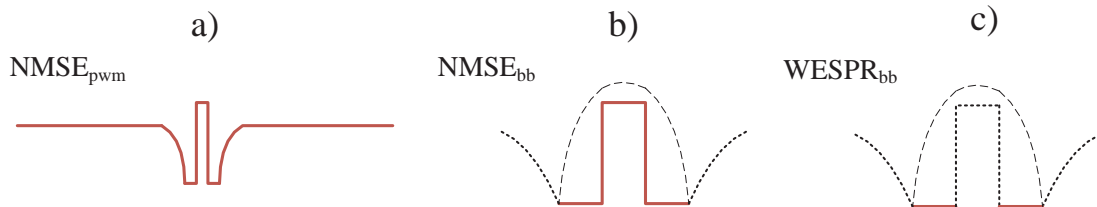


FIGURE 5.9: Illustrations on the proportions of the signal spectrum that are taken into account for a) NMSE_{pwm} b) NMSE_{bb} and c) WESPR.

In order to validate the performance of the equivalent complex baseband model, NMSE is calculated for the complete pulsed complex baseband sequences and denoted by NMSE_{pwm} . Secondly, the modeling efficiency is investigated in terms of NMSE and WESPR for the reconstructed baseband sequence, denoted by NMSE_{bb} and WESPR_{bb} , respectively. The parts of the spectrum that are taken into account for these FoMs are illustrated in Figure 5.9.

Finally, the computational complexity of the given nISI models will be assessed by [the number of multiplications](#) required for computation of a single output sample.

5.3.3 Validation results based on simulations

The initial model validations were performed using the simulation based Wiener model type reference system. The essential goal of the simulation based behavioral

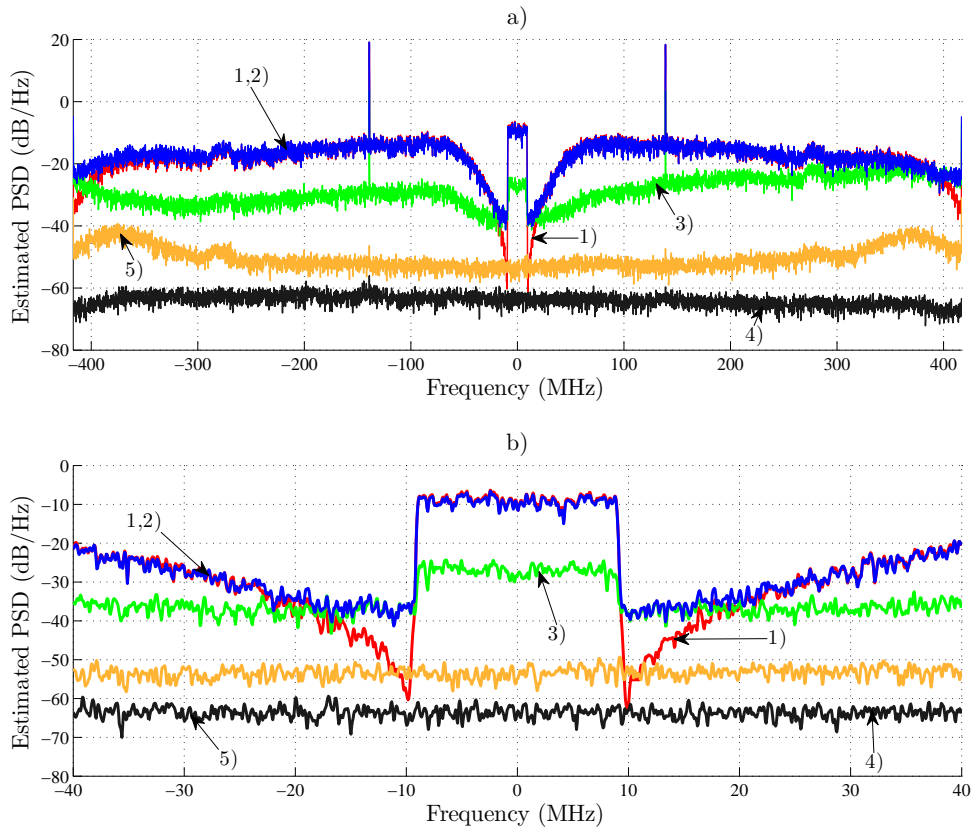


FIGURE 5.10: Simulated spectra shown a) over complete bandwidth of the encoded sequences b) near the signal band for 1) excitation 2) simulated output 3) error without modeling 4) error with equivalent nISI model 5) error with TDNN based model.

modeling is to verify that the proposed models are able to effectively capture the baseband proportion of the long term nISI effects. Moreover, the desired functionality of the chosen model fitting algorithms can be justified from the successful validation results.

Figure 5.10 a) presents spectra of 1) encoded pulsed excitation, 2) reference system output, 3) error without modeling, 4) modeling error for equivalent baseband nISI model with $M = 3$ and 5) modeling error for TDNN based model with $M_i = 10$ and $N_i = 10$. The first observation concerns the distortion due to nISI. As depicted in Figure 5.10 b) the in-band as well as adjacent channel distortion energy in 3) is significantly higher in comparison to the quantization noise power in 1). Secondly, also the amount of out-of-band nISI distortion in 3) is notable. The

noise like characteristics of 3) is due to the fact that the nISI causes the out-of-band quantization noise to fold back to the signal band.

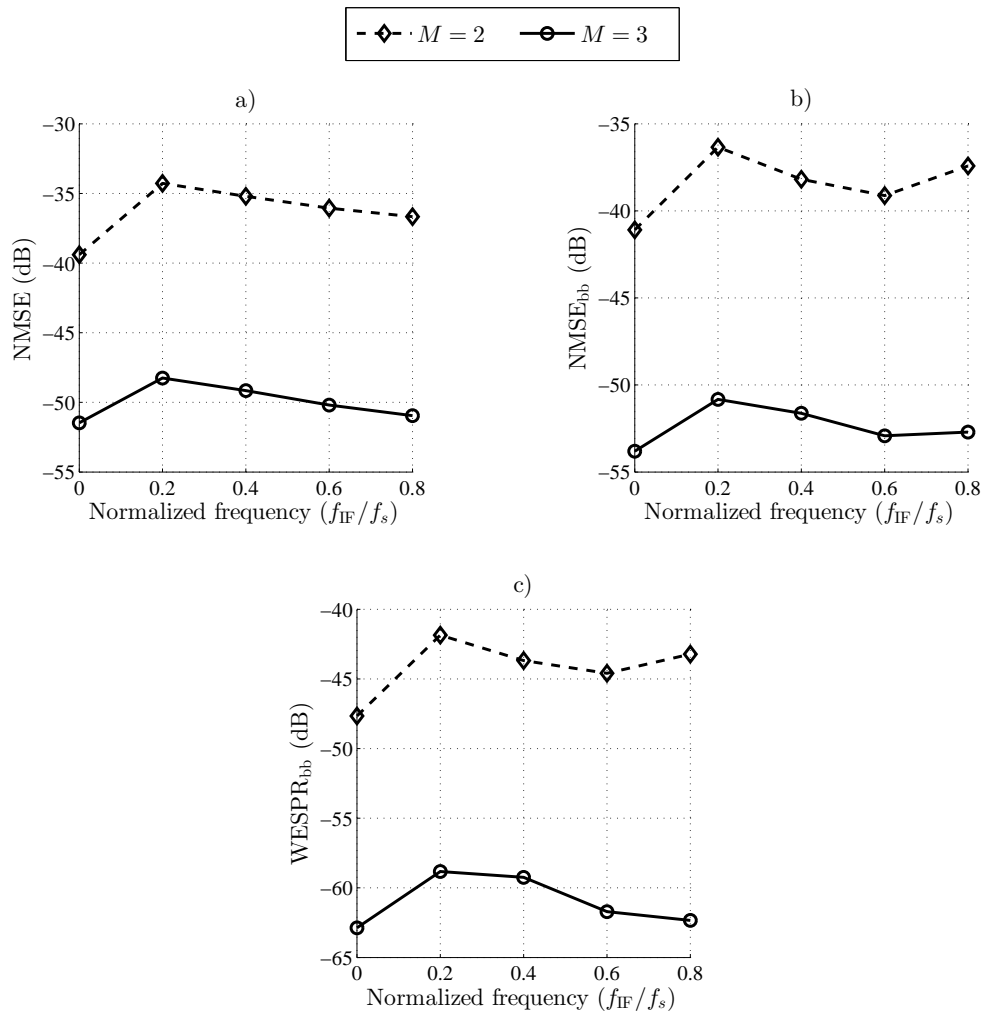


FIGURE 5.11: Simulation based modeling performance of the equivalent baseband nISI model in terms of a) NMSE b) $NMSE_{bb}$ and c) $WESPR_{bb}$, where $2 \leq M \leq 3$.

By observing the modeling error in 4) and by comparing it with 3) it becomes clear that the equivalent baseband nISI model identifies the reference Wiener model efficiently. Furthermore as visible in 5) the TDNN based model yields satisfactory modeling accuracy over the complete encoded baseband sequence.

Next, it is of interest to evaluate the FoMs given in Section 5.3.2 to gain a more detailed knowledge of the achieved modeling performance. In particular, as shown in the previous chapter the properly compensated Q Σ Δ PWM allows for continuous

adjustment of f_c . Therefore, in the following the effectiveness of the two models are evaluated for excitations with $f_{IF} \in [0, 0.2, 0.4, 0.6, 0.8]$.

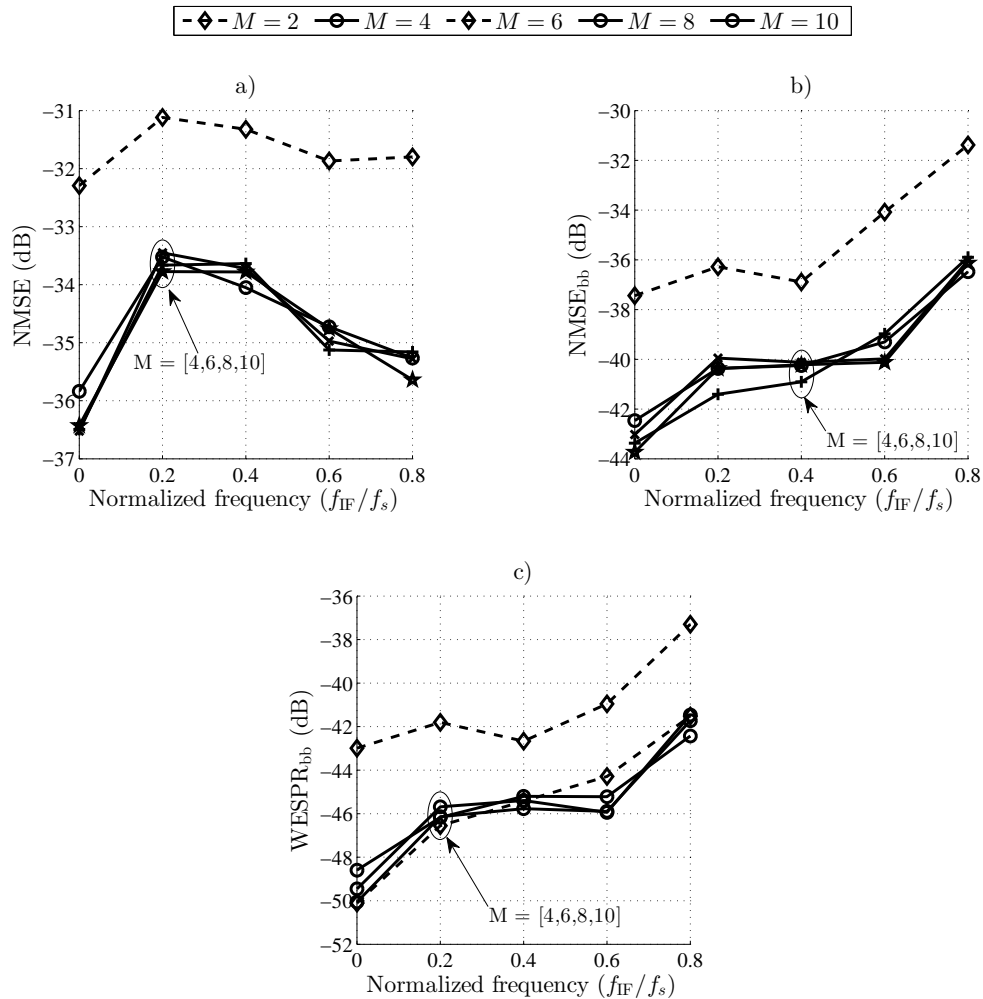


FIGURE 5.12: Simulation based modeling performance of the TDNN based nISI model in terms of a) NMSE b) NMSE_{bb} and c) WESPR_{bb}, where $M_i \in [2, 4, 6, 8, 10]$ and $N_i = 10$.

In figure 5.11 the considered FoMs are shown for equivalent baseband nISI model for $2 \leq M \leq 3$. It shall be noted that for $M > 3$ some of the excitation sequences are in violation with the necessary condition regarding the training sequence given in section 5.1.3. Therefore, in order to demonstrate accurate and reliable validation results, those parameters are omitted from the performed results. Nevertheless, it can be seen that for already $M = 2$ the complex equivalent nISI model performs well on both in-band and out-of-band frequency regions. By setting $M = 3$ NMSE, NMSE_{bb} as well as WESPR_{bb} are further improved by approximately 15 dB. Given

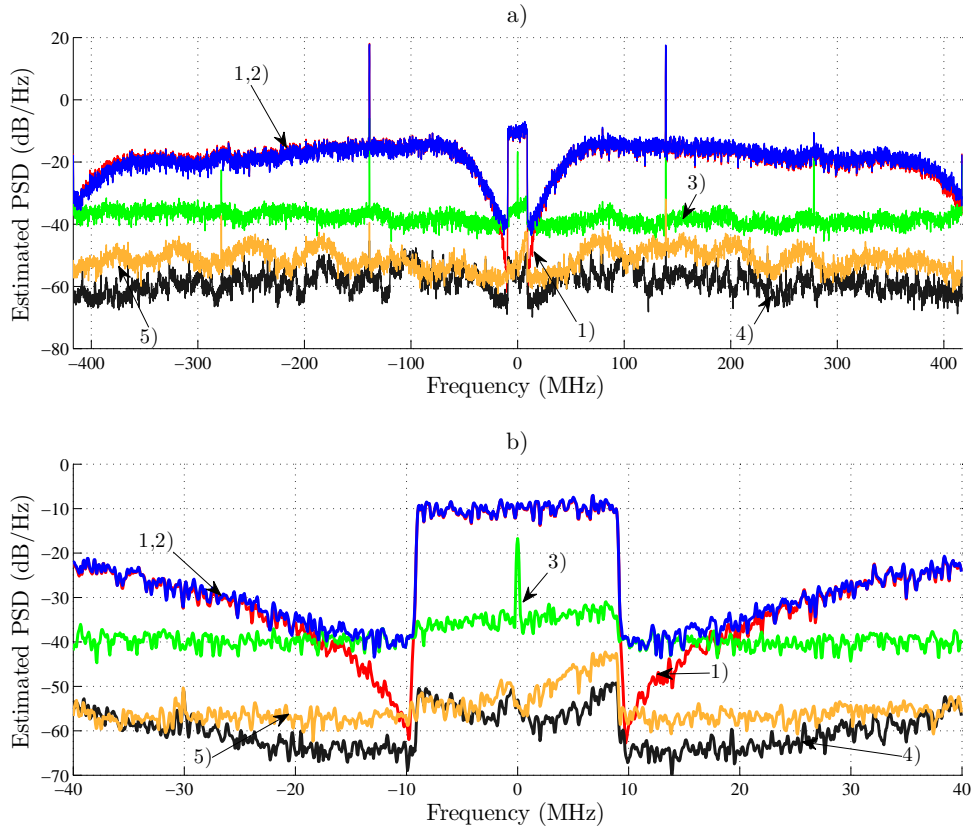


FIGURE 5.13: Measurement based spectra shown a) over complete bandwidth of the encoded sequences b) near the signal band for 1) excitation 2) measured output 3) error without modeling 4) error with equivalent nISI model 5) error with TDNN based model.

that $M = 3$ equals $M_{\text{RF}} = 36$ for $R_s = 12$, it becomes obvious that the baseband model captures the significant proportion of the reference system memory, which concerns 48 RF symbols. This in the end leads to an excellent modeling accuracy for the given f_{IF} settings.

Figure 5.12 depicts the modeling precision of the TDNN based nISI model, where $M_i \in [2, 4, 6, 8, 10]$ and $N_i = 10$. The obtained overall accuracy is clearly smaller in comparison with the equivalent baseband nISI model. This reflects the drawbacks of the TDNN based modeling i.e. the convergence to a local optimum and the residual nISI terms. Nevertheless, according to NMSE_{bb} and WESPR_{bb} the model achieves a satisfactory performance for the multiple f_c settings with reduced computational complexity. Secondly, as visible from all the evaluated FoMs, no performance gains are obtained for $M_i > 4$. Referring to the discussion

above, for those settings the equivalent $M_{\text{RF}} > 48$, which clearly exceeds the finite memory depth of the reference system. In addition, the TDNN based nISI model remains well behaved for higher M_i settings although the excitation includes only a subset of the higher order nISI terms. This suggests that the model fitting by Levenberg-Marquard back-propagation leads to a better numerical stability.

5.3.4 Measurement based results

Further model validations concern real world measurements. The motivation for the additional modeling tasks is twofold. Firstly, the usefulness of the black box modeling approach for center frequency agile digital transmitters shall be explained. Secondly, the measurement based modeling is an effective method to test the hypothesis concerning the higher order nISI. At first by investigating the error spectrum 3) between the excitation 1) and the measured output 2) shown in Figure 5.13, it becomes clear that the measurement system exhibits nISI. This is particularly indicated by the raised noise floor of the measured output signal near the signal band as shown in Figure 5.13 b). Most importantly, the obtained error spectra related to 4), the equivalent baseband nISI model, and 5) the TDNN based nISI model indicate that the respective models are working successfully.

In order to investigate the suitability of the given models for flexible f_c digital transmitter operation further model validations were performed. Excitation sequences were generated for 20 randomly chosen f_{IF} settings between $[0, 0.42]f_s$. The modeling results for the equivalent baseband nISI model are shown in Figure 5.14. Again already moderate memory depths yield an accurate performance over the considered f_{IF} range. This allows for an interpretation that the reference system exhibits only short term memory effects. Nevertheless, the difference in NMSE between $M = 2$ and $M = 3$ is notable. As given in Table 5.2 a mean improvement of approximately 2.5 dB in NMSE is observed. Further, as visible from Figure 5.14 a) there is a fluctuation in NMSE of about 1.5 dB. This can be explained by the varying statistical properties of the Q Σ Δ PWM encoded complex baseband sequences. Although all of the sequences fulfil the condition for sufficient

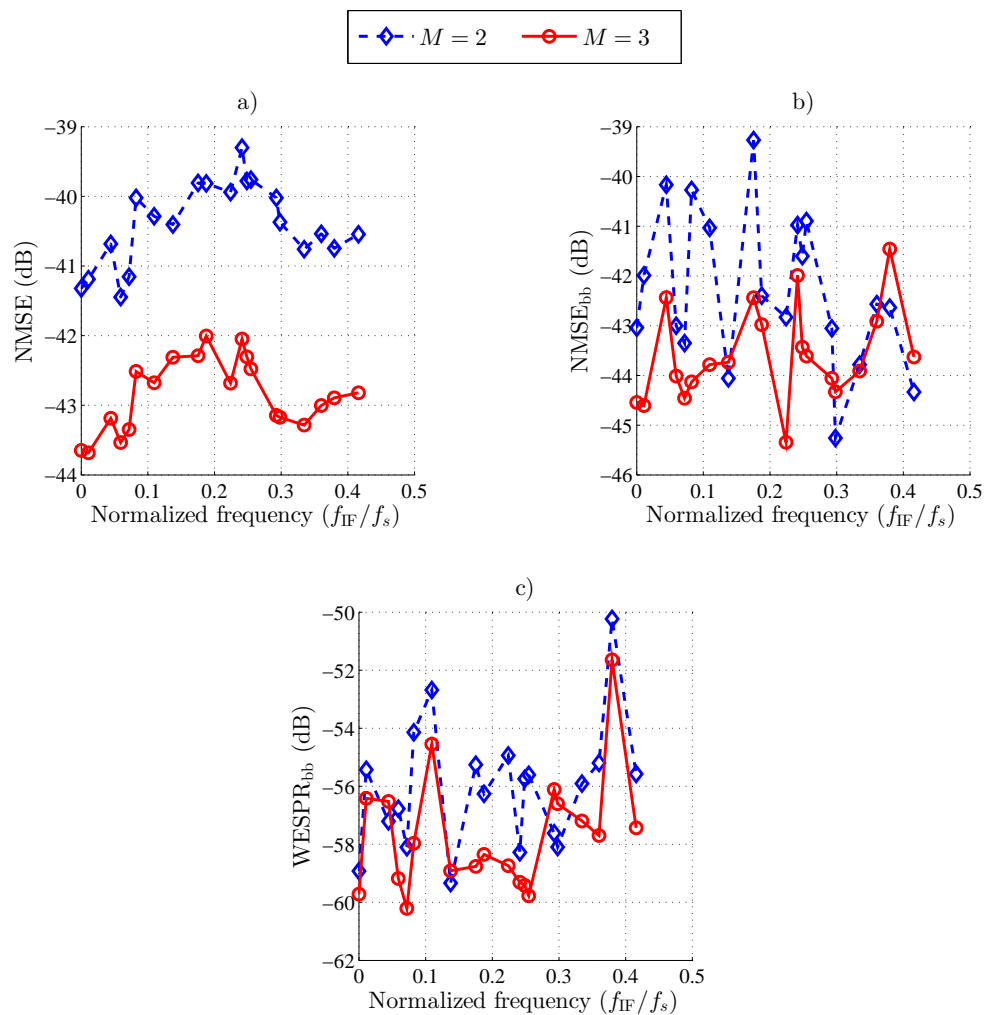


FIGURE 5.14: Measurement based modeling performance of the equivalent baseband nISI model in terms of a) NMSE b) NMSE_{bb} and c) WESPR_{bb} , where $2 \leq M \leq 3$.

excitation, the unequally distributed nISI terms in the excitation blocks lead to different parameter estimation results. For some excitations the nISI term distributions may result in favourable weighting of those nISI terms with dominant distortion energy, and hence, to a lower NMSE¹. At next, NMSE_{bb} and WESPR_{bb} measures given in Figure 5.14 b) and Figure 5.14 c), respectively, demonstrate that the equivalent complex baseband nISI model yields nearly constant performance close to the signal band. The variations in the obtained signal band results can be explained by the unequally distributed frequency domain modeling error from

¹This argumentation is of course valid only by assuming that the electrical properties of the reference system do not change significantly.

the least squares fit. The mean values for NMSE_{bb} and WESPR_{bb} are given in Table 5.2. It can be observed that improvements of circa 1.5 dB for NMSE_{bb} and 1.7 dB for WESPR_{bb} can be obtained when M is increased from 2 to 3.

TABLE 5.2: Mean NMSE over f_{IF} and number of multiplications for equivalent baseband nISI model

M	NMSE (dB)	NMSE_{bb} (dB)	WESPR_{bb} (dB)	MUL
2	-40.4	-42.3	-55.5	656
3	-42.9	-43.6	-57.2	2624

Secondly, the measurement based modeling verifications were repeated for the TDNN based model. The results are depicted in Figure 5.15 for various M_i and the considered f_{IF} settings. At first it can be seen that e.g. for $M_i = 2$ the modeling results are on the average weaker in comparison to the equivalent nISI baseband model. This is largely due to the mentioned residual terms and also because of possible local minimum solutions. Nevertheless, the TDNN based model successfully captures the nISI effects for a multitude f_{IF} as demonstrated by NMSE values shown in Figure 5.15 a). The improved NMSE results for $M_i \geq 4$ seem at first contradicting. As discussed above, for those settings the excitations do not fulfil the condition for the sufficient excitation. Therefore, a more plausible explanation is that the larger M_i settings allow for converge to local minimum solutions for which the residual terms are more strongly suppressed. This reasoning is supported by the mean NMSE values given in Table 5.3. As clearly visible, even for $M_i = 10$ the obtained results do not overrule the respective measures for equivalent baseband nISI model with $M_i = 3$. A similar performance increase can be noted also for mean NMSE_{bb} and WESPR_{bb} values. Furthermore, as depicted in Figures 5.15 b) and c) the modeling accuracy near signal band is, due to the same reasons as for the equivalent baseband nISI model, more dependent on the f_{IF} setting.

The computational requirements in terms of multiplications (MUL) for the equivalent complex baseband nISI model and for the TDNN based nISI model are listed in Table 5.2 and in Table 5.3, respectively. The principal advantage of the TDNN

TABLE 5.3: Mean NMSE over f_{IF} and number of multiplications for TDNN based nISI model

M_i	NMSE (dB)	NMSE _{bb} (dB)	WESPR _{bb} (dB)	MUL
2	-37.6	-37.9	-52.7	152
4	-38.3	-39.4	-55.1	232
6	-38.6	-39.4	-54.9	312
8	-40.9	-41.8	-56.3	392
10	-41.1	-42.7	-56.5	472

based model is the lower amount of multiplications ranging between 152 and 472 for $2 \leq M_i \leq 10$. On the contrary for the equivalent baseband nISI model the number of multiplications for $M = 2$ and $M = 3$ becomes 656 and 2624, respectively. Hence, a significant reduction in computational complexity can be obtained by utilizing the TDNN based model, especially for larger memory depths.

5.4 Summary

This Chapter presented novel behavioral models for digital RF transmitters. Those models utilize the inherent redundancy of the RF sequence to perform the modeling with a lower number of RF symbols in comparison to the generalized nISI model. This in the end enables reduced computational complexity and savings in the computational resources.

From the two proposed models, the first one is the Volterra series based equivalent baseband nISI model and the second one is the TDNN based baseband nISI model. According to the simulation and the measurement based model verification results, both models show successful modeling performance for multiple f_c settings. Furthermore, the modeling accuracy of the models in terms of frequently used FoMs is close to those reported for RF transmitters operating with band-limited, wide-band RF signals [89]. The main difference between the two models is that the TDNN based model exhibits polynomial complexity and the equivalent baseband nISI model shows exponential complexity. However, the lower

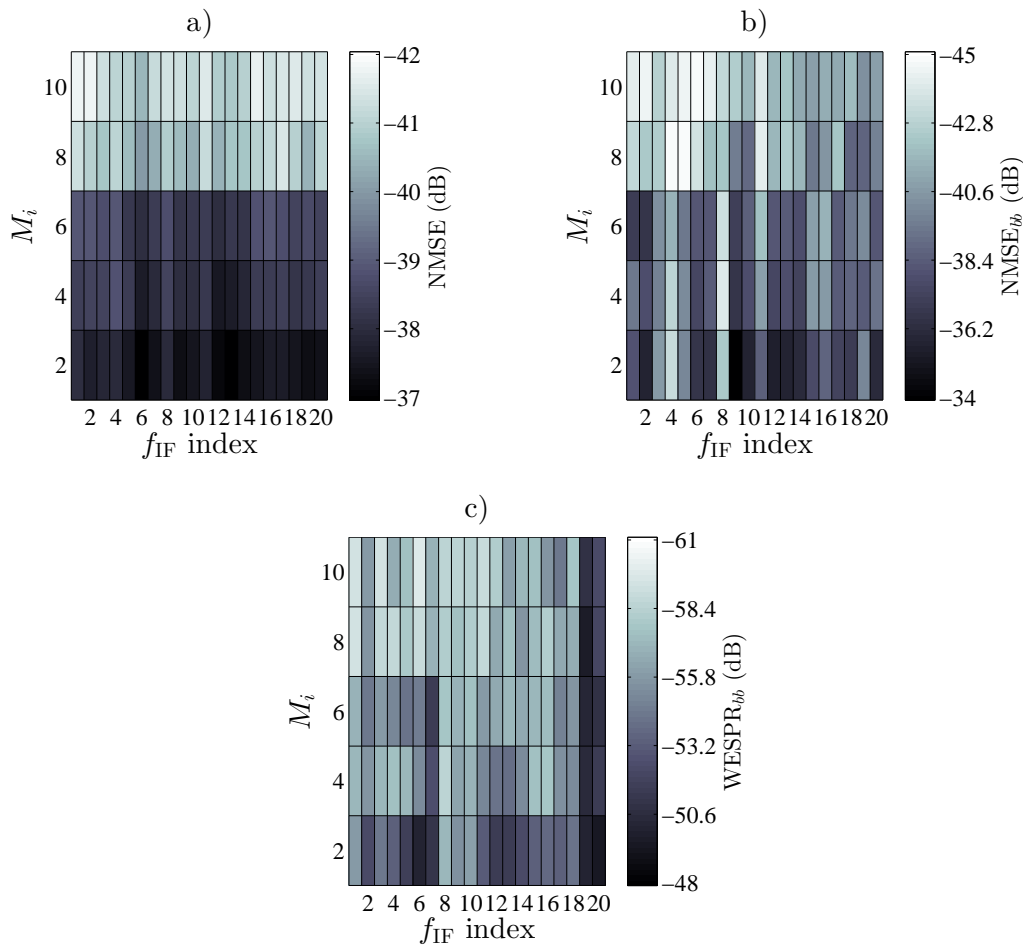


FIGURE 5.15: Measurement based modeling performance of the TDNN based model in terms of a) NMSE b) $NMSE_{bb}$ and c) $WESPR_{bb}$, where $M_i \in [2, 4, 6, 8, 10]$ and $N_i = 10$.

TDNN model computational complexity comes at the cost of residual non-linear terms and the possible local optimum solutions, which leads to reduced modeling performance. This was indicated by the simulation results, where the equivalent nISI model yielded over 10 dB performance gain in terms of NMSE, $NMSE_{bb}$ and $WESPR_{bb}$. Nevertheless, conforming to the measurement based results reflecting a more realistic scenario, with a suitable selection of the TDNN based model parameters, the performance difference can be reduced to a few dBs.

Finally, it can be stated that the given models are suitable tools for investigating the nISI effects of digital transmitters. Moreover, the observed improvement in

the modeling performance by increased memory depth supports the hypothesis, that nISI is a function over multiple RF symbols.

Chapter 6

Conclusions

Digital RF transmitters have the potential to tackle the challenges of future wireless transmission systems. However, in order to bring the theoretical advances closer to practice, further engineering efforts both in digital and analog domain have to be taken. This thesis aimed at improving f_c adjustability of the quadrature type digital transmitters by means of digital signal processing techniques. To this end, a novel PWM modulator, compensating quadrature noise shaped encoding algorithms as well as new complex baseband behavioral models were introduced. The most important aspects related to those contributions are summarized below.

Firstly, a novel Q $\Sigma\Delta$ PWM modulator to encode quadrature sequences was proposed. Contrary to the conventional PWM methods, the closed-loop topology of the Q $\Sigma\Delta$ PWM requires neither crossing point calculation nor specialized NTFs. Furthermore, due to the close relationship with quadrature $\Sigma\Delta$ modulators, one can apply the existing tools for e.g. NTF design, analytical N_p calculations or stability analysis. However, unlike the open-loop PWM modulators operating at f_{PWM} , Q $\Sigma\Delta$ PWM operates at $f_s > f_{\text{PWM}}$, which may lead to restrictions in the input signal bandwidths on reconfigurable hardware implementations. Nevertheless, the modulator operates as desired even when the highest frequency component of the input signal is well beyond f_{PWM} , which allows for wide f_{IF} tuning. This in turn is the first and the crucial step towards f_c agility. Simulation based analysis revealed some important and interesting facts. Most important, nearly constant

SNDR can be guaranteed for the majority of available f_{IF} tuning range. Secondly, in terms of SNDR and APRR it is wise not to utilize too strong NTF, i.e. an NTF with a high $|NTF(z)|_{\infty}$. The obtained results suggest also that an f_{PWM} setting leading to an optimal APR can be found iteratively for an arbitrary selection of NTF. Also, according to quantizer gain analysis, Q $\Sigma\Delta$ PWM applying conventional higher order, $\Sigma\Delta$ NTFs ($N > 2$) is likely to become unstable independent of σ_x .

Secondly, as it turned out, it is not sufficient to perform noise shaping appropriately over the signal of interest in complex baseband. The conjugate quantization noise and image problem connected to the digital up-conversion leads to a severe signal band distortion, which in the worst case, corrupts the complex baseband noise shaping. By modifying the phase and amplitude of the quantization noise in the complex domain, a cancelation of the conjugate quantization noise can be obtained. Depending on the f_c and OSR settings, the compensation yields an improvement of up to 50 dB in SNDR. Furthermore, the cancelation based noise shaping techniques outperform the techniques based on optimization of the quantization noise magnitude. The main result of the presented, novel quadrature noise shaped encoder topologies is that conjugate noise and the conjugate signal image can be *completely* suppressed for many modulator settings over the whole f_c tuning range. This property is true especially for the modulator parameters for which a realistic hardware configuration is available.

Thirdly, the distortion mechanism of the analog circuitry, i.e. the nISI, was studied. The particular encoding method used in the quadrature type digital transmitters allows for complex baseband modeling of nISI with possibility to access memory depths much longer than what is currently possible with the generalized nISI model. Additionally, the modeling over a limited bandwidth is suitable from the system level point of view, since the relevant distortion products are those that are left after the reconstruction by the band-pass filter. From the two presented models, the Volterra based equivalent complex baseband nISI model showed in general improved modeling performance in comparison to the second, TDNN

based nISI model. According to measurements both models exhibited NMSE below -40 dB for multiple f_c settings over 400 MHz f_c tuning range.

6.1 Future work

A general motivation for future work is to increase the coding efficiency, i.e. the ratio between σ_x and the average power of the encoded sequence. Conventionally improved coding efficiency, leading also to superior transmitter efficiency is achieved by reducing the quantization noise power. This could be done e.g. by including multi-level PWM support for Q $\Sigma\Delta$ PWM, which can attain coding efficiencies of up to 78% [57]. Alternatively, the presented quadrature noise shaped encoding methods to mitigate for conjugate quantization noise could be applied with modifications to digital RF-PWM modulators such as those given in [21]. The further future aspects may include the following.

- The current development of computing hardware tends to multi-core processor systems, which are effective for parallel computing tasks. Hence, parallelization of Q $\Sigma\Delta$ PWM in the same fashion as [97] would allow encoding with a lower f_s and thus enable potential support for higher transmission signal bandwidths.
- The enhanced digital up-conversion techniques are effective in principle for a single carrier setting. Conjugate quantization noise cancelation over multiple bands would be a basis for advanced direct-to-RF multi-carrier digital RF transmitters.
- To enable the utilization of the digital transmitters in wireless mobile applications, the nISI based distortion shall be effectively mitigated. Therefore, novel linearization concepts that are effective to mitigate long term nISI shall be developed. Possible ways to do this would include embedding the presented nISI models in the Q $\Sigma\Delta$ PWM noise shaping loop in the same fashion

as [98]. A second approach involves an alternative noise shaping [technique](#) with inherent nISI mitigation capabilities [44].

Appendix A

Derivation of (4.44)

For R_o settings the z-domain transfer function between $v(n)$ and $e(n)$ becomes

$$\begin{aligned} V(z) &= [E(z) - \Gamma_o E^*(-z^*) - z^{-1} \Gamma_o V^*(-z^*)] F(z) \\ V^*(-z^*) &= [E^*(-z^*) - \Gamma_o^* E(z) - z^{-1} \Gamma_o^* V(z)] F^*(-z^*), \end{aligned} \quad (\text{A.1})$$

where $\Gamma_o = \Gamma_o(jf_{\text{IF}})$. Thus

$$\begin{aligned} V(z) &= \{E(z) - \Gamma_o E^*(-z^*) - z^{-1} \Gamma_o [E^*(-z^*) F^*(-z^*) \\ &\quad - \Gamma_o^* E(z) F^*(-z^*) - z^{-1} \Gamma_o^* V(z) F^*(-z^*)]\} \end{aligned} \quad (\text{A.2})$$

After a few algebraic steps we arrive at

$$\begin{aligned} V(z) &= \frac{E(z)[F(z) + z^{-1} |\Gamma_o|^2 F^*(-z^*) F(z)]}{1 - z^{-2} |\Gamma_o|^2 F^*(-z^*) F(z)} \\ &\quad - \frac{E^*(-z^*) [\Gamma_o F(z) + z^{-1} \Gamma_o F^*(-z^*) F(z)]}{1 - z^{-2} |\Gamma_o|^2 F^*(-z^*) F(z)}. \end{aligned} \quad (\text{A.3})$$

Since $Y(z) = E(z) - V(z)$ the complete transfer function becomes

$$\begin{aligned} Y(z) &= E(z) \left\{ 1 - \frac{z^{-1} [F(z) + |\Gamma_o|^2 F^*(-z^*) F(z)]}{1 - z^{-2} |\Gamma_o|^2 F^*(-z^*) F(z)} \right\} + \\ &\quad E^*(-z^*) \left\{ \frac{z^{-1} \Gamma_o [F(z) + F^*(-z^*) F(z)]}{1 - z^{-2} |\Gamma_o|^2 F^*(-z^*) F(z)} \right\} \\ &= E(z) \text{NTF}_o(z) + E^*(-z^*) \text{INTF}_o(z). \end{aligned} \quad (\text{A.4})$$

The transfer function for R_e settings is obtained similarly. At first

$$\begin{aligned} V(z) &= [E(z) - \Gamma_e E^*(z^*) - z^{-1} \Gamma_e V^*(z^*)] F(z) \\ V^*(z^*) &= [E^*(z^*) - \Gamma_e^* E(z) - z^{-1} \Gamma_e^* V(z)] F^*(z^*), \end{aligned} \quad (\text{A.5})$$

where $\Gamma_e = \Gamma_e(jf_{IF})$. Hence,

$$\begin{aligned} V(z) &= \{E(z) - \Gamma_e E^*(z^*) - z^{-1} \Gamma_e [E^*(z^*) F^*(z^*) \\ &\quad - \Gamma_e^* E(z) F^*(z^*) - z^{-1} \Gamma_e^* V(z) F^*(z^*)]\} \end{aligned} \quad (\text{A.6})$$

Reorganization of the terms on the right hand side leads to

$$\begin{aligned} V(z) &= \frac{E(z)[F(z) + z^{-1} |\Gamma_e|^2 F^*(z^*) F(z)]}{1 - z^{-2} |\Gamma_e|^2 F^*(z^*) F(z)} \\ &\quad - \frac{E^*(z^*) [\Gamma_e F(z) + z^{-1} \Gamma_e F^*(z^*) F(z)]}{1 - z^{-2} |\Gamma_e|^2 F^*(z^*) F(z)}. \end{aligned} \quad (\text{A.7})$$

Again, since $Y(z) = E(z) - V(z)$ the complete transfer function becomes

$$\begin{aligned} Y(z) &= E(z) \left\{ 1 - \frac{z^{-1} [F(z) + |\Gamma_e|^2 F^*(z^*) F(z)]}{1 - z^{-2} |\Gamma_e|^2 F^*(z^*) F(z)} \right\} + \\ &\quad E^*(z^*) \left\{ \frac{z^{-1} \Gamma_e [F(z) + F^*(z^*) F(z)]}{1 - z^{-2} |\Gamma_e|^2 F^*(z^*) F(z)} \right\} \\ &= E(z) \text{NTF}_e(z) + E^*(z^*) \text{INTF}_e(z). \end{aligned} \quad (\text{A.8})$$

Bibliography

- [1] Simon Haykin. Cognitive radio: brain-empowered wireless communications. *IEEE Journal on Selected Areas in Communications*, 23(2):201–220, Feb. 2005.
- [2] L. Anttila, P. Handel, and M. Valkama. Joint mitigation of power amplifier and i/q modulator impairments in broadband direct-conversion transmitters. *IEEE Transactions on Microwave Theory and Techniques*, 58(4):730–739, Apr. 2010.
- [3] The international technology roadmap for semiconductors (itrs), system drivers. 2013. URL <http://www.itrs.net/>.
- [4] J. Mitola. The software radio architecture. *IEEE Communications Magazine*, 33(5):26–38, 1995.
- [5] A. Wentzel, C. Meliani, and W. Heinrich. Rf class-s power amplifiers: State-of-the-art results and potential. In *IEEE MTT-S International Microwave Symposium Digest*, page 1, May 2010.
- [6] M.M. Ebrahimi and M. Helaoui. Delta-sigma-based transmitters: Advantages and disadvantages. *IEEE Transactions on Microwave Theory and Techniques*, 14(99):1–7, 2013.
- [7] F.M. Ghannouchi, S. Hatami, P. Aflaki, M. Helaoui, and R. Negra. Accurate power efficiency estimation of ghz wireless delta-sigma transmitters for different classes of switching mode power amplifiers. *IEEE Transactions on Microwave Theory and Techniques*, 58(11):2812–2819, Nov. 2010.

-
- [8] A Jayaraman, P.F. Chen, G. Hanington, L. Larson, and P. Asbeck. Linear high-efficiency microwave power amplifiers using bandpass delta-sigma modulators. *IEEE Microwave and Guided Wave Letters*, 8(3):121–123, Mar. 1998.
- [9] T. Johnson and S. P. Stapleton. Rf class-d amplification with bandpass sigma-delta modulator drive signals. *IEEE Transactions on Circuits and Systems I: Regular Papers*, 53(12):2507–2520, Dec 2006.
- [10] J. Sommarek, V. Saari, J. Lindeberg, J. Vankka, and K. Halonen. A 20 mhz bp-pwm and bp-dsm class-d pa in 0.18 cmos. In *12th IEEE International Conference on Electronics, Circuits and Systems*, pages 1–4, Dec. 2005.
- [11] P. Wagh and P. Midya. High-efficiency switched-mode rf power amplifier. In *42nd Midwest Symposium on Circuits and Systems*, volume 2, pages 1044–1047, 1999.
- [12] M. Helaoui, S. Hatami, R. Negra, and F.M. Ghannouchi. A novel architecture of delta-sigma modulator enabling all-digital multiband multistandard rf transmitters design. *IEEE Transactions on Circuits and Systems II: Express Briefs*, 55(11):1129–1133, Nov. 2008.
- [13] A. Frappe, A. Flament, B. Stefanelli, A. Kaiser, and A. Cathelin. An all-digital rf signal generator using high-speed delta-sigma modulators. *IEEE Journal of Solid-State Circuits*, 44(10):2722–2732, Oct. 2009.
- [14] K. Finnerty, J. Dooley, and R. Farrell. Digital quadrature mixing of lowpass sigma-delta modulators for switch-mode power amplifiers. In *20th European Conference on Circuit Theory and Design*, pages 282–285, Aug. 2011.
- [15] N.V. Silva, A.S.R. Oliveira, U. Gustavsson, and N.B. Carvalho. A novel all-digital multichannel multimode rf transmitter using delta-sigma modulation. *IEEE Microwave and Wireless Components Letters*, 22(3):156–158, Mar. 2012.
- [16] T. Kitayabu and H. Ishikawa. Generalized architecture of concurrent dual-band transmitter for spectrum aggregation system. In *21st International*

- Symposium on Personal Indoor and Mobile Radio Communications*, pages 111–116, 2010.
- [17] B.T. Thiel, A. Ozmert, J. Guan, and R. Negra. Lowpass delta-sigma modulator with digital upconversion for switching-mode power amplifiers. In *Microwave Symposium Digest (MTT), 2011 IEEE MTT-S International*, pages 1–4, june 2011. doi: 10.1109/MWSYM.2011.5972816.
- [18] P. Midya, P. Wagh, and P. Rakers. Quadrature integral noise shaping for generation of modulated rf signals. In *The 45th Midwest Symposium on Circuits and Systems*, volume 2, pages 537–540, Aug. 2002.
- [19] N.V. Silva, A.S.R. Oliveira, and N.B. Carvalho. Evaluation of pulse modulators for all-digital agile transmitters. In *MTT-S International Microwave Symposium Digest*, pages 1–3, Jun. 2012.
- [20] Thomas Johnson, Kelly Mekechuk, and David Kelly. Noise shaped pulse position modulation for rf switch-mode power amplifiers. In *European Microwave Integrated Circuits Conference (EuMIC)*,, pages 320–323, Oct. 2011.
- [21] V. Bassoo and M. Faulkner. Sigma-delta digital drive signals for switchmode power amplifiers. *Electronics Letters*, 44(22):1299–1300, 2008.
- [22] B.T. Thiel, S. Dietrich, N. Zimmermann, and R. Negra. System architecture of an all-digital ghz transmitter using pulse-width/position-modulation for switching-mode pas. In *Asia Pacific Microwave Conference*, pages 2340–2343, Dec. 2009.
- [23] J. Keyzer, R. Uang, Y. Sugiyama, M. Iwamoto, I. Galton, and P.M. Asbeck. Generation of rf pulsewidth modulated microwave signals using delta-sigma modulation. In *MTT-S International Microwave Symposium Digest*, volume 1, pages 397–400, 2002.

- [24] C. Berland, I. Hibon, J.F. Bercher, M. Villegas, D. Belot, D. Pache, and V. Le Goasoz. A transmitter architecture for nonconstant envelope modulation. *IEEE Transactions on Circuits and Systems II: Express Briefs*, 53(1): 13–17, Jan. 2006.
- [25] M.E. Heidari, Minjae Lee, and A.A. Abidi. All-digital outphasing modulator for a software-defined transmitter. *IEEE Journal of Solid-State Circuits*, 44(4):1260–1271, 2009.
- [26] R. Schreier. *Noise Shaped Encoding*. PhD thesis, University of Toronto, 1991.
- [27] S. Norsworthy, R. Schreier, and G. Temes. *Delta-Sigma Data Converters: Theory, Design, and Simulation*. 1996.
- [28] S.A. Jantzi, K.W. Martin, and A.S. Sedra. Quadrature bandpass delta; sigma; modulation for digital radio. *IEEE Journal of Solid-State Circuits*, 32(12): 1935–1950, Dec. 1997.
- [29] Jaakko Marttila, Markus Allen, and Mikko Valkama. Multistage quadrature sigma-delta modulators for reconfigurable multi-band analog-digital interface in cognitive radio devices. *EURASIP Journal on Wireless Communications and Networking*, 2011(1):130, 2011.
- [30] M. Nielsen and T. Larsen. A transmitter architecture based on delta-sigma modulation and switch-mode power amplification. *Circuits and Systems II: Express Briefs, IEEE Transactions on*, 54(8):735–739, aug. 2007. ISSN 1549-7747. doi: 10.1109/TCSII.2007.899457.
- [31] A.B. Sripad and D. Snyder. A necessary and sufficient condition for quantization errors to be uniform and white. *IEEE Transactions on Acoustics, Speech and Signal Processing*, 25(5):442–448, Oct 1977.
- [32] Peter G. Gerzon, Michael A.; Craven. Optimal noise shaping and dither of digital signals. In *Audio Engineering Society Convention 87*, Oct. 1989.

- [33] J. Lindeberg, J. Vankka, J. Sommarek, and K. Halonen. A 1.5-v direct digital synthesizer with tunable delta-sigma modulator in 0.13- μm cmos. *IEEE Journal of Solid-State Circuits*, 40(9):1978–1982, 2005.
- [34] J. Vankka, J. Sommarek, J. Ketola, I. Teikari, and K.A.I. Halonen. A digital quadrature modulator with on-chip d/a converter. *Solid-State Circuits, IEEE Journal of*, 38(10):1635 – 1642, Oct. 2003.
- [35] A. Jerng and C.G. Sodini. A wideband delta-sigma digital-rf modulator for high data rate transmitters. *Solid-State Circuits, IEEE Journal of*, 42(8): 1710–1722, Aug. 2007.
- [36] Nelson V. Silva, Arnaldo S.R. Oliveira, and Nuno Borges Carvalho. Novel fine tunable multichannel all-digital transmitter. In *IEEE MTT-S International Microwave Symposium Digest*, pages 1–3, 2013.
- [37] P. Wagh, P. Midya, P. Rakers, J. Caldwell, and T. Schooler. An all-digital universal rf transmitter [cmos rf modulator and pa]. In *Proceedings of the IEEE Custom Integrated Circuits Conference*, pages 549 – 552, Oct. 2004.
- [38] M. Nielsen and T. Larsen. An rf pulse width modulator for switch-mode power amplification of varying envelope signals. In *Topical Meeting on Silicon Monolithic Integrated Circuits in RF Systems*, pages 277–280, Jan. 2007.
- [39] T. Podsiadlik, J. Dooley, A. Canniff, and R. Farrell. Pulse width modulation of multilevel delta-sigma output for class -s power amplifier. In *European Conference on Circuit Theory and Design*, pages 457 –460, Aug. 2009.
- [40] J. Vuolevi, T. Rahkonen, and J. Manninen. Measurement technique for characterizing memory effects in rf power amplifiers. In *Radio and Wireless Conference*, pages 195–198, 2000.
- [41] Qianli Mu, J.O. Coleman, D.P. Scholnik, and Z. Popovic? and. Circuit approaches to nonlinear-isi mitigation in noise-shaped bandpass d/a conversion. *IEEE Transactions on Circuits and Systems I: Regular Papers*, 57(7):1559 –1572, Jul. 2010.

- [42] J.O. Coleman. Modeling finite-memory nonlinearity in unit dac elements, binary storage channels, and bpsk data channels. In *Proceedings of the European Conference on Circuit Theory and Design*, volume 1, pages I/59 – I/62 vol. 1, Aug. 2005.
- [43] L. Risbo, R. Hezar, B. Kelleci, H. Kiper, and M. Fares. Digital approaches to isi-mitigation in high-resolution oversampled multi-level d/a converters. *IEEE Journal of Solid-State Circuits*, 46(12):2892 –2903, Dec. 2011.
- [44] A.K. Gupta, J. Venkataraman, and O.M. Collins. Measurement and reduction of isi in high-dynamic-range 1-bit signal generation. *IEEE Transactions on Circuits and Systems I: Regular Papers*, 55(11):3593 –3606, Dec. 2008.
- [45] T. Maehata, S. Kameda, and N. Suematsu. High aclr 1-bit direct radio frequency converter using symmetric waveform. In *42nd European Microwave Conference*, pages 1051–1054, 2012.
- [46] M. Tanio, S. Hori, M. Hayakawa, N. Tawa, K. Motoi, and K. Kunihiro. A linear and efficient 1-bit digital transmitter with envelope delta-sigma modulation for 700mhz lte. In *IEEE MTT-S International Microwave Symposium*, pages 1–4, Jun. 2014.
- [47] Norbert Leder, Holger Arthaber, and Henri Ruotsalainen. Characterization and optimization of pulse drivers for switched mode power amplifier measurements. In *Integrated Nonlinear Microwave and Millimetre-wave Circuits (INMMiC), 2014 International Workshop on*, pages 1–3, April 2014. doi: 10.1109/INMMiC.2014.6815107.
- [48] K.M. Smith, K.M. Smedley, and Yunhong Ma. Realization of a digital pwm power amplifier using noise and ripple shaping. In *26th Annual IEEE Power Electronics Specialists Conference*, volume 1, pages 96–102, Jun. 1995.
- [49] Lars Risbo and Thomas Morch. Performance of an all-digital power amplification system. In *104th Audio Engineering Society Convention*, May 1998.

-
- [50] C. Pascual, Zukui Song, P.T. Krein, D.V. Sarwate, P. Midya, and W.J. Roeckner. High-fidelity pwm inverter for digital audio amplification: Spectral analysis, real-time dsp implementation, and results. *IEEE Transactions on Power Electronics*, 18(1):473–485, Jan. 2003.
- [51] H.S. Black. *Modulation Theory*. Van Nostrand Reinhold, New York, 1953.
- [52] Zukui Song and Dilip V. Sarwate. The frequency spectrum of pulse width modulated signals. *Signal Processing*, 83(10):2227 – 2258, 2003.
- [53] S. Santi, R. Rovatti, and G. Setti. Spectral aliasing effects of pwm signals with time-quantized switching instants. In *Proceedings of the 2004 International Symposium on Circuits and Systems*, volume 4, pages 689–692, may 2004.
- [54] K. Hausmair, Shuli Chi, P. Singerl, and C. Vogel. Aliasing-free digital pulse-width modulation for burst-mode rf transmitters. *IEEE Transactions on Circuits and Systems I: Regular Papers*, 60(2):415–427, Feb 2013.
- [55] H. Mouton and B. Putzeys. Understanding the pwm nonlinearity: Single-sided modulation. *IEEE Transactions on Power Electronics*, 27(4):2116–2128, Apr. 2012.
- [56] 3GPP. E-utra; base station (bs) radio transmission and reception (release 10). Technical report, 3GPP, Oct. 2011.
- [57] N. V. Silva, A. S. R. Oliveira, and N. B. Carvalho. Design and optimization of flexible and coding efficient all-digital rf transmitters. *IEEE Transactions on Microwave Theory and Techniques*, 61(1):625 –632, Jan. 2013.
- [58] Midya Pallab; Miller Matt; Sandler Mark. Integral noise shaping for quantization of pulse-width modulation. In *109th Audio Engineering Society Convention*, Sep. 2000.
- [59] Mark B. Sandler, Jason M. Goldberg, Roderick Hiorns, Robert Bowman, Michael Watson, and Peter Ziman. Ultra-low distortion digital power amplification. In *91st Audio Engineering Society Convention*, Oct. 1991.

- [60] Peter Craven. Toward the 24-bit dac: Novel noise-shaping topologies incorporating correction for the nonlinearity in a pwm output stage. *Journal of Audio Engineering Society*, 41(5):291–313, 1993.
- [61] Bruno Putzeys. Simple, ultralow distortion digital pulse width modulator. In *120th Audio Engineering Society Convention*, 5 2006.
- [62] S. Jantzi, K. Martin, M. Snelgrove, and A. Sedra. A complex bandpass delta-sigma converter for digital radio. In *IEEE International Symposium on Circuits and Systems*, volume 5, pages 453–456, May 1994.
- [63] S. Ralph and R. Farrell. Using high pass sigma-delta modulation for class-s power amplifiers. In *18th European Conference on Circuit Theory and Design*, pages 707 –710, Aug. 2007.
- [64] Temes G. Schreier, R. *Understanding Delta-Sigma Data Converters*. Wiley-IEEE Press, 2004.
- [65] M. Nagahara and Y. Yamamoto. Frequency domain min-max optimization of noise-shaping delta-sigma modulators. *IEEE Transactions on Signal Processing*, 60(6):2828–2839, Jun. 2012.
- [66] Jia-Ming Liu, Shih-Hsiung Chien, and Tai-Haur Kuo. Optimal design for delta-sigma modulators with root loci inside unit circle. *IEEE Transactions on Circuits and Systems II: Express Briefs*, 59(2):83–87, Feb 2012.
- [67] U. Gustavsson, T. Eriksson, and C. Fager. Quantization noise minimization in sigma-delta modulation based rf transmitter architectures. *IEEE Transactions on Circuits and Systems I: Regular Papers*, 57(12):3082–3091, Dec 2010.
- [68] R. Schreier. The delta-sigma toolbox version 7.3. Technical report. URL <http://www.mathworks.com/matlabcentral/fileexchange/19>.
- [69] C.N. Nzeza, A. Flament, A. Frappe, A. Kaiser, A. Cathelin, and J. Muller. Reconfigurable complex digital delta-sigma modulator synthesis for digital

- wireless transmitters. In *4th European Conference on Circuits and Systems for Communications*, pages 320–325, Jul. 2008.
- [70] K.W. Martin. Complex signal processing is not complex. *IEEE Transactions on Circuits and Systems I: Regular Papers*, 51(9):1823–1836, Sep. 2004.
- [71] R.M. Gray. Oversampled sigma-delta modulation. *IEEE Transactions on Communications*, 35(5):481–489, May 1987.
- [72] R.T. Baird and T.S. Fiez. Stability analysis of high-order delta-sigma modulation for adc's. *IEEE Transactions on Circuits and Systems II: Analog and Digital Signal Processing*, 41(1):59–62, Jan. 1994.
- [73] R. Schreier, M.V. Goodson, and Bo Zhang. An algorithm for computing convex positively invariant sets for delta-sigma modulators. *Circuits and Systems I: Fundamental Theory and Applications, IEEE Transactions on*, 44(1):38–44, Jan. 1997.
- [74] S. Hein and A. Zakhor. On the stability of sigma delta modulators. *IEEE Transactions on Signal Processing*, 41(7):2322–2348, Jul. 1993.
- [75] Lee W.L. A novel higher order interpolative modulator topology for high resolution oversampling a/d converters. Master's thesis, Massachusetts's Institute of Technology, Cambridge, 1987.
- [76] L. Risbo. Stability predictions for high-order sigma; delta; modulators based on quasilinear modeling. In *IEEE International Symposium on Circuits and Systems*, volume 5, pages 361–364, May 1994.
- [77] M. Valkama and M. Renfors. A novel image rejection architecture for quadrature radio receivers. *IEEE Transactions on Circuits and Systems II: Express Briefs*, 51(2):61–68, 2004.
- [78] M. Valkama, K. Salminen, and M. Renfors. Digital i/q imbalance compensation in low-if receivers: principles and practice. In *14th International Conference on Digital Signal Processing*, volume 2, pages 1179–1182, 2002.

- [79] Julius O. Smith. *Introduction to Digital Filters with Audio Applications - on-line book*. URL <https://ccrma.stanford.edu/~jos/filters/>.
- [80] M. Valkama. *Advanced I/Q Signal Processing for Wideband Receivers: Models and Algorithms*. PhD thesis, Tampere University of Technology, 2001.
- [81] T.I. Laakso, V. Valimaki, M. Karjalainen, and U.K. Laine. Splitting the unit delay. *IEEE Signal Processing Magazine*, 13(1):30–60, Jan. 1996.
- [82] J.D. Johnston. A filter family designed for use in quadrature mirror filter banks. In *IEEE International Conference on Acoustics, Speech, and Signal Processing*, volume 5, pages 291–294, 1980.
- [83] G.T. Zhou, Hua Qian, Lei Ding, and R. Raich. On the baseband representation of a bandpass nonlinearity. *IEEE Transactions on Signal Processing*, 53(8):2953–2957, Aug. 2005.
- [84] G.-O.A. Glentis, P. Koukoulas, and N. Kalouptsidis. Efficient algorithms for volterra system identification. *IEEE Transactions on Signal Processing*, 47(11):3042–3057, Nov. 1999.
- [85] M. Schetzen. *The Volterra and Wiener Theories Nonlinear Systems*. Wiley, 1980.
- [86] M. Isaksson, D. Wisell, and D. Ronnow. A comparative analysis of behavioral models for rf power amplifiers. *IEEE Transactions on Microwave Theory and Techniques*, 54(1):348–359, Jan. 2006.
- [87] D. Silveira, M. Gadringer, H. Arthaber, and G. Magerl. Rf-power amplifier characteristics determination using parallel cascade wiener models and pseudo-inverse techniques. In *Asia-Pacific Conference Proceedings Microwave Conference Proceedings*, volume 1, pages 1–4, Dec. 2005.
- [88] D.R. Morgan, Zhengxiang Ma, Jaehyeong Kim, M.G. Zierdt, and J. Pastalan. A generalized memory polynomial model for digital predistortion of rf power amplifiers. *IEEE Transactions on Signal Processing*, 54(10):3852–3860, Oct. 2006.

- [89] F. Mkdem and S. Boumaiza. Physically inspired neural network model for rf power amplifier behavioral modeling and digital predistortion. *IEEE Transactions on Microwave Theory and Techniques*, 59(4):913–923, 2011.
- [90] Jr. Parker, R.E. and M. Tummala. Identification of volterra systems with a polynomial neural network. In *IEEE International Conference on Acoustics, Speech, and Signal Processing*, volume 4, pages 561–564, Mar. 1992.
- [91] G. Cybenko. Approximations by superpositions of sigmoidal functions. *Mathematics of Control, Signals, and Systems*, 2:303–314, 1989.
- [92] Jin Hu and Jun Wang. Global stability of complex-valued recurrent neural networks with time-delays. *IEEE Transactions on Neural Networks and Learning Systems*, 23(6):853–865, Jun. 2012.
- [93] M.T. Hagan and M.B. Menhaj. Training feedforward networks with the marquardt algorithm. *IEEE Transactions on Neural Networks*, 5(6):989–993, Nov. 1994.
- [94] H.B. Demuth Hagan, M.T. and M.H. Beale. *Neural Network Design*. Boston, MA: PWS Publishing, 1996.
- [95] Per Landin, M. Isaksson, and P. Handel. Comparison of evaluation criteria for power amplifier behavioral modeling. In *IEEE MTT-S International Microwave Symposium Digest*, pages 1441–1444, Jun. 2008.
- [96] D. Wisell, M. Isaksson, and N. Keskitalo. A general evaluation criteria for behavioral power amplifier modeling. In *69th ARFTG Conference*, pages 1–5, Jun. 2007.
- [97] T. Podsiadlik and R. Farrell. Time-interleaved sigma-delta modulators for fpgas. *Circuits and Systems II: Express Briefs, IEEE Transactions on*, 61(10):808–812, Oct. 2014.
- [98] M.M. Ebrahimi and M. Helaoui. Reducing quantization noise to boost efficiency and signal bandwidth in delta sigma based transmitters. *IEEE Transactions on Microwave Theory and Techniques*, (99):1–7.